

1 Every Flare, Everywhere: Untriggered Searches for Astrophysical Neutrino Transients Using Data

2 From the IceCube Detector

3 *by*

4 William Luszczak

5 A dissertation submitted in partial fulfillment of

6 the requirements for the degree of

7 Doctor of Philosophy

8 (Physics)

9 *at the*

10 UNIVERSITY OF WISCONSIN – MADISON

11 2021

12 Defended on 19 August 2021

13 Dissertation approved by the following members of the Final Oral Committee:

14 Albrecht Karle · Professor of Physics

15 Keith Bechtol · Assistant Professor of Physics

16 Ke Fang · Assistant Professor of Physics

17 Sebastian Heinz · Professor of Astronomy

18

© Copyright William Luszczak 2021

19

All Rights Reserved

20 Abstract

21 Recent results from the IceCube collaboration regarding the blazar TXS 0506+056 suggest
22 the presence of neutrino flares that are not temporally coincident with a significant corre-
23 sponding gamma ray flare. Such flares are particularly difficult to identify, as their presence
24 must be inferred from the temporal distribution of neutrino data alone. While previously
25 existing statistical methods fit for only the largest neutrino flare candidate at a particular
26 location, this work introduces an extension to fit for the contributions from multiple flare
27 candidates at once, thereby increasing the sensitivity to sub-threshold neutrino flares. The
28 need for a multiple flare fit is further motivated by the increasing duration of the IceCube
29 data available for analysis. In this work, this "multi-flare" method is applied to data from
30 the IceCube Neutrino Observatory using two different source catalogs to explore emission
31 from candidates similar to TXS 0506+056. This method is additionally used to create a
32 "multi-flare" skymap, describing the temporal variability of IceCube data at every point in
33 the neutrino sky. These results can be used to place further constraints on potential pop-
34 ulations of transient neutrino sources, serving as a complement to existing time-integrated
35 and time-dependent methods.

36 Acknowledgements

37 This thesis is dedicated to all the people who helped me along the way.

38 Thank you to my parents, Michael and Janice Luszczak, for loving and supporting me
39 since childhood, as well as for ensuring I had a strong start to my education which has
40 undoubtedly served me well to this day. I will always be impressed by just how good of a
41 start you both gave me to the rest of my life.

42 Thank you to my undergraduate research advisor, Ben Monreal, for putting up with me
43 when I was a dumb and useless undergraduate researcher. Despite my uselessness as an
44 undergrad, the opportunities you provided were the start of my growth into the (hopefully
45 slightly less useless) physicist I am today.

46 Thank you to my graduate advisor, Albrecht Karle, for providing the resources, direction,
47 guidance, and freedom to foster my scientific growth over the past five years. Additional
48 thanks to Jim Braun, for teaching and guiding me through the development of much of what
49 is presented in this thesis.

50 More broadly, I am especially thankful for WIPAC and the members of the IceCube
51 collaboration, in particular those who maintain the detector, software, and data for the rest
52 of us to use. I'd like to specifically call out Mike Richman, whose software framework (cSky)
53 was an integral component to making much of this work possible.

54 Final thanks to Dan, Bhavna, Krysten, David, and Zain: my friends and classmates who
55 were the best part of undergrad, and who deserve a lot of credit for making the start of my
56 academic career enjoyable. I'd also like to thank Sarah and Austin, who in addition to being
57 valued friends, served as unofficial peer mentors over the past five years of graduate school.

58 **Contents**

| | | |
|----|--|-----------|
| 59 | Abstract | i |
| 60 | Acknowledgements | ii |
| 61 | 1 Introduction | 1 |
| 62 | 2 Astrophysical Messengers | 5 |
| 63 | 2.1 Cosmic Rays | 5 |
| 64 | 2.1.1 Energy Spectrum | 5 |
| 65 | 2.1.2 Acceleration Mechanism | 6 |
| 66 | 2.2 Photons | 8 |
| 67 | 2.2.1 Leptonic Radiative Processes | 9 |
| 68 | 2.2.2 Hadronic Radiative Processes | 11 |
| 69 | 2.2.3 Gamma Rays as an Astrophysical Messenger | 12 |
| 70 | 2.3 Neutrinos | 13 |
| 71 | 2.3.1 Production Mechanisms | 13 |
| 72 | 2.3.2 Observed Neutrino Spectrum | 14 |
| 73 | 2.3.3 Neutrinos as Astrophysical Messengers | 15 |
| 74 | 2.3.4 AGN as Neutrino Source Candidates | 16 |
| 75 | 2.3.5 Galactic Neutrino Sources | 20 |
| 76 | 2.3.6 Constraints on Neutrino Source Populations from Diffuse Measurements | 21 |
| 77 | 3 The IceCube Detector | 23 |

| | | |
|-----|---|-----------|
| 78 | 3.1 Detection Mechanism | 23 |
| 79 | 3.2 The Physical Components of the IceCube Detector | 26 |
| 80 | 3.3 Event Types | 29 |
| 81 | 3.3.1 Tracks | 30 |
| 82 | 3.3.2 Cascades | 31 |
| 83 | 3.3.3 Double Cascades | 31 |
| 84 | 3.4 Triggering | 32 |
| 85 | 3.5 Directional Reconstruction | 32 |
| 86 | 3.5.1 LineFit | 33 |
| 87 | 3.5.2 SplineMPE | 33 |
| 88 | 3.5.3 Paraboloid | 34 |
| 89 | 3.6 Energy Reconstruction | 35 |
| 90 | 3.7 IceCube Event Samples Overview | 36 |
| 91 | 3.7.1 PointSourceTracks v002p03 | 37 |
| 92 | 3.7.2 PointSourceTracks v003p02 | 38 |
| 93 | 3.7.3 NorthernTracks v002p06 | 39 |
| 94 | 4 Review and Improvements to Statistical Methods in Neutrino Astronomy | 46 |
| 95 | 4.1 Clustering Analysis Outline for an Arbitrary Test Statistic | 47 |
| 96 | 4.2 Unbinned Time Integrated Methods | 49 |
| 97 | 4.3 Unbinned Time-Dependent Methods | 53 |
| 98 | 4.3.1 Optimizing for a Single Flare | 53 |
| 99 | 4.3.2 Improving the Search for Temporal Clustering: Fitting Ensembles of | |
| 100 | Multiple Flares | 56 |
| 101 | 5 Applications of the Multi-flare Algorithm to Source Catalogs | 61 |
| 102 | 5.1 Self-Triggered Catalog | 62 |
| 103 | 5.2 Fermi 3LAC Blazars | 64 |

| | | |
|-----|---|------------|
| 104 | 6 An All-Sky Multi-flare Analysis | 77 |
| 105 | 6.1 Motivation | 77 |
| 106 | 6.2 Analysis Construction | 78 |
| 107 | 6.3 Results | 80 |
| 108 | 6.3.1 Hotspots and Populations Analysis | 80 |
| 109 | 6.3.2 Locations of External Interest | 84 |
| 110 | 7 Outlook | 96 |
| 111 | 8 Appendix: Statistics Background | 98 |
| 112 | 8.1 Estimators | 98 |
| 113 | 8.2 Likelihoods | 99 |
| 114 | 8.3 Confidence Intervals | 100 |
| 115 | 8.4 Hypothesis Testing | 101 |
| 116 | 8.4.1 State relevant null and alternative hypotheses | 101 |
| 117 | 8.4.2 State a test statistic | 102 |
| 118 | 8.4.3 Select a significance level at which the null hypothesis will be rejected | 104 |
| 119 | 8.4.4 Compute the TS from observed data | 106 |
| 120 | 8.4.5 Decide whether to accept or reject the null hypothesis | 106 |
| 121 | 8.5 Trial Factors | 107 |
| 122 | Bibliography | 109 |

₁₂₃ **Chapter 1**

₁₂₄ **Introduction**

₁₂₅ Though cosmic rays were first discovered in 1912, their origins have to date remained a
₁₂₆ mystery. Since cosmic rays are charged particles and their paths through the universe are
₁₂₇ bent by magnetic fields, identifying the sources of cosmic rays is not as simple as tracing back
₁₂₈ their arrival directions at Earth. The discovery of the astrophysical neutrino flux in 2013 [1]
₁₂₉ provides a new avenue for investigating this problem, as the sources of astrophysical neutrinos
₁₃₀ are suspected to be the same as high energy cosmic rays, but neutrinos are not charged, and
₁₃₁ thus their arrival directions point directly back to their source. Identifying the sources
₁₃₂ of astrophysical neutrinos (and consequently cosmic rays) would provide an entirely new
₁₃₃ view of the universe, potentially allowing us to examine regions opaque to more traditional
₁₃₄ astrophysical messengers such as photons. Additionally, neutrinos are a “smoking gun”
₁₃₅ for hadronic acceleration, providing important information about the processes of particle
₁₃₆ production in astrophysical sources.

₁₃₇ With the IceCube Neutrino Observatory having collected over 10 years of data, the
₁₃₈ first hints of astrophysical neutrino sources are beginning to be visible: a high energy alert
₁₃₉ event from the direction of the blazar TXS 0506+056 sparked multi-messenger followup that
₁₄₀ suggests neutrino emission from that location [2][3], and recent studies of time integrated
₁₄₁ neutrino emission from candidate blazars reveal a 3.5σ excess of astrophysical neutrino events
₁₄₂ from the direction of the Seyfert II galaxy NGC 1068 [4].

143 These first hints of astrophysical neutrino sources raise several further questions: Could
144 there be more sources like TXS 0506+056 or NGC 1068? How many? Is neutrino emission
145 time-dependent, or steady? Perhaps most importantly, if there are more sources, how can
146 we identify them? Though neutrinos are an excellent astrophysical messenger due to the
147 correlation of their arrival directions with their source of origin, neutrino astronomy is made
148 significantly more difficult by the existence of the atmospheric neutrino flux, which produces
149 a large, irreducible background for searches of astrophysical neutrino sources. Because of
150 this, high energy neutrino astronomy relies either on triggering off a multi-messenger signal
151 (such as a blazar that was also detected in gamma rays), or leveraging knowledge about the
152 pattern of neutrino emission (for example, the arrival directions of astrophysical neutrinos
153 should be clustered near their sources of origin, while the atmospheric background should
154 be isotropically distributed).

155 This work will focus specifically on exploring the possibility of time-dependent neutrino
156 emission, motivated in part by the archival followup that was performed by IceCube at the
157 location of the blazar TXS 0506+056 [3]. A novel method for fitting decorrelated ensembles of
158 neutrino flare candidates is introduced and subsequently applied to source catalogs assembled
159 according to properties of the TXS 0506+056 result that could potentially define a class of
160 astrophysical neutrino sources. This new method of fitting ensembles of neutrino flares is
161 intended to fill a methodological gap that exists in the field, as it provides a framework for
162 combining (“stacking”) neutrino flare candidates.

163 This method is additionally applied to the entire neutrino sky, allowing for a more gen-
164 eral examination of potential clustering of neutrino data in both space and time. If neutrino
165 data is clustered beyond what is expected from the background hypothesis (isotropic arrival
166 directions distributed uniformly in time), then that would be evidence of a population of
167 astrophysical neutrino sources. Even in the case of a non-discovery, the method introduced
168 here produces neutrino “light-curves” (here referred to as “flare curves”) which are of po-
169 tential use for future multi-messenger searches that may wish to incorporate information on
170 historical neutrino emission from a particular source candidate.

| | Time Independent | Untriggered Time-Dependent |
|-------------------------------|--|-----------------------------------|
| Single-Source Searches | Time-integrated skymap analysis [4] | Single flare analysis [3] |
| Source Stacking | Blazar catalog analysis [5] | This work! |

Figure 1.1: Examples of some of the types of astrophysical neutrino source searches that have been performed using IceCube data. Time-integrated analyses search for an excess of events over the entire data sample livetime, ignoring any information about potential temporal clustering. By contrast, untriggered, time-dependent searches attempt to fit for temporal neutrino clusters (“flares”) without using a multi-messenger lightcurve as a template. Single source searches report the most significant result from a small number of source candidate locations, corrected by a trial factor, while source stacking analyses combine information from many source locations under the assumption that each source candidate is a weak emitter, thereby increasing the search sensitivity to low individual source flux. Note that this table is certainly not an exhaustive list of all types of neutrino source searches, as there are many other types of analyses that can be constructed (e.g. template searches, multi-messenger light-curve correlation analyses, cross correlation analyses [?], [?], [?]). The analyses presented here are primarily intended to describe the space of analyses that are best suited for searching for point-like, flaring neutrino sources.

171 This thesis is organized as follows:

- 172 • Chapter 2 provides the scientific context and background information for this work, de-
tail the astrophysical messengers of interest (cosmic rays, photons, and neutrinos),
173 their production mechanisms, and their relevance to modern multi-messenger astron-
omy. Several potential candidates of astrophysical neutrino sources are introduced,
174 including TXS 0506+056 and NGC 1068.
- 175
- 176
- 177 • Chapter 3 describes the IceCube detector, which is used to collect the neutrino data
used in the analyses presented later in this work. This section details both the physical
178 components of the detector itself, as well as the triggering, event reconstruction, and
179 data sample event selections that are relevant for the later chapters.
- 180
- 181 • Chapter 4 discusses the existing methods of untriggered searches for astrophysical

182 neutrino flares, and subsequently introduces the new “multi-flare” modification that
183 is used to fit ensembles of flares at a candidate source location. This allows for a
184 statistically efficient combination of the significance of multiple, sub-threshold flares,
185 representing an improvement over previous methods that fit only the largest flare in
186 the data sample.

- 187 • Chapter 5 presents the application of the multi-flare method to two source catalogs,
188 motivated by previous results associated with the blazar TXS 0506+056. The first
189 catalog is a catalog of 3LAC blazars detected by the Fermi LAT detector. The second
190 catalog is formed by the locations of high energy IceCube events, in analog to the high
191 energy alert event that triggered the follow-up of TXS 0506+056.
- 192 • Chapter 6 presents the application of the multi-flare algorithm on an all-sky scale,
193 fitting for every potential neutrino flare candidate over the entire sky. Neutrino “flare
194 curves” at potentially interesting locations are examined, including the most significant
195 multi-flare locations, as well as the previously discussed source candidates of TXs
196 0506+056 and NGC 1068.
- 197 • Chapter 7 discusses the outlook for neutrino astronomy, and places the results pre-
198 sented in this work in the context of the field as a whole.

₁₉₉ **Chapter 2**

₂₀₀ **Astrophysical Messengers**

₂₀₁ This work will focus primarily on cosmic rays, photons, and neutrinos, however other mes-
₂₀₂ sengers, such as gravitational waves, can provide unique information as well.

₂₀₃ **2.1 Cosmic Rays**

₂₀₄ **2.1.1 Energy Spectrum**

₂₀₅ Cosmic rays are high energy protons and atomic nuclei, originating from outside the Earth's
₂₀₆ atmosphere. It is difficult to do traditional astronomy using cosmic rays (in the sense of using
₂₀₇ their arrival directions to identify sources) due to the fact that cosmic rays are charged, and
₂₀₈ consequently their paths are bent by magnetic fields in the universe. However, the cosmic
₂₀₉ ray spectrum is well studied, with many measurements having been made over the past
₂₁₀ century since their initial discovery. In general, the spectrum can be modeled as a power
₂₁₁ law (eq. 2.1):

$$N(E)dE \propto E^{-x}dE \quad (2.1)$$

₂₁₂ where N describes the number of cosmic ray particles, E is their energy, and x is an energy-
₂₁₃ dependent spectral index. The spectrum has several notable features, shown in figure 2.1.

At lower energies (below 3×10^{15} eV), the spectrum is well described by an $E^{-2.7}$ flux. At 3×10^{15} eV, the spectrum softens to $E^{-3.1}$, commonly referred to as the "knee", referring to the point where cosmic rays are energetic enough to no longer be contained by the galactic magnetic field. At even higher energies (around $10^{18.5}$ eV), the spectrum hardens again. This region is referred to as the "ankle", and is thought to correspond to the point where extragalactic cosmic rays begin to dominate the flux.

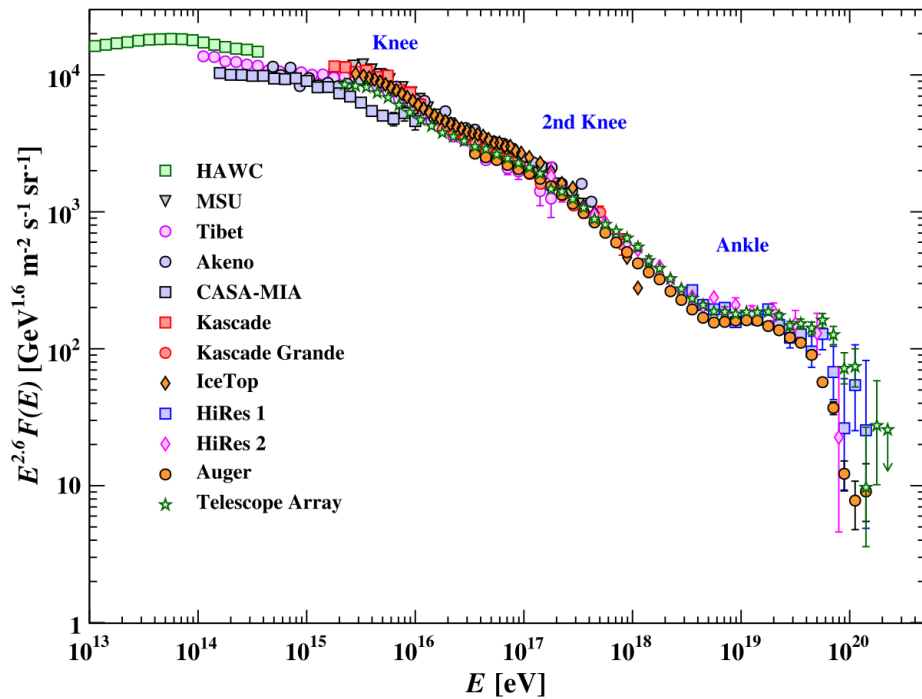


Figure 2.1: A plot of the cosmic ray spectrum assembled from observations from a variety of experiments. Major features visible are the knee ($\approx 10^{15}$ eV), and the ankle ($\approx 10^{18.5}$ eV). [?]

2.1.2 Acceleration Mechanism

Though the exact origin of cosmic rays is still unknown, we can infer how these particles are being accelerated based on our knowledge of how charged particles behave.

Suppose a particle encounters a moving cloud of plasma. If it is large enough, the cloud will act as a massive scatterer. The overall collision is the result of a large number of individual scatterings inside the cloud, and the outgoing angle of the original particle is

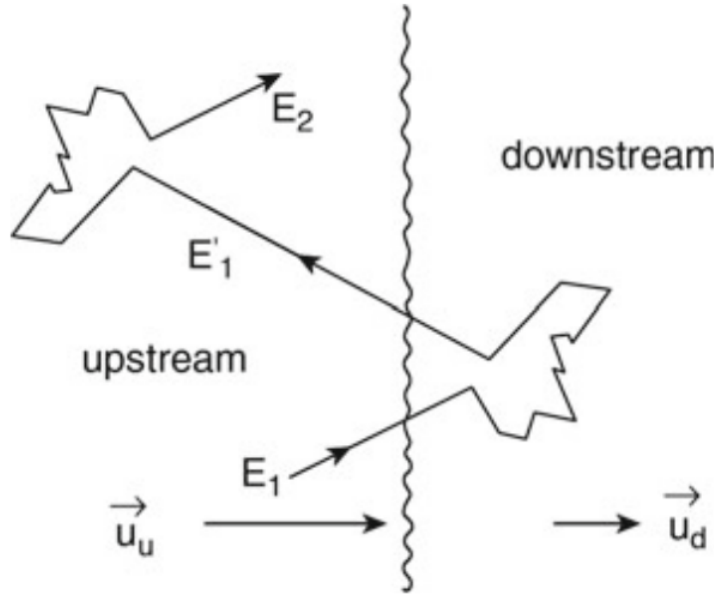


Figure 2.2: Fermi acceleration of a plane shock front[?].

226 essentially random. On average the energy of the particle after a collision with this boundary
 227 will increase by a factor (eq. 2.2):

$$\langle \frac{\Delta E}{E} \rangle \approx \frac{4}{3}\beta^2 \quad (2.2)$$

228 Where $\beta = V/c$, corresponding to the boundary velocity. This is *second order Fermi*
 229 *acceleration*, and is generally insufficient to explain the cosmic ray spectrum. If we instead
 230 assume a plane shock front, as in figure 2.4 , then the post-collision velocity of the particle
 231 is no longer randomly distributed, and we instead obtain the expression (eq. 2.3):

$$\langle \frac{\Delta E}{E} \rangle \approx \frac{4}{3}\beta \quad (2.3)$$

232 This describes *first order Fermi acceleration*. From here, we can calculate the expected
 233 flux measured at Earth to be (eq. 2.4):

$$\frac{dN}{dE} \propto \left(\frac{E}{E_0}\right)^{-\Gamma} \quad (2.4)$$

234 where $\Gamma = \alpha + 1$, $\alpha \approx \frac{3P_e}{4\beta}$, and P_e is the probability that a particle may escape the
 235 shock region (proportional to the velocity, V). Note that this is a power law with almost
 236 constant spectral index, as both β and P_e are proportional to V , similar to what is seen in
 237 the observed cosmic ray spectrum [?].

238 We can additionally derive constraints on the maximum energy to which a particle can be
 239 accelerated based off the magnetic field intensity, B , and the size of the accelerating region,
 240 R (eq. 2.5):

$$E_{max} < eBR \approx 10^{21} \left[\frac{R}{1 \text{ pc}} \right] \left[\frac{B}{1 \text{ Gauss}} \right] \text{ eV} \quad (2.5)$$

241 This is known as *Hillas' condition*, and can inform us about the properties of cosmic
 242 ray accelerators. We can plot this condition to show sources which satisfy this requirement
 243 for a particular energy, producing what is commonly referred to as Hillas' plot (Figure 2.3).
 244 Sources must exist above the diagonal thresholds in order to be valid accelerators of cosmic
 245 rays of certain energies. For example, sources capable of accelerating protons to 100 EeV
 246 energies must exist above the dashed line in figure 2.3. Sources below are either too small,
 247 or have magenetic fields that are too weak.

248 2.2 Photons

249 Perhaps the oldest and most well-studied astrophysical messenger, photons have the useful
 250 property of being electrically neutral. Unlike cosmic rays, their paths are not bent by
 251 magnetic fields, and the arrival directions of photons can be used to identify their origin due
 252 to their good angular resolution. Photons additionally span a large energy range, and can
 253 be used to explore a wide variety of astrophysical production processes. For the purposes of
 254 this work, we are most interested in the highest energy photons (gamma rays, with energies
 255 greater than 100 keV), which can be produced through either leptonic or hadronic processes.

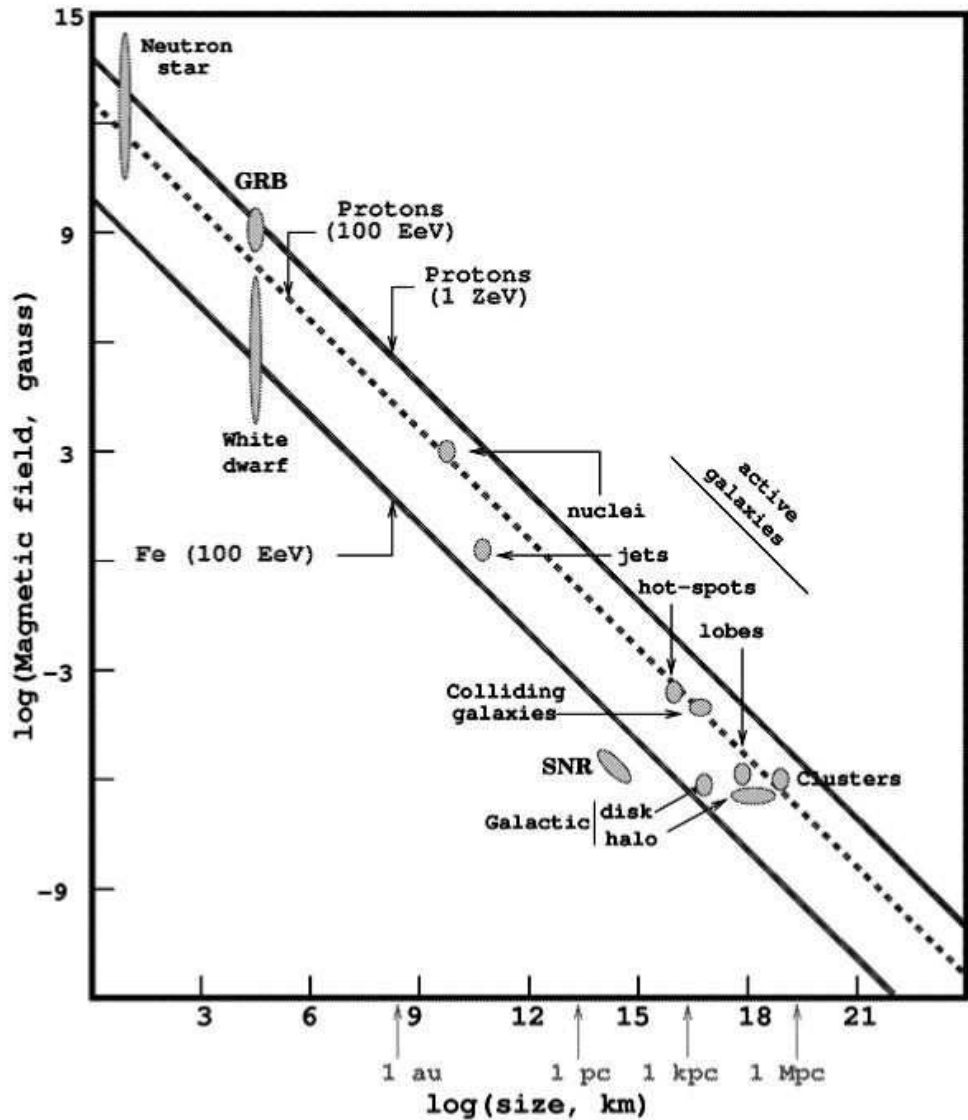


Figure 2.3: A Hillas plot, showing source populations capable of accelerating cosmic rays to a given energy, given their size and magnetic field strength [?].

256 2.2.1 Leptonic Radiative Processes

257 While photons cannot be directly accelerated by electric and magnetic fields, there are a
258 variety of mechanisms by which processes involving leptons can produce high energy photons.

- 259 • **Synchrotron radiation:** Radially accelerated relativistic particles will release syn-
260 chrotron radiation. This typically occurs as charged particles (such as electrons) spiral
261 through magnetic fields. The power loss, (dE/dT) , due to synchrotron radiation for a

262 particle of mass M and charge Z can be expressed as (eq. 2.6):

$$-\frac{dE}{dT} \approx 2.6 \left(\frac{Zm_e}{M}\right)^4 \left(\frac{E}{1 \text{ keV}}\right)^2 \left(\frac{B}{1 \text{ G}}\right)^2 \text{ keV s}^{-1} \quad (2.6)$$

263 Where m_e is the electron mass, E is the particle energy, and B is the magnetic field
 264 strength. From equation 2.6 it can be seen that synchrotron emission is significantly
 265 more relevant for electrons than protons, due to the $1/M^4$ term.

266 • **Compton Scattering and Inverse Compton Scattering:** Photons may scatter
 267 off an electron at rest, and in doing so experience a wavelength shift according to (2.7):
 268

$$\frac{\lambda' - \lambda}{\lambda} = \frac{\hbar\omega}{m_e c^2} (1 - \cos \alpha) \quad (2.7)$$

269 where λ' and λ correspond to the final and initial photon wavelengths, and α is the
 270 deflection angle of the photon. If a low energy photon collides with a high energy
 271 electron, the energy of the photon may exit with more energy than it began with,
 272 providing an effective mechanism for increasing the photon energy.

273 • **Bremsstrahlung:** Particles deflected by the electric field of the material they are
 274 traveling through emit photons, referred to as "bremsstrahlung". The fractional energy
 275 loss for a high energy electron due to bremsstrahlung can be described by:

$$\frac{1}{E} \frac{dE}{dX} \simeq -\frac{1}{X_0} \quad (2.8)$$

276 where X_0 is the radiation length of the material.

277 A combination of these two processes can produce the two peak structure typically seen
 278 in the spectrum of observed gamma ray sources. The lower energy peak is due to synchrotron
 279 radiation, while the higher energy peak corresponds to low energy photons being scattered
 280 to higher energies via inverse compton scattering.

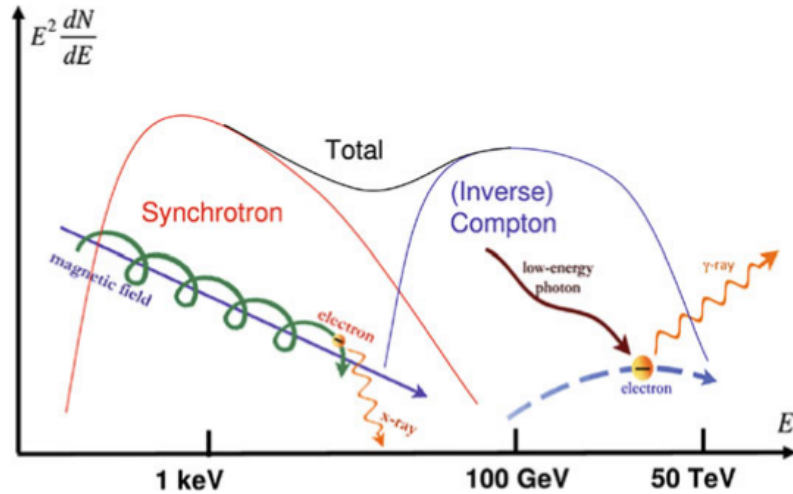


Figure 2.4: A cartoon plot of the gamma ray spectrum for a high energy gamma ray source. The two peak structure arises from the two production mechanisms of gamma rays. At lower energies, photons are produced by synchrotron radiation of electrons spiraling around magnetic field lines. The higher energy peak is then formed by the lower energy photons being scattered off energetic electrons via inverse compton scattering [?].

281 2.2.2 Hadronic Radiative Processes

282 While leptonic processes can produce high energy gamma rays, hadronic processes will pro-
 283 duce gamma rays in addition to neutrinos and cosmic rays. Protons accelerated to high
 284 energies in an astrophysical source may interact with other protons via (eq. 2.9):

$$p + p \rightarrow [\pi^0 + \pi^+ + \pi^-] + X \quad (2.9)$$

285 Where X is the appropriate nucleus or hadron depending on the pions produced, and on
 286 average there is expected to be equal production of neutral, positive, and negative charged
 287 pions. Additionally, protons may interact with photons, providing an additional path to
 288 pion production (eq. 2.10 and 2.11):

$$p + \gamma \rightarrow \Delta^+ \rightarrow \pi^0 + p \quad (2.10)$$

289

$$p + \gamma \rightarrow \Delta^+ \rightarrow \pi^+ + n \quad (2.11)$$

290 These resultant pions can subsequently decay, producing child particles depending on the
 291 particular pion type. Neutral pions will decay into gamma rays ($\pi^0 \rightarrow \gamma + \gamma$), and charged
 292 pions will decay to a lepton and their associated (anti)neutrino (most often muons and muon
 293 neutrinos: $\pi^+ \rightarrow \nu_\mu + \mu^+$, $\pi^- \rightarrow \bar{\nu}_\mu + \mu^-$). As such the sources of cosmic rays are expected
 294 to additionally produce a high energy gamma ray flux.

295 2.2.3 Gamma Rays as an Astrophysical Messenger

296 Gamma rays are a robust astrophysical messenger. As previously mentioned, photons are
 297 uncharged and their arrival directions can consequently be used to identify their origin.
 298 Additionally, the gamma ray energy can be used to infer information about the primary
 299 particle energy for a known production mechanism. Gamma rays are also well studied, and
 300 modern detectors boast high event rates: Fermi-LAT, for example, observes enough events to
 301 be capable of studying the temporal variability of sources on the timescale of approximately
 302 a day.

303 Gamma rays are not without their limitations, however. Note that while at the high-
 304 est energies gamma rays may be produced by both leptonic and hadronic processes, only
 305 hadronic processes are expected to additionally produce neutrinos and cosmic rays. For this
 306 reason, high energy gamma rays alone cannot be used to identify the source of high energy
 307 cosmic rays.

308 Additionally, high energy gamma rays ($E > 100$ GeV) may also interact electromagneti-
 309 cally with the ambient radiation in the universe, undergoing pair production (eq. 2.12):

$$\gamma_{VHE} + \gamma_{CMB} \rightarrow e^+ + e^- \quad (2.12)$$

310 This interaction can occur between high energy gamma rays and photons from the CMB,
 311 leading to an event horizon for gamma rays of a particular energy. Figure 2.5 shows this
 312 horizon as a function of distance and photon energy. The photon event horizon prevents us
 313 from studying the highest energy photons from many AGN, and there is a significant region

314 of parameter space below the highest observed cosmic ray energy that cannot be examined
 315 with photons alone.

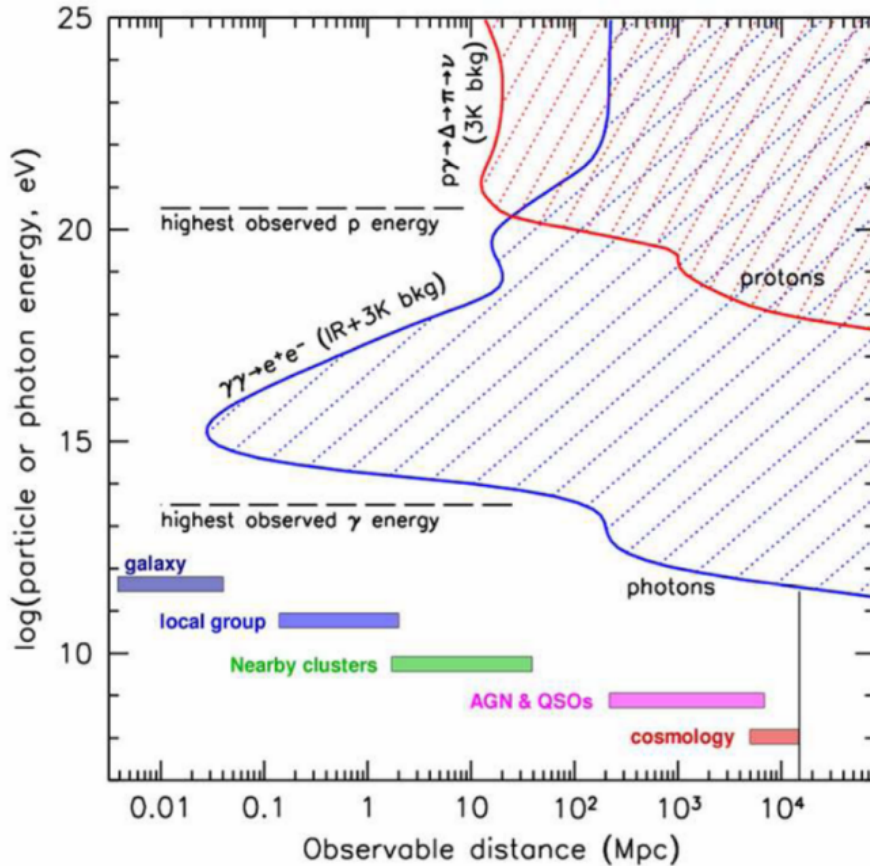


Figure 2.5: A plot of the photon and cosmic ray event horizons, showing the regions/energy scales visible using observations originating from photons (blue) and cosmic rays (red). Pair production of high energy photons with the ambient radiation in the universe prevents photon observations at long distances and high energies, including much of the energy scale below the highest observed cosmic ray energy. Also note that the photon event horizon can prevent us from studying the highest energy photons from AGN [?].

316 2.3 Neutrinos

317 2.3.1 Production Mechanisms

318 Neutrinos in astrophysical sources are produced via charged pion decay from pions pro-
 319 duced from cosmic ray interactions with either photons or protons. The charge of the pion

320 determines whether more neutrinos or anti-neutrinos are produced (eq. 2.13 and 2.14):

$$\pi^+ \rightarrow \nu_\mu + \mu^+ \rightarrow \nu_\mu + e^+ + \nu_e + \bar{\nu}_\mu \quad (2.13)$$

$$\pi^- \rightarrow \nu_\mu + \mu^- \rightarrow \bar{\nu}_\mu + e^- + \bar{\nu}_e + \nu_\mu \quad (2.14)$$

321 In either case, note that the expected flavor ratio of the neutrinos and anti-neutrinos
 322 produced at the source is $\nu_e : \nu_\mu : \nu_\tau = 1 : 2 : 0$. Combining this initial flavor ratio
 323 with neutrino oscillations over cosmic distances produces an expected observed astrophysical
 324 neutrino flavor ratio of $\nu_e : \nu_\mu : \nu_\tau = 1 : 1 : 1$.

325 Neutrinos are also produced by cosmic rays interacting with the Earth's atmosphere. This
 326 is referred to as the atmospheric neutrino flux, and has contributions both from pion decay
 327 ($\pi^+ \rightarrow \nu_\mu + \mu^+$, $\pi^- \rightarrow \bar{\nu}_\mu + \mu^-$), as well as kaon decay ($K_L^0 \rightarrow \pi^\pm + e^\mp + \nu_e$, $K_L^0 \rightarrow \pi^\pm + \mu^\mp + \nu_\mu$,
 328 $K^+ \rightarrow \mu^+ + \nu_\mu$, $K^+ \rightarrow \pi^0 + e^+ + \nu_e$, $K^+ \rightarrow \pi^0 + \mu^+ + \nu_\mu$). The resultant spectrum
 329 closely follows that of cosmic rays, with a spectral index of $\gamma_{atmos} = 2.7$. At higher energies
 330 the shower mesons are able to travel further in the atmosphere, giving them an increased
 331 opportunity to interact and steepening the spectral index to $\gamma_{atmos} = 3.7$, further reducing
 332 the atmospheric neutrino flux contribution at high energies. The atmospheric neutrino flux
 333 exists as an irreducible background for many studies of the origin of astrophysical neutrinos.

334 2.3.2 Observed Neutrino Spectrum

335 Both the astrophysical and atmospheric neutrino fluxes have been observed in data from
 336 the IceCube detector, with the astrophysical neutrino spectral index being measured to be
 337 $\gamma_{astro} \approx 2.28$ [?]. While astrophysical and atmospheric neutrinos are largely indistinguish-
 338 able on an individual event basis, the difference in spectra between the two populations
 339 ($\gamma_{astro} \approx 2.28$, $\gamma_{atmos} \approx 3.7$) allows us to distinguish between the two on a statistical ba-
 340 sis. Higher energy events are more likely to be astrophysical in origin, and an equal share
 341 of astrophysical and atmospheric neutrinos can be expected at ≈ 200 TeV. Currently, the

source(s) of the astrophysical neutrino flux have yet to be identified. For this reason, the observed astrophysical neutrino flux is commonly referred to as the "diffuse" astrophysical neutrino flux (as opposed to a "point source" flux, where specific astrophysical objects that are producing neutrino are identified).

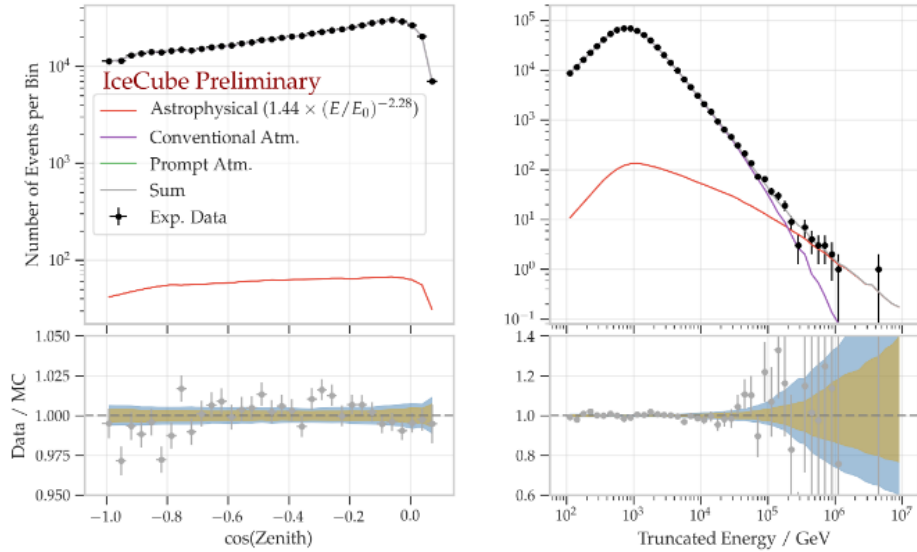


Figure 2.6: Observation of the astrophysical neutrino flux in through-going tracks detected by the IceCube Neutrino Observatory. The effect is most visible in the plot of the observed energy spectrum on the right, showing the atmospheric contribution (blue) and the astrophysical contribution (red). The excess of events at high energies is unable to be explained without including a non-zero astrophysical contribution [?].

2.3.3 Neutrinos as Astrophysical Messengers

As noted in the previous section, hadronic processes in astrophysical sources can produce neutrinos via pion decay. Like gamma rays, neutrinos are electrically neutral, and thus their paths are not bent by magnetic fields. Unlike gamma rays, however, neutrinos do not interact electromagnetically, instead interacting only via the weak force. Because of this, the mean free path of neutrinos traveling through the universe is significantly greater than that of photons, allowing us to use neutrinos to probe regions normally opaque to gamma rays.

354 Astrophysical neutrinos are not without their drawbacks, however. The fact that neutrinos
 355 interact only weakly necessitates the construction of large detectors in order to observe
 356 an appreciable number of astrophysical events. Such detectors also observe a large, irre-
 357 ducible background of atmospheric neutrinos, particularly at lower (TeV) energies. For this
 358 reason, multi-messenger approaches that combine information from neutrinos and other as-
 359 trophysical messengers are commonly used to attempt to identify the sources of astrophysical
 360 neutrinos.

361 **2.3.4 AGN as Neutrino Source Candidates**

362 Since neutrinos can be used as an indicator of hadronic processes in astrophysical sources,
 363 identifying the source of the astrophysical neutrino flux is a promising route to also identi-
 364 fying the source of ultra-high energy cosmic rays. Though the source of the astrophysical
 365 neutrino flux has yet to be fully determined, in recent years there have been promising hints
 366 that extragalactic AGN are at least partially responsible.

367 An active galactic nucleus (AGN) is a compact region at the center of a galaxy displaying
 368 elevated electromagnetic emission, such that the additional luminosity cannot be attributed
 369 to stars. The luminosity is expected to originate from the accretion disk surrounding a
 370 supermassive black hole at the center of the galaxy, where conditions are thought to be ideal
 371 for high-energy particle acceleration and production.

372 The presence and angle relative to earth of the AGN jet (a beam of outflowing ionized
 373 matter extending along the axis of rotation) determines its exact classification, as can be
 374 seen in figure 2.7. If the AGN is viewed "down" the jet (i.e. the jet is directed at Earth),
 375 the AGN is seen to be particularly luminous and is referred to as a blazar or BL Lac object.
 376 Blazars can be further divided into two subclasses: flat spectrum radio quasars (FSRQ),
 377 which have luminous broad emission lines and continuous thermal emission, and BL-Lacs,
 378 which have weak or absent broad emission lines. AGN viewed off-axis fall into a variety
 379 of other classifications, with further sub-classification being defined by the spectrum of the

380 AGN in various wavelength bands.

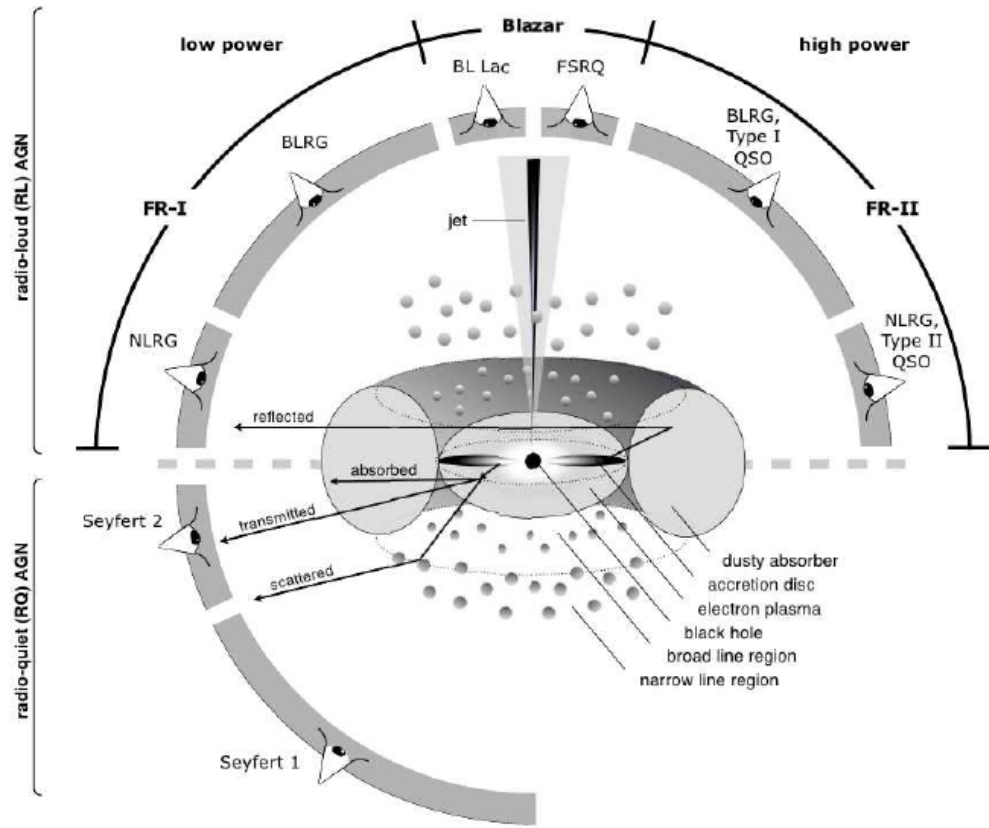


Figure 2.7: The unified AGN model, showing the various classifications of AGN for different observation angles. If the jet is directed at Earth, the object is viewed as a blazar, while other viewing angles can obscure the jet, leading to alternative classification (e.g. as a Seyfert galaxy) [?].

381 2.3.4.1 TXS 0506+056

382 On September 22, 2017, the IceCube Neutrino Observatory detected a high energy neu-
 383 trino, IceCube-170922A, with an energy of approximately 290 TeV. The arrival direction of
 384 IceCube-170922A was consistent with the location of the blazar TXS 0506+056, and sparked
 385 multi-messenger followup from a variety of other telescopes and detectors. Notably, it was
 386 determined that TXS 0506+056 was flaring in gamma rays at the time IC-170922A was
 387 observed. The significance of the positional correlation of a high energy IceCube event and
 388 a flaring blazar was calculated to be 3.0σ , providing the first hint that blazars may be a
 389 source of high energy astrophysical neutrinos [2].

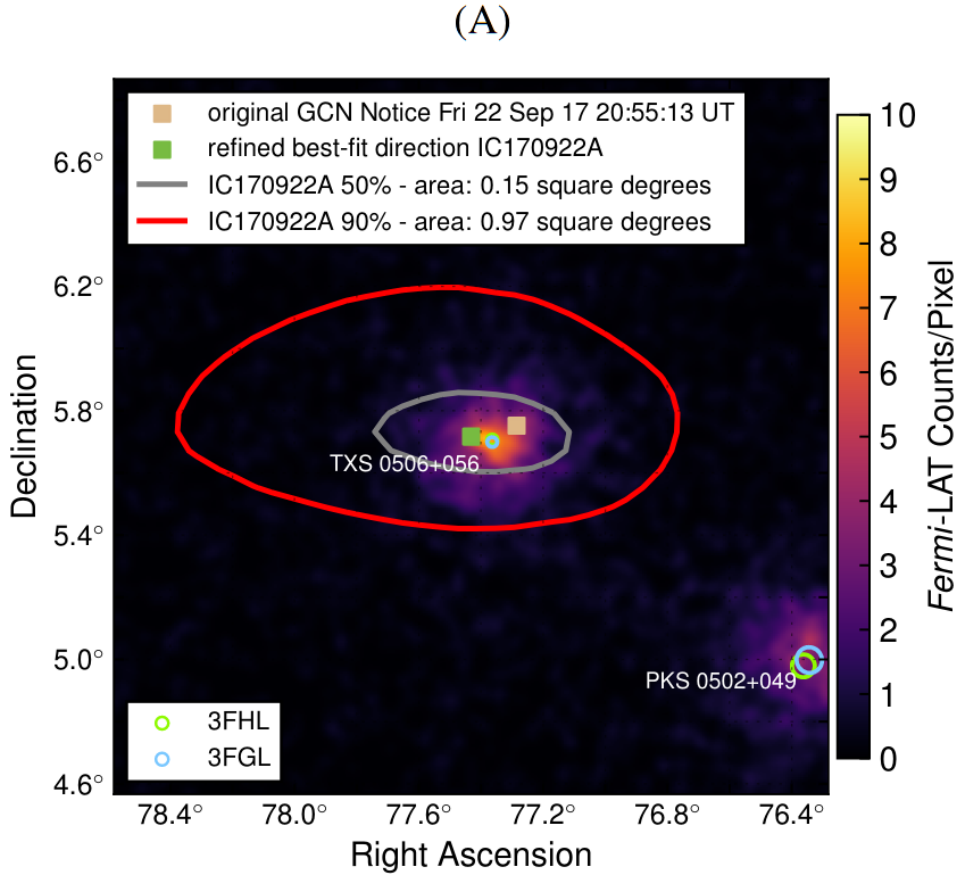


Figure 2.8: The Fermi-LAT skymap near the location of the observed high energy IceCube event IC170922A, with the 50% and 90% error contours associated with IC170922A plotted in grey and red, respectively. The significance associated with the spatial coincidence of the high energy event and TXS 0506+056 was found to be 3.0σ [2].

390 In addition to examining the multi-messenger correlation of a high energy IceCube event
 391 and a flaring blazar, an analysis of archival IceCube data was performed at the coordinates
 392 of IC170922A, examining the historical behavior of neutrino emission from this location of
 393 the sky over the previous nine years. In addition to the original high energy event observed
 394 in 2017, this archival analysis also revealed a 158 day period of elevated neutrino emission
 395 beginning in September 2014. The significance of this archival "neutrino flare" was calculated
 396 to be 3.5σ . Unlike the 2017 high energy event, the 2014 neutrino flare did not correspond
 397 to a flaring period for TXS 0506+056 in gamma rays. [3]

398 The combination of a 3.0σ multimessenger result with the 3.5σ "untriggered" neutrino

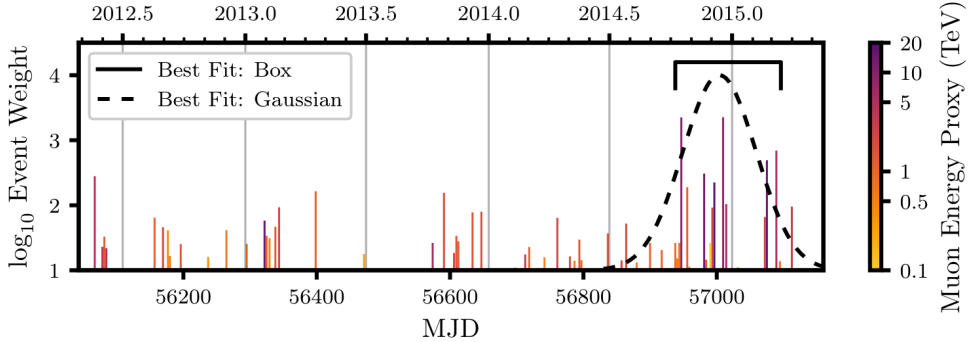


Figure 2.9: The result of the archival analysis of IceCube data near the location of TXS 0506+056, with the 3.5σ flare shown. This flare is separate from the high energy event observed in 2017, and there was no corresponding flare observed in gamma rays during this time period [3].

399 flare in 2014 suggest a significance of TXS 0506+056 as a neutrino source of at least 3σ .
 400 This makes for a strong argument for extragalactic blazars as interesting source candidates
 401 from the perspective of neutrino astronomy.

402 2.3.4.2 NGC 1068

403 In addition to the multimessenger and archival results associated with TXS 0506+056, the
 404 results of the 10-year time integrated IceCube analysis [4] also seem to suggest AGN as
 405 candidates for astrophysical neutrino emission. In this all-sky, untriggered, time integrated
 406 analysis, the most significant point in the northern sky appears to be spatially coincident
 407 with the Seyfert II galaxy NGC 1068. Notably, NGC 1068 was also included in an associated
 408 time integrated catalog analysis. In this catalog analysis, the pre-trial significance of time-
 409 integrated neutrino emission from NGC 1068 was 1.8×10^{-5} , corresponding to a significance
 410 of 2.9σ . At a 14.4 Mpc distance, NGC 1068 is the most luminous Seyfert II galaxy detected
 411 by Fermi-LAT, and NGC 1068 had additionally been hypothesized as a candidate cosmic
 412 ray accelerator prior to this particular analysis [?][?][?].

413 It should additionally be noted that the catalog analysis mentioned above identified
 414 three other objects which, together with NGC 1068, collectively form a 3.3σ excess over
 415 the background expectation. These objects are the Seyfert II galaxy NGC 1068, the blazar

416 TXS 0506+056, and the BL Lacs PKS 1424+240 and GB6 J1542+6129 [4], providing further
 417 indication of AGN as potential neutrino emitters.

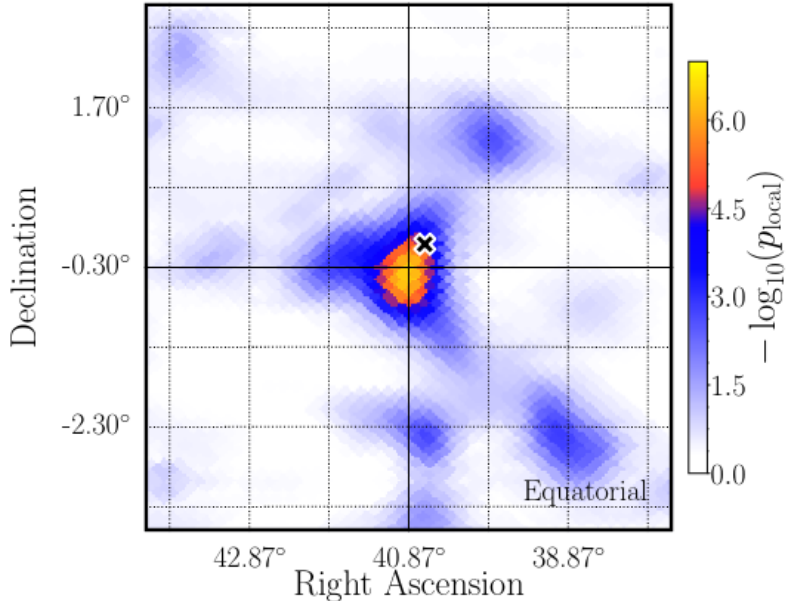


Figure 2.10: The results of the untriggered time integrated IceCube point source search analysis, showing the most significant spot in the northern sky, with the location of NGC 1068 plotted as the black "X" [4].

418 2.3.5 Galactic Neutrino Sources

419 Though this work will primarily focus on searches for extra-galactic point sources of the
 420 astrophysical neutrino flux, potential neutrino emission from sources within our galaxy is
 421 an active area of study as well. Notably, one of the first confirmed sources of lower energy
 422 astrophysical neutrinos was Supernova 1987A [?], a supernova occurring within the Large
 423 Magellanic Cloud. Other galactic objects that are considered candidates for neutrino emis-
 424 sion include supernova remnants [?], as well as pulsar wind nebula [?], both of which are
 425 known to produce gamma rays.

426 The galactic center and the majority of galactic source candidates lie in the southern
 427 hemisphere. Since neutrino telescopes make use of the earth to block out atmospheric muon

428 backgrounds (see subsequent chapter), this means that to best study the galactic plane, a
 429 neutrino observatory located in the northern hemisphere would be required. While there are
 430 several such telescopes either planned or under construction [?][?], they have yet to reach
 431 effective volumes comparable to the existing IceCube observatory (located in the southern
 432 hemisphere).

433 2.3.6 Constraints on Neutrino Source Populations from Diffuse 434 Measurements

435 It is important to keep in mind that whatever the sources of astrophysical neutrinos may
 436 be, they must combine to reproduce the measured diffuse astrophysical neutrino flux. The
 437 current best fit astrophysical neutrino spectrum, assuming a single power law in energy, is
 438 given as (eq. 2.15) [?]:

$$\frac{d\phi_{\nu+\bar{\nu}}}{dE} = 1.44^{+0.25}_{-0.24} \left(\frac{E}{100\text{TeV}}\right)^{-2.28^{+0.08}_{-0.09}} 10^{-18} \text{GeV}^{-1}\text{cm}^{-1}\text{s}^{-1}\text{sr}^{-1} \quad (2.15)$$

439 This places constraints on the density and luminosity of potential astrophysical neutrino
 440 source populations. If a candidate source population has sources that are too numerous
 441 and/or too bright, that that source class would likely have already been detected by existing
 442 neutrino point source searches, or in more extreme cases, that source population would
 443 produce a higher flux of astrophysical neutrinos than has been observed, and an explanation
 444 of the nondetection of the additional flux is required. Similarly, if sources are too sparse
 445 and/or too dim, then such a source class is incapable of explaining the entirety of the
 446 measured diffuse flux.

447 These constraints can be summarized in figure 2.11, showing the band of the measured
 448 diffuse flux in source density/luminosity space, as well as several commonly discussed source
 449 populations. It should be noted that in this plot, the luminosity values for various source
 450 populations are derived from the electromagnetic luminosity L_γ . In principle, the true ratio

451 L_ν/L_γ remains unknown, and consequently the positions of sources along the luminosity axis
 452 may shift according to this value.

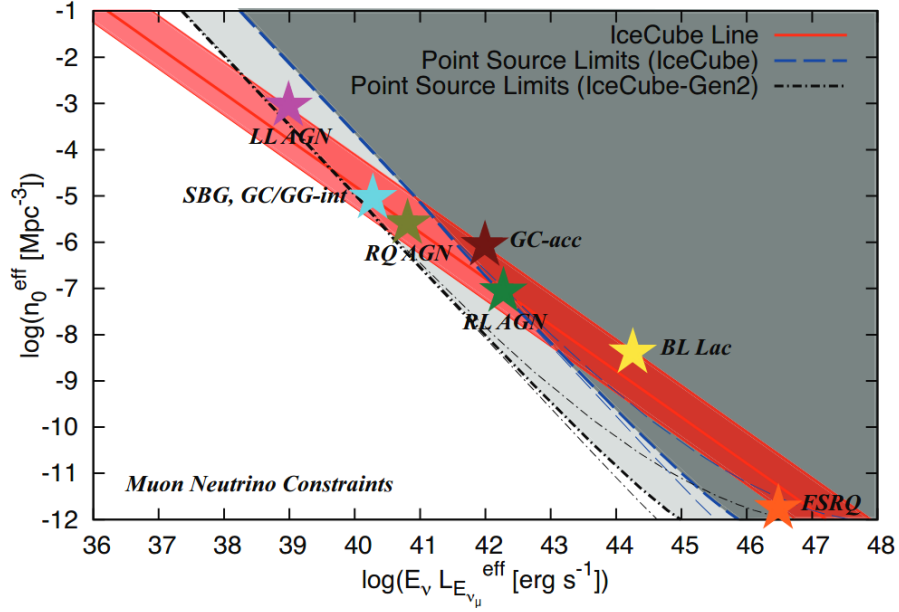


Figure 2.11: Constraints on potential populations of sources of the high energy astrophysical neutrino flux. The red band represents combinations of source density and luminosity that are consistent with the measured astrophysical neutrino flux. Source populations that lie above this band are too bright and/or too numerous, while source below this band are too dim/too sparse. Also shown are limits derived from the non-observation of neutrino sources in time-integrated analyses performed by the IceCube collaboration as of 2016, as well as a projected set of limits that would be associated with a non-observation from IceCube-Gen2. Stars mark the expected properties of various source classes, as calculated in [?].

⁴⁵³ **Chapter 3**

⁴⁵⁴ **The IceCube Detector**

⁴⁵⁵ The IceCube Detector is a large (cubic kilometer scale) water cherenkov detector situated
⁴⁵⁶ underneath the ice at the south pole. Its large volume makes it ideal for studying high energy
⁴⁵⁷ (TeV and higher) neutrino events originating from either the atmosphere or astrophysical
⁴⁵⁸ sources.

⁴⁵⁹ **3.1 Detection Mechanism**

⁴⁶⁰ The cross section for neutrino interaction in Earth can be seen in figure 3.1. These cross
⁴⁶¹ sections are small, but the Earth is also quite large. We can calculate the mean free path
⁴⁶² for neutrinos traveling through Earth as (eq. 3.1):

$$\lambda = \frac{1}{\sigma_\nu \rho_{Earth}} \quad (3.1)$$

⁴⁶³ Using the neutrino cross section near 1 PeV ($\sigma_\nu \approx 1.15 \times 10^{-33} \text{ cm}^2$) [?], and the density
⁴⁶⁴ of the Earth ($\approx 5.5 \text{ g/cm}^3$, corresponding to a nucleon density of $\rho_{Earth} = 3.3 \times 10^{24} \text{ cm}^{-3}$),
⁴⁶⁵ we obtain an estimate of the neutrino mean free path of $\approx 2600 \text{ km}$. Since the diameter
⁴⁶⁶ of the Earth is approximately $1.3 \times 10^4 \text{ km}$, we can conclude that the Earth is opaque to
⁴⁶⁷ high energy neutrinos. We can detect the neutrinos that interacted in the Earth by way of
⁴⁶⁸ identifying their interaction products.

469 For the purposes of neutrino point source searches, we primarily focus on neutrinos
 470 interacting either through charged current (CC) or neutral current (NC) interactions. In
 471 both cases, the energy of the neutrinos observed by the IceCube detector is high enough
 472 that neutrinos interact through deep inelastic scattering with nucleons in the antarctic ice.
 473 In neutral current (NC) interactions, the process is mediated by a neutral Z boson, as shown
 474 on the left in figure 3.2. In this case, the product of the interaction is a neutrino, meaning
 475 the only visible signature of this interaction is the production of a hadronic particle cascade.

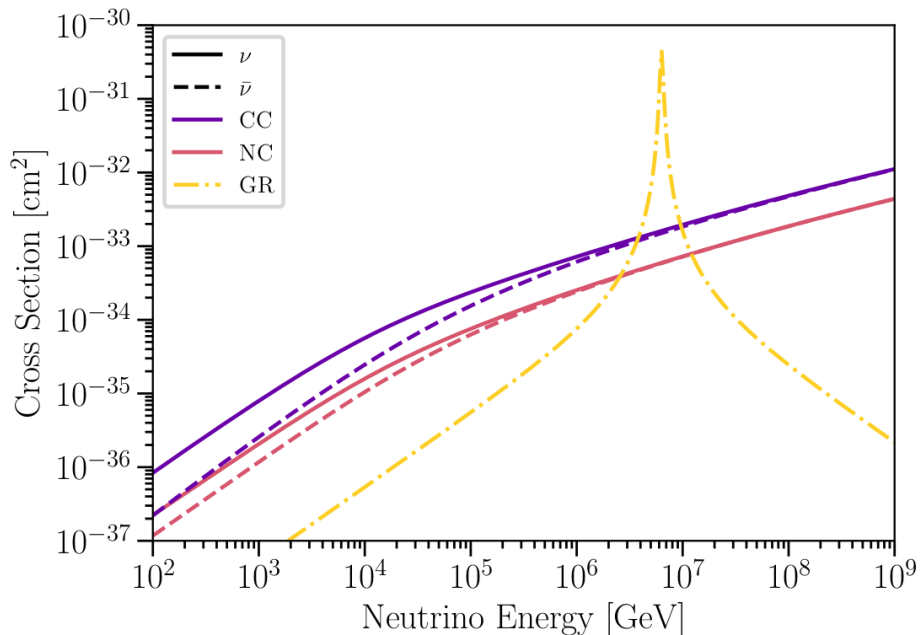


Figure 3.1: The cross sections of various neutrino interactions in the Earth. The yellow curve corresponds to Glashow Resonance [?], whereby an anti-electron neutrino combines with an atomic electron to produce a W+. These events are relatively rare in IceCube data, and are subsequently not used in the context of astrophysical neutrino source searches. Figure from [?].

476 Charged current interactions are mediated by a charged W boson, and can be summarized
 477 as (eq. 3.2 and 3.3):

$$\nu_\ell + n \rightarrow \ell^- + p \quad (3.2)$$

478



479 The Feynman diagrams for this process can be seen on the right in figure 3.2. Notably,
 480 charged current interactions produce an outgoing lepton ℓ in addition to a hadronic cascade.
 481 This is particularly useful in the case that the lepton produced is a muon, as muons can
 482 travel a sizeable distance (hundreds, or even thousands of meters) before decaying. If the
 483 lepton receives enough energy, it will subsequently produce cherenkov radiation, as it will
 484 be traveling faster than the local speed of light in ice. This radiation is emitted at an angle
 485 θ_c relative to the direction of travel, where θ_c is given by (eq. 3.4):

$$\cos(\theta_c) = \frac{1}{n\beta} \quad (3.4)$$

486 Where n is the index of refraction of the medium through which the particle is traveling
 487 (in this case ice), $\beta = \frac{v}{c}$, and v is the velocity of the traveling particle (the lepton, in this
 488 case). For ice, $n = 1.31$, and this emission angle is approximately 41 degrees. The number
 489 of photons expected per unit track length is given by the Frank-Tamm formula [?] (eq. 3.5):

$$\frac{dN}{dx d\lambda} = \frac{2\pi z\alpha}{\lambda^2} \sin^2(\theta_c) \quad (3.5)$$

490 Where z is the charge of the ionizing particle, λ is the wavelength of the emitted radiation,
 491 α is the fine structure constant ($\approx \frac{1}{137}$), and θ_c is the cherenkov angle given by eq. 3.4. Peak
 492 emission is found in the optical portion of the light spectrum, between 350 and 600 nm
 493 corresponding to a characteristic blue hue.

494 To summarize, neutrinos traveling through the antarctic ice will occasionally interact,
 495 producing child particles that will emit cherenkov radiation. We can then build an array
 496 of photon detectors to detect these photons, and subsequently infer information about the
 497 original incident particles.

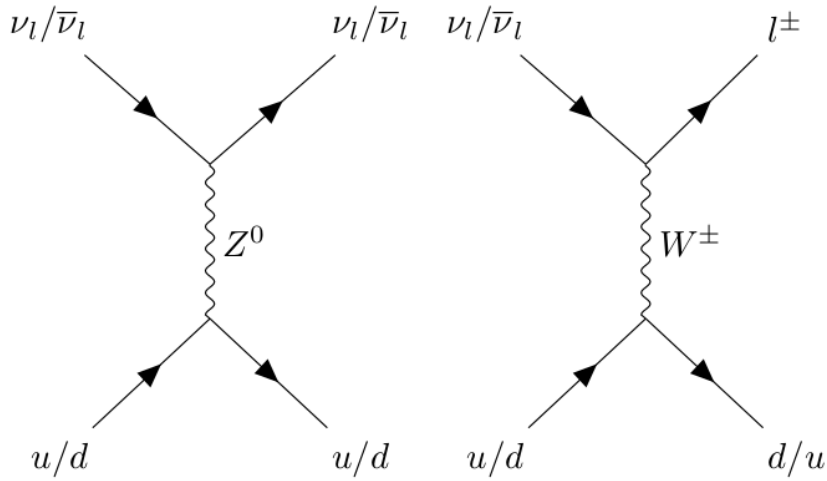


Figure 3.2: The Feynman diagrams corresponding to neutral current (left) and charged current (right) neutrino interactions. Charged current interactions can produce a detectable outgoing lepton in addition to a hadronic cascade, while neutral current interactions only produce a hadronic cascade.

498 3.2 The Physical Components of the IceCube

499 Detector

500 As outlined in the previous section, the strategy for detecting neutrinos with a water
 501 cherenkov detector is not to directly detect the neutrinos themselves, but rather to detect
 502 the cherenkov photons from the outgoing particles resulting from the neutrino interactions.
 503 The IceCube detector accomplishes this through the use of a large number of photomultiplier
 504 tubes (PMTs). At the very highest level, a PMT is a device that converts photons to an
 505 electrical signal that can then be read out by a set of associated electronics. The details of
 506 general PMT design and operation can be found in [?].

507 In IceCube, PMTs are housed in a single unit referred to as a digital optical module
 508 (“DOM”), seen in figure 3.3. Each module contains the PMT and its associated electronics,
 509 as well as a set of LED flashers that can be used to calibrate the detector once the DOMs have
 510 been lowered into the ice. DOMs are arranged onto 86 vertical strings, 78 of which contain
 511 60 DOMs spaced 17 meters apart along the length of the string. These strings are arranged

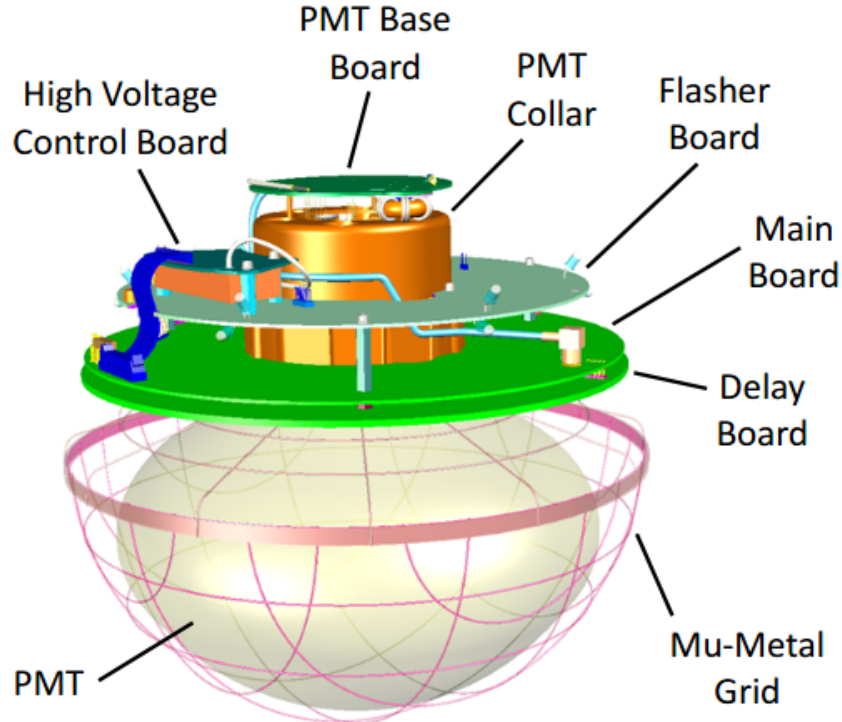


Figure 3.3: A diagram of a single IceCube digital optical module (DOM). The entire apparatus is encased in a pressurized glass sphere for protection (not shown). The PMT faces downward for optimal collection of photons from upgoing neutrino events. In addition to the PMT, each DOM also contains digitization electronics and an array of LED flashers that can be used for calibration [?].

512 into a hexagonal grid pattern under the south pole ice with a separation between strings
 513 of approximately 125 meters, resulting in a cubic kilometer of instrumented ice extending
 514 between 1450 and 2450m below the surface of the south pole ice sheet. The remaining 8
 515 strings form the DeepCore sub-array, a more densely instrumented region near the center of
 516 the detector, primarily used for studying lower (\approx 100s of GeV) scale events. PMTs that are
 517 part of the DeepCore portion of the detector have a higher quantum efficiency than those
 518 on the other 78 strings [?].

519 A diagram of the IceCube detector can be seen in figure 3.4. Due to the weakly interacting

520 nature of neutrinos combined with a power law spectrum, a large detector volume is critical
 521 to detecting the astrophysical neutrino flux. Prior to IceCube's construction, calculations
 522 based on the likely linkage of neutrinos to the observed high energy cosmic ray flux indicated
 523 that a cubic-kilometer scale detector would be necessary to observe an appreciable event
 524 rate of astrophysical neutrinos [?][?]. The size and design of IceCube are well suited for
 525 detecting astrophysical neutrino events in the TeV+ energy range, as the large instrumented
 526 volume ensures a significant number of interactions in this energy range, and the detector's
 527 nanosecond scale timing resolution makes event reconstruction possible for events producing
 528 cherenkov radiation over the scale of ≈ 100 s of meters.

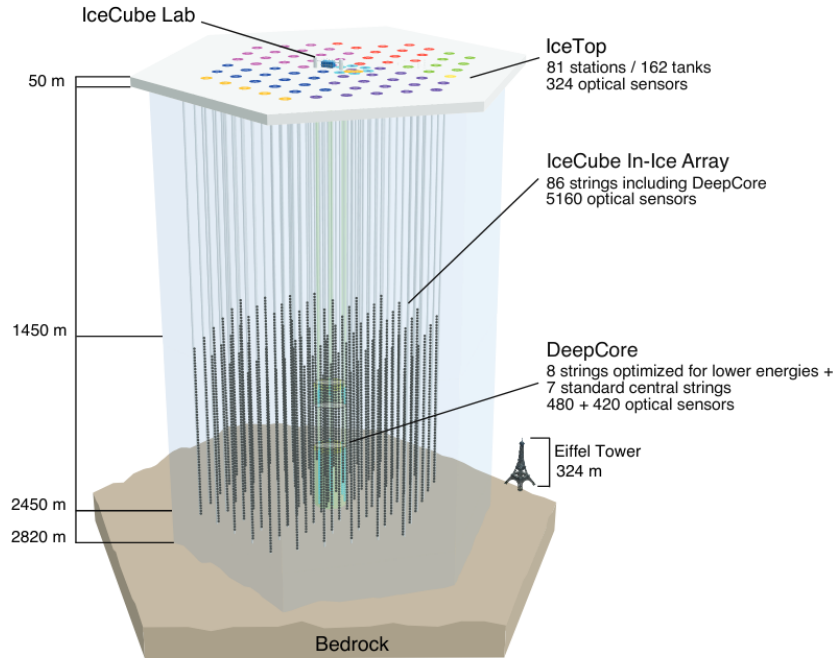


Figure 3.4: A diagram of the IceCube detector. The detector consists of 86 strings of DOMs lowered into holes drilled in the pattern of a hexagonal grid defined by a separation of 125 meters. Each string is formed by 60 DOMs connected by a cable, used for powering the DOMs and communication with the IceCube Lab (ICL) on the surface. The instrumented detector volume begins at a depth of 1450 meters, and extends down to 2450 meters, resulting in approximately a cubic kilometer of instrumented ice [?].

529 As the IceCube detector is situated in the south pole ice, a proper description of the
 530 optical properties of the ice is key for being able to accurately reconstruct events. While the

531 ice is generally clear, it does contain several impurities and features that make it optically
 532 nonuniform. The scattering and absorbtion of light are known to vary as a function of depth,
 533 as seen in figure 3.5. The large peak near a depth of 2000 meters is thought to correspond to
 534 a layer of dust deposited on the south pole ice sheet many years in the past, and is commonly
 535 referred to as “the dust layer” (physicists are not always the most creative with names).

536 In addition to varying as function of depth, the optical properties of the ice also vary as
 537 a function of azimuth. The largest effects along this axis are the ice tilt and ice anisotropy.
 538 The ice tilt refers to the layers of ice with similar optical properties being not perfectly
 539 horizontal, and results in a variation in scattering and absorption as light travels in different
 540 directions through the ice sheet. The ice anisotropy is similar, but has an observed additional
 541 axis of symmetry, leading to variations that are twice as frequent as a function of azimuth.
 542 Notably, while this effect was original observed in calibration data using LED flashers, it is
 543 visible in data from observed atmospheric muons, as seen in figure 3.6.

544 The final major optical nonuniformity of the detector ice is the hole ice. During the
 545 construction of the IceCube detector, holes were drilled in the south pole ice, and strings
 546 of DOMs were lowered down the appropriate depth. The water in these holes then refroze
 547 with different optical properties than the surrounding ice. The column of refrozen ice is
 548 referred to as the “hole ice”, typically containing an inner region where air bubbles have
 549 been trapped referred to as the “bubble column”. The hole ice has significantly shorter
 550 scattering distances, and is an area of active study within the IceCube collaboration.

551 3.3 Event Types

552 IceCube events can be generally be categorized into three different types: tracks, cascades,
 553 and double cascades. While neutral current events exclusively correspond to cascades,
 554 charged current events can produce any of the three, dependent on the variety of the out-
 555 going lepton. This gives IceCube the ability to identify the flavor of the incident neutrino,
 556 and this fact can be leveraged to do a large amount of interesting physics. However, for the

557 purposes of this work, we are primarily interested in tracks, due to their excellent pointing
 558 resolution as discussed below.

559 **3.3.1 Tracks**

560 From equation 3.2 we can see that charged current interactions produce an outgoing lepton,
 561 which will in turn produce cherenkov radiation if it is energetic enough. In particular, if the
 562 outgoing particle is a muon, it will travel a significant distance before decaying or exiting the
 563 detector. As the muon produces cherenkov radiation as it travels through the ice, the pattern
 564 of DOMs which detect this radiation will resemble a line, as shown in figure 3.7. These events
 565 are referred to as “tracks”. If the neutrino interaction occurred inside the IceCube detector,
 566 then the track will appear to start within the detector, and the event can be referred to as
 567 a “starting track”. If instead the neutrino interaction occurred outside the detector, and
 568 the resultant muon traveled through the detector, then the event is instead referred to as a
 569 “through-going track” (again, physicists are not the most creative). Through-going tracks
 570 can result from astrophysical neutrinos, as well as atmospheric neutrinos and atmospheric
 571 muons (muons resulting from cosmic ray interactions in the atmosphere). Starting tracks,
 572 however, can only be produced by muons originating from atmospheric or astrophysical
 573 neutrinos. For the purposes of this work, we will focus primarily on through-going tracks,
 574 however starting tracks are also scientifically interesting, and can be used for point-source
 575 and diffuse analyses of the neutrino flux as well [?].

576 Through-going tracks are notable for their good angular resolution (up to 0.25 degrees
 577 at high energies), particularly at high energies (> 1 TeV), as seen in figure 4.1. This makes
 578 them an excellent candidate for attempting to do astronomy, as they can be expected to
 579 point back to their point of origin with reasonable accuracy. Energy reconstruction of these
 580 events is somewhat more challenging, however, due to a combination of stochastic energy
 581 losses of the muon producing the cherenkov photons, and the fact that the event itself is
 582 often not entirely contained in the detector. The energy resolution of tracks in IceCube is

583 approximately a factor of 2 at 10 TeV, though this increases for higher energy events [?].

584 3.3.2 Cascades

585 Neutral current neutrino interactions will always produce a hadronic cascade and an outgoing
 586 neutrino which is not detectable. Charged current interactions will produce a hadronic
 587 cascade in addition to an outgoing lepton. If the outgoing lepton is a muon (or potentially an
 588 extremely energetic tau), the track morphology described above is produced. If the incident
 589 neutrino is a ν_e , resulting in an outgoing electron, which in turn results in an electromagnetic
 590 shower that has an extension of ≈ 10 meters. The cascade morphology produced in this case
 591 is indistinguishable from the hadronic cascade produced by charged current interactions.
 592 While cascades tend to have relatively poor ($\approx 5^\circ$) pointing resolution [?] due to their
 593 spherical symmetry, they have excellent energy resolution, as even for high energy events, the
 594 entirety of the cascade is often contained within the detector, making energy reconstruction
 595 as simple as counting the total number of cherenkov photons produced. The energy resolution
 596 of cascades is approximately 15%, potentially even lower at higher energies [?].

597 3.3.3 Double Cascades

598 If the outgoing lepton from a CC interaction is a tau, then the tau will decay with an
 599 average decay length of 50 meters/PeV, potentially observable above energies of 200 TeV. If
 600 the initial tau is high enough energy, this can produce a signature of two spatially separated
 601 hadronic cascades in the detector. If the tau is lower energy, the two cascades may not be
 602 spatially resolvable, though may still be able to be identified by examining the waveforms
 603 observed by hit DOMs. This type of event was only recently observed in IceCube data
 604 [?]. Notably, tau events of these energies are not expected to be produced by atmospheric
 605 processes, and consequently this observation provides further evidence of an astrophysical
 606 neutrino flux.

607 3.4 Triggering

608 IceCube DOMs are subject to dark noise in the detector originating from PMTs emitting
 609 electrons from the cathode in the absence of an external photoelectron. Dark noise below 0°
 610 celsius is primarily caused by radioactivity in the PMT and DOM glass. This noise should
 611 not be correlated between nearby DOMs, and can be dramatically reduced by imposing the
 612 triggering requirement that neighboring DOMs also experience a signal with $1 \mu s$. These
 613 hits are classified as “Hard Local Coincidence” (HLC). An eight-channel simple majority
 614 trigger (SMT8) is used to trigger a readout window where DOM information is written to
 615 file. This trigger requires eight DOMs to have HLC hits within a $5 \mu s$ window.

616 Events are further filtered through several additional algorithms to pare down events
 617 based on temporal and spatial coincidence of DOM hits. The result is a “Level 2” event rate
 618 of approximately 2.5 kHz. These events can be additionally filtered to select specifically for
 619 high quality track-like events (originating mostly from atmospheric muons, but also from
 620 atmospheric and astrophysical muon neutrinos as well), reducing the event rate to a few
 621 Hz. The most relevant cuts that are used to achieve this are cuts on zenith and total
 622 charge deposited, which together form the IceCube “MuonFilter” [?]. This level of data
 623 is often referred to within the collaboration as “Muon Level 3”, and primarily consists of
 624 through-going track-like events.

625 3.5 Directional Reconstruction

626 In this section we discuss algorithms for reconstructing the direction of through-going track
 627 events observed by the IceCube detector. Different algorithms may be used for cascades,
 628 though understanding these is unimportant for the remaining content of this thesis. Those
 629 who are interested in the reconstruction of cascade and double cascade events can refer to
 630 [?].

631 **3.5.1 LineFit**

632 An initial guess for the reconstructed direction of the track can be obtained by ignoring the
 633 geometry of the cherenkov cone and the optical properties of the ice, and assuming a plane
 634 wave of light traveling along a straight line in the detector. The location of each DOM that
 635 observes photons (\mathbf{r}_i) can then be written as a line (eq. 3.6):

$$\mathbf{r}_i = \mathbf{r} + \mathbf{v} \cdot t_i \quad (3.6)$$

636 Where t_i is the time that the i th DOM observes photons, \mathbf{r} is the vertex of the track,
 637 and \mathbf{v} is the velocity of light in the ice. A χ^2 fit can then be preformed to determine the
 638 free parameters \mathbf{r} and \mathbf{v} (eq. 3.7):

$$\chi^2 \equiv \sum_{i=1}^{N_{tot}} (\mathbf{r}_i - \mathbf{r} - \mathbf{v} \cdot t_i)^2 \quad (3.7)$$

639 This can be solved analytically, resulting in fitted vectors for \mathbf{r} and \mathbf{v} (eq. 3.8 and 3.9):

$$\mathbf{r} = \langle \mathbf{r}_i \rangle - \mathbf{v} \cdot \langle t_i \rangle \quad (3.8)$$

$$\mathbf{v} = \frac{\langle \mathbf{r}_i \cdot t_i \rangle - \langle \mathbf{r}_i \rangle \cdot \langle t_i \rangle}{\langle t_i^2 \rangle - \langle t_i \rangle^2} \quad (3.9)$$

640 This corresponds to a vertex (\mathbf{r}) and a direction (\mathbf{v}) describing the path of the particle.
 641 Further discussion on this topic can be found in [?].

642 **3.5.2 SplineMPE**

643 An improved reconstruction of the particle direction can be obtained by iterating on the
 644 initial LineFit reconstruction described above. The LineFit result is treated as a seed for
 645 a likelihood based reconstruction that takes the cherenkov angle and ice properties into
 646 account. A description of the specific likelihood components may be found in section 3 of
 647 [?]. In the simplest implementation of this likelihood method, only information from the

648 first photoelectron observed by a particular DOM is used. This is referred to as a single
 649 photoelectron fit, or “SPEFit”. For events that produce multiple hits on a single DOM,
 650 this information can be included in the likelihood as well, producing a multi-photoelectron
 651 (MPE) fit. Since photons arriving after the first are likely to have experienced at least
 652 some scattering, a proper description of the ice properties is necessary for an accurate MPE
 653 fit. This is incorporated into the likelihood described in [?] via the use of tabulated timing
 654 and light yield distributions for various DOM/photon configurations given an ice model
 655 developed from fits to LED flasher data [?]. The information in these tables is stored via
 656 a multi-dimensional spline, allowing these tables to be used directly as PDFs in the MPE
 657 likelihood, hence the name for this variety of reconstruction: “SplineMPE”.

658 3.5.3 Paraboloid

659 There is some inherent uncertainty associated with the observation and reconstruction of a
 660 particular event. For an event originating from a particular true position, the reconstructed
 661 position is expected to be drawn from distribution centered on the true position. Properly
 662 describing this distribution is key to characterizing the per-event uncertainty associated
 663 with the directional reconstruction, and is important for obtaining accurate results in a
 664 point source analysis.

665 A semi-analytic description of the angular error associated with a particular event can
 666 be obtained from the likelihood map associated with the direction reconstruction outlined
 667 in the previous section. An ellipse can be fit around the global minimum of the likelihood
 668 map, describing a 1σ containment region. The ellipse is parameterized by three variables,
 669 σ_1 , σ_2 , and α , describing the scales of the two axes of the ellipse and its orientation. An
 670 average circularized error can be computed as (eq. 3.10)[?]:

$$\sigma_{evt} = \sqrt{\frac{\sigma_1^2 + \sigma_2^2}{2}} \quad (3.10)$$

671 This description can be further improved by comparing this error with the “true error”

672 obtained from examining the difference between the simulated event direction and the cor-
 673 responding reconstructed direction. By multiplying the above circularized error by the ratio
 674 of the reconstructed error to the “true” error, we remove potential bias due to effects not ac-
 675 counted for by the directional reconstruction algorithm. For example, one such effect would
 676 be the angle between the incident neutrino and the outgoing muon. Since the reconstruc-
 677 tion algorithm only reconstructs the direction of the track associated with the muon, the
 678 direction of the neutrino is still technically unknown. While at high energies the muon and
 679 its parent neutrino can be assumed to be colinear, this angle becomes a significant source
 680 of uncertainty below 1 TeV.

681 3.6 Energy Reconstruction

682 While the direction of track event in IceCube can be reconstructed with good precision
 683 using the methods described previously, reconstructing the energy is more difficult. The
 684 primary reason for this is simply a lack of information: since many tracks originate from
 685 events neutrino interactions outside of the instrumented volume, the entirety of the muon
 686 track is not contained within the detector. This prevents the detector from behaving as
 687 a calorimeter, and estimates must be made to extrapolate the initial event energy based
 688 on the portion of the track observed. Similar to the directional reconstruction, an energy
 689 reconstruction of a particular event can be obtained using a likelihood based approach based
 690 on the individual DOM observations.

691 At its core, this likelihood approach assumes that the number of detected photoelectrons
 692 (k) is expected to be poisson distributed with a mean directly proportional to the energy:
 693 $\lambda = E\Lambda$ (eq. 3.11), where Λ is the number of photons the event produces per unit energy:

$$\mathcal{L} = \frac{(E\Lambda)^k}{k!} e^{-E\Lambda} \quad (3.11)$$

694 Maximizing this likelihood over all j DOMs that see photoelectrons results in the relation
 695 (eq. 3.12):

$$E = \sum k_j / \sum \Lambda_j \quad (3.12)$$

696 Which is largely a statement that the event energy is proportional to the number of
 697 observed photons, scaled by some factor that is the sum of the light yield scaling functions
 698 Λ_j . These functions depend on a variety of factors including the geometry and ice optical
 699 properties. Much like in the case of the directional reconstruction, these functions are often
 700 obtained from tabulated monte carlo data, smoothed with a multi-dimensional spline.

701 This likelihood can then be applied to calculate the energy loss rate ($\langle dE/dx \rangle$) of a
 702 particular muon. Above 1 TeV, this energy loss rate is roughly proportional to the muon
 703 energy. A robust estimate of this rate can be obtained by fitting segmented energy losses
 704 along the muon track using the methodology described in [?]. Once a list of segmented energy
 705 losses is calculated, there are several different approaches to converting to a reconstructed
 706 energy.

- 707 • **MuEX** takes the average of the segmented energy losses and uses that as an estimate
 708 of the energy
- 709 • **TruncatedEnergy** first removes the largest 40% of energy losses before calculating
 710 an average, ideally reducing the variance in the calculation of $\langle dE/dx \rangle$.

711 A comparison of these approaches can be found in [?], and both methods provide approx-
 712 imately 35% precision in $\log_{10} E$ for an initial muon energy of 10^4 GeV, improving slightly
 713 to approximately 30% in $\log_{10} E$ at higher energies.

714 3.7 IceCube Event Samples Overview

715 As the Icecube detector is capable of doing a wide variety of science, there exists a plethora
 716 of event samples used within the collaboration. Even within the context of searches for point
 717 sources of astrophysical neutrinos, there exist several event samples of IceCube events, each

718 with their own selection criterion and set of reconstructed parameters. In many cases, the
 719 distinguishing features between event selections used in point source analyses are purity and
 720 event rate. An ideal point source event sample would have both a high purity of astrophysical
 721 events in addition to a high event rate. Unfortunately, this is not possible with the current
 722 iteration of the IceCube data, as we observe relatively few events above 100 TeV (where
 723 the highest purity of astrophysical events can be achieved), and below 100 TeV there is a
 724 significant irreducible background of atmospheric neutrinos.

725 For this reason, point source event samples in the IceCube collaboration generally fol-
 726 low two different philosophies. “Low statistics/high purity” samples contain relatively few
 727 events, but the events in these samples have a high probability of being astrophysical in
 728 origin [?] [?]. By contrast “high statistics/low purity” samples contain a higher number of
 729 events, including additional astrophysical events. However in doing so, these samples also
 730 include significantly more atmospheric (background) events [?] [4]. In the context of point
 731 source searches, these samples typically rely on advanced statistical methods in their analy-
 732 sis pipeline to distinguish between clustered astrophysical signal and isotropic atmospheric
 733 background.

734 Even within the category of high statistics/low purity samples used for neutrino source
 735 searches, there exist multiple samples that are regularly used within the IceCube collabora-
 736 tion. The following sections will briefly outline three such samples that are relevant to the
 737 analyses presented later in this work. A comparison of the three samples outlined here can
 738 be seen in table 3.1 and figure 3.9

739 **3.7.1 PointSourceTracks v002p03**

740 Starting with Muon level 3 data, this sample applies an additional BDT to attempt to select
 741 for well-reconstructed muon neutrino interactions from mis-reconstructed atmospheric muon
 742 background. The variables used in this BDT were associated with a track-like event topology,
 743 and the BDT was trained using both background data, as well as simulation of both an $E^{-2.0}$

744 and $E^{-2.7}$ signal. The result is a high-statistics sample of mostly track-like neutrino events
 745 in the northern sky, consisting of both atmospheric and astrophysical neutrinos [?]. Events
 746 in this sample use a SplineMPE reconstruction (“plain” settings, corresponding to a balance
 747 of computation time and precision) for the event direction, and a MuEX reconstruction for
 748 the event energy.

749 This sample covers seven years of IceCube data (2008-2015), and was used for the histor-
 750 ical untriggered flare analysis of TXS0506+056 [3], where a 3.5σ neutrino flare was identified
 751 in 2014.

752 3.7.2 PointSourceTracks v003p02

753 Though this sample is oftentimes treated as a “successor” to PointSourceTracks v002p03, it
 754 is in many ways a completely new event selection. This sample covers 10 years (2008-2018)
 755 of IceCube data. Like v002p03, this sample also starts with Muon level 3 data, however here
 756 the BDT is trained to additionally reject cascade-like events in addition to accepting track-
 757 like events. Additionally, an improved directional reconstruction is used: the SplineMPE
 758 reconstruction algorithm is applied twice, with the second application using the results of the
 759 first as a seed, and additionally including the energy estimation. This results in improved
 760 angular resolution [?].

761 This sample additionally requires that events pass some precuts prior the the application
 762 of the BDT. Events are only selected if they satisfy the conditions below:

- 763 • The length of empty track (the portion of the reconstructed track that does not have
 764 any associated DOM hits) must be $\leq 400\text{m}$
- 765 • The reconstructed track length must be at least 200m
- 766 • The number of hit DOMs must be ≥ 12
- 767 • The number of DOMs that observe direct (non-scattered) photons must be ≥ 6

- 768 • $\cos(\theta_{geo}^2) < 0.2$, where θ_{geo} is the angle between independent reconstructions calculated
 769 for the first and second half of the track only. For a high quality track, both the first
 770 half reconstruction and the second half reconstruction should lie almost parallel.

771 This sample also has different requirements for events observed from the southern sky.

772 The minimum track length and maximum empty track length pre-cuts are applied as in
 773 the northern sky, in addition to an additional cut that the initial estimated uncertainty
 774 ($\sigma_{paraboloid}$) must be less than 5 degrees. A cut on the likelihood reconstructions is also
 775 enforced, requiring $R \log(\mathcal{L}) > 9$, where $R \log(\mathcal{L})$ is the “reduced log likelihood”, where the
 776 maximum likelihood value, \mathcal{L} is divided by the number of degrees of freedom, n_{dof} ($n_{dof} = 5$
 777 in this particular case). Events in the southern sky are also required to have hits on more
 778 than 5 different IceCube strings if the number of direct DOM hits was fewer than 12 [?].

779 This sample is notable as it was the sample used for the 10-year all-sky IceCube time
 780 integrated analysis, where NGC 1068 was identified as having a significance of 3σ [4]. This
 781 sample has also been publicly released for use outside the IceCube collaboration [?].

782 3.7.3 NorthernTracks v002p06

783 The NorthernTracks sample is a high statistics, low purity sample of through-going tracks
 784 that was originally developed for the purpose of performing a diffuse fit of the atmospheric
 785 and astrophysical neutrino spectrum. As such, this sample has relatively good data/MC
 786 agreement (as this is essential to the diffuse fit analysis pipeline), but is restricted to only
 787 events in the northern sky. Additionally, this sample does not make use of data from
 788 DeepCore DOMs, a decision that was made in order to homogenize the detector. This
 789 sample covers 8 years of livetime (2009-2017) has been used for point source analyses as well
 790 as diffuse studies of the neutrino spectrum [?].

791 The precuts for this sample in the northern sky are identical to PointSourceTracks
 792 v003p02, however this selection then uses two separate BDTs to further filter events: one
 793 BDT to select for track-like events, and a separate BDT to reject cascade-like events. In

794 practice the application of these two BDTs is similar, but not perfectly identical, to the
795 application of the single BDT in PointSourceTracks v003p02. Also of note is that the BDTs
796 used in the NorthernTracks selection are trained exclusively using simulation, for both signal
797 and background.

798 This sample uses a SplineMPE directional reconstruction (with “max” settings, priori-
799 tizing precision over computation speed), and a TruncatedEnergy estimator as the energy
800 reconstruction.

| | PSTracks v2 | PSTracks v3 | NorthernTracks |
|--------------------------|---------------------------------|-------------------------------------|--------------------------------|
| Pre-cuts | No | Yes | Yes |
| BDT 1 | Selects tracks | Selects tracks and rejects cascades | Selects tracks |
| BDT 2 | None | None | Rejects cascades |
| Signal training set | Simulation | Simulation | Simulation |
| Background training set | Data | Data | Simulation |
| Direction reconstruction | SplineMPE (“plain”) | SplineMPE (“plain”) $\times 2$ | SplineMPE (“max”) |
| Angular error estimator | Paraboloid | Paraboloid | Paraboloid |
| Energy estimator | MuEX | MuEX | TruncatedEnergy |
| DeepCore included? | Yes | Yes | No |
| Livetime | 7 years (2008-2015) | 10 years (2008-2018) | 8 years (2009-2017) |
| Declination Range | $-90^\circ < \delta < 90^\circ$ | $-90^\circ < \delta < 90^\circ$ | $-5^\circ < \delta < 90^\circ$ |
| Events | 711,878 | 1,134,451 | 493,252 |

Table 3.1: A comparison of several similar high statistics/low purity event samples used by the IceCube collaboration

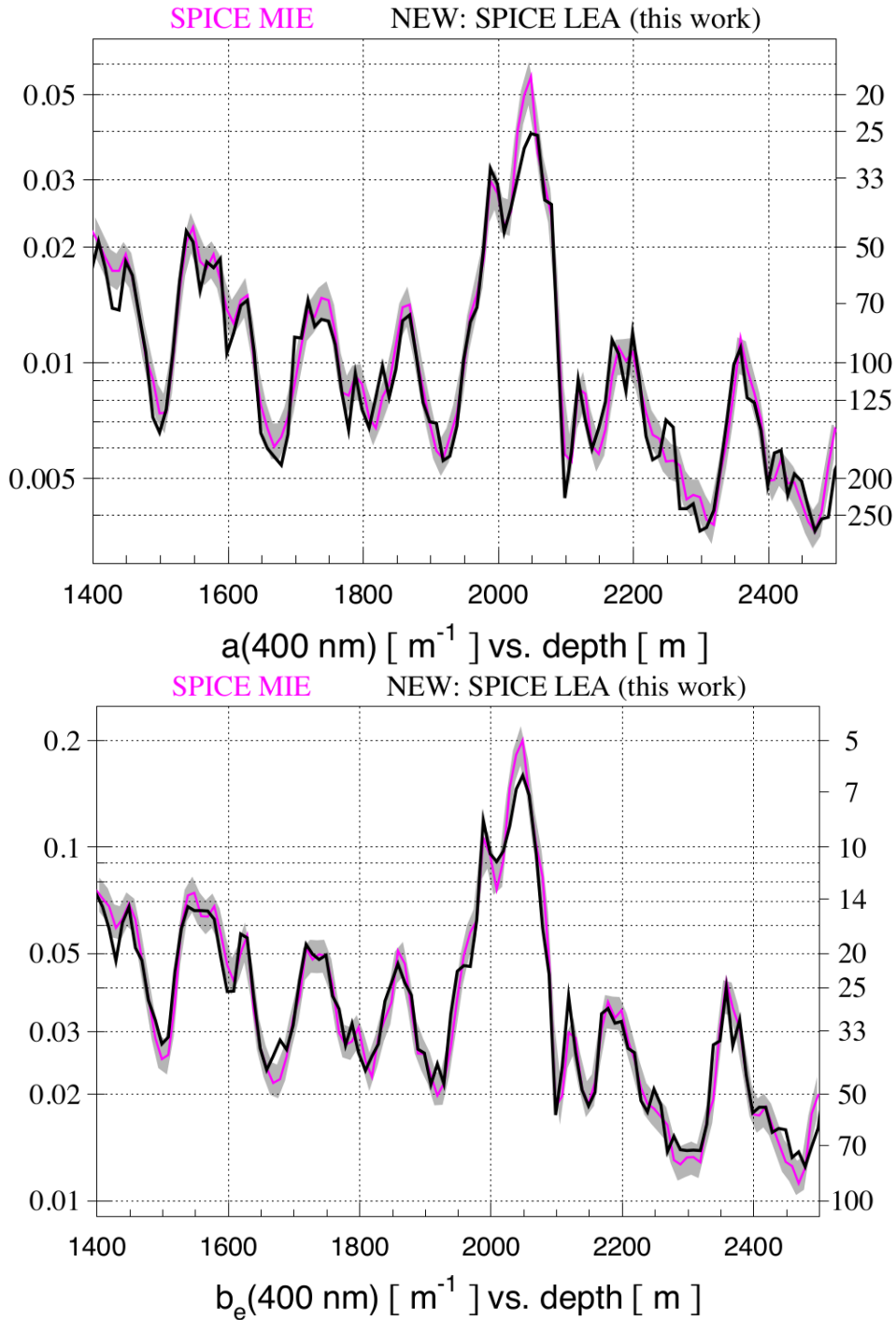


Figure 3.5: Plots of the absorption (top) and scattering (bottom) of 400 nm light as a function of depth in the south pole ice. The peak near a depth of 2000 meters is referred to as “the dust layer”, and is thought to correspond to a layer of dust deposited at the south pole at some point in the Earth’s history. “SPICE MIE” and “SPICE LEA” refer to two different ice models describing the detector ice, with the more recent model (SPICE LEA) incorporating the bulk ice anisotropy [?]

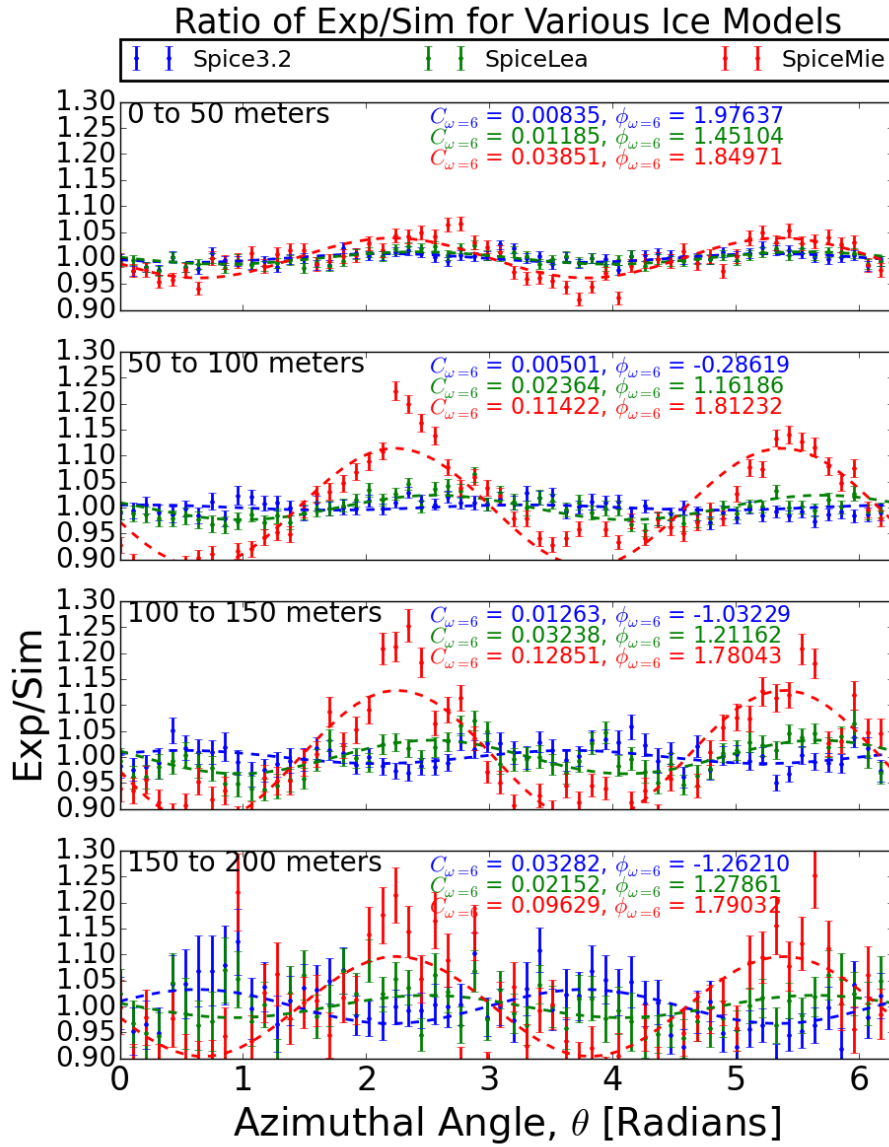


Figure 3.6: Plots of the ratio of light seen from atmospheric muons in experiment and simulation using various ice models (SpiceMie, SpiceLea, and Spice3.2), as a function of azimuthal angle between the muon track and the observing DOM. SpiceMie does not account for the ice anisotropy, resulting in a sinusoidal shape that grows with distance. SpiceLea and Spice3.2 both account for the anisotropy, and consequently the sinusoidal shape is reduced in amplitude when using these ice models.

IceCube Event Types

Early → Late

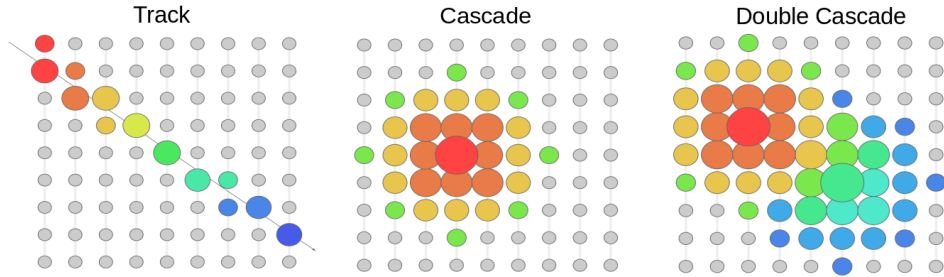



Figure 3.7: Cartoons in the x/z plane depicting the various event types seen by the IceCube detector. Grey circles are intended to represent individual DOMs, while colored circles correspond to DOMs that saw photoelectrons. The size of the circle corresponds to the amount of charge seen, while the color denotes the timing. Of most relevance to this work are tracks (left), as their long lever arm provides good pointing resolution.

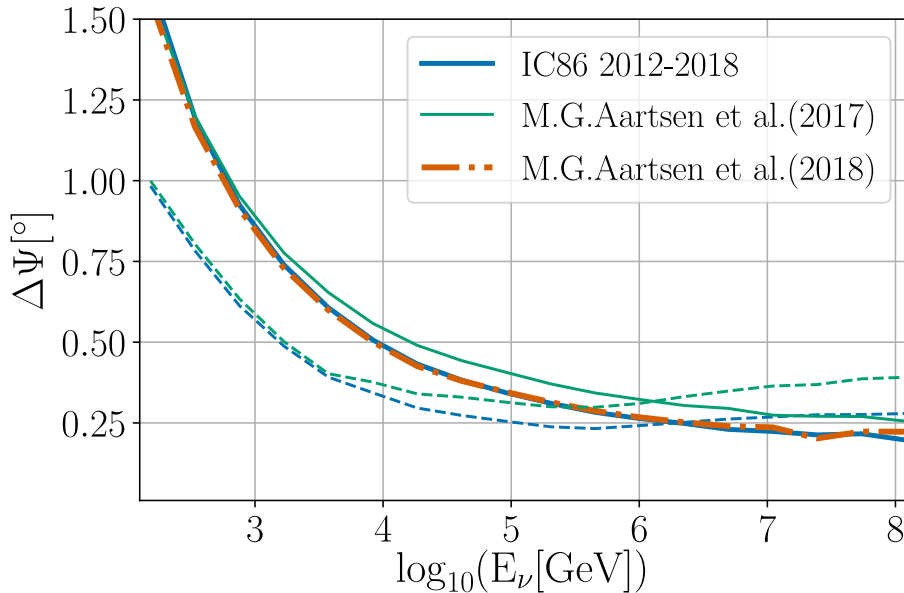


Figure 3.8: The median angle between simulated neutrino and reconstructed muon directions as a function of energy for various high-statistics IceCube samples composed of track events. The dark blue line corresponds to PSTracks v003p02, the light blue line corresponds to PSTracks v002p03, and the orange dashed line corresponds to NorthernTracks v002p06 (see section 1.7 for a description of these data samples). The solid lines describe events in the northern hemisphere, while the dashed lines are events in the southern hemisphere [4][?][?].

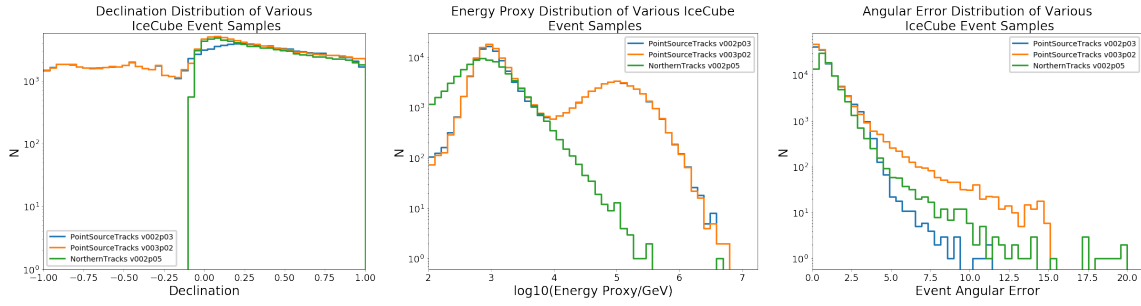


Figure 3.9: Distributions of the event variables in the three samples discussed in this section. The NorthernTracks sample does not contain events in the southern sky, as can be seen in the declination distribution on the left. This additionally has the effect of altering the overall energy proxy distribution for the sample, as the higher-energy peak in the energy proxy distribution for the PointSourceTracks samples is composed primarily of high energy southern sky events.

801 **Chapter 4**

802 **Review and Improvements to**
803 **Statistical Methods in Neutrino**
804 **Astronomy**

805 Point source searches in neutrino astronomy are essentially weighted clustering analyses:
806 each event is determined by a set of coordinates (right ascension, declination, angular error,
807 and time), and a weight (energy), and the task is to determine if high weight points are
808 clumped beyond what is expected purely from statistical fluctuations. Most attempts to
809 do this make use of a similar approach, using data-driven background estimation and a
810 likelihood-based estimator of clustering. This section outlines the general framework of such
811 an analysis, as well as several variants of the likelihood-based clustering estimator that is
812 commonly used. In the simplest case, only spatial clustering is examined, and temporal
813 information is excluded entirely (“time-integrated” analyses), however it can be additionally
814 interesting to explore the possibility of temporal clustering of events as well, increasing the
815 dimensionality of the clustering problem by one. Later in this section we introduce an
816 improved method for fitting ensembles of spatial and temporal clusters of events (“flares”)
817 to characterize the data, which is an improvement over existing methods which only make
818 use of information from the most significant flare. This fills in the methodological gap that

819 can be seen in table 1.1.

820 4.1 Clustering Analysis Outline for an Arbitrary Test 821 Statistic

822 There are many ways of constructing a test statistic in neutrino astronomy, in addition to
823 a variety of types of clustering to look for (for example, clustering near various source cata-
824 logs, clustering in space and time, clustering with weights according to source/event energy
825 weights, clustering about an extended spatial feature such as the galactic plane). However,
826 almost all clustering analyses in this area share several features in their construction:

- 827 1. A test statistic is formulated, which ideally tests the degree of clustering of astrophys-
828 ical events near a particular source candidate location. This test statistic is typically
829 a likelihood-based test statistic of a form similar to that which is described in the
830 following section, however this test statistic is often modified to reflect the specifics of
831 the clustering hypothesis being tested.
- 832 2. A background test statistic distribution is calculated using maps generated from data
833 that has the right ascension values of events randomized. This destroys any cluster-
834 ing that may have already been present, providing an excellent representation of the
835 null hypothesis (a purely diffuse astrophysical neutrino flux with no spatial or tem-
836 poral clustering). As this background estimation is data-driven, it is robust against
837 unknown backgrounds that may be present in the sample. Scrambling the data does
838 not affect the sample event content, and consequently the underlying distributions of
839 event declination, energy, and arrival time are unchanged.
- 840 3. Alternative hypothesis test statistic distributions may be obtained from simulations of
841 signal events. If the analysis is not sensitive to the total astrophysical neutrino flux,
842 simulated events can simply be added to the background maps generated above. If the

analysis is sensitive to the total astrophysical flux, then more sophisticated methods (such as moving existing events instead of injecting new events) may be required. Once maps containing signal have been generated, they can be used both to characterize the performance of the analysis, as well as compute upper limits as the median of the 90% upper limit on the flux in the event of a null result.

4. The performance of the test statistic being used is typically evaluated using the *sensitivity* and/or *discovery potential*. For the purposes of this work, the *sensitivity* refers to the amount of signal that needs to be injected before 90% of the test statistic distribution is greater than the median of the background test statistic distribution. Similarly the *discovery potential* refers to the amount of signal that needs to be injected before 50% of the test statistic distribution is greater than the $N\sigma$ significance threshold in the background test statistic distribution (N is typically either 3 or 5, but can be other values. This is typically clarified by stating that the value reported is the “N-sigma discovery potential”). “Amount of signal” is intentionally ambiguous here, as different analyses are sensitive to different types of signal. The sensitivity and discovery potential can be cast in terms of any number of variables that may be relevant to a particular analysis. For example, in the time-integrated case, these values are often reported as a flux, however time-dependent analyses may report a fluence, and analyses sensitive to source populations may even report their sensitivity as a curve in the space of source density and source luminosity.
5. The test statistic is calculated for the observed data sample, and this observed test statistic is compared to the distribution generated in step 2 to calculate a p-value. This p-value is then used to either accept/reject the null hypothesis of no clustering.

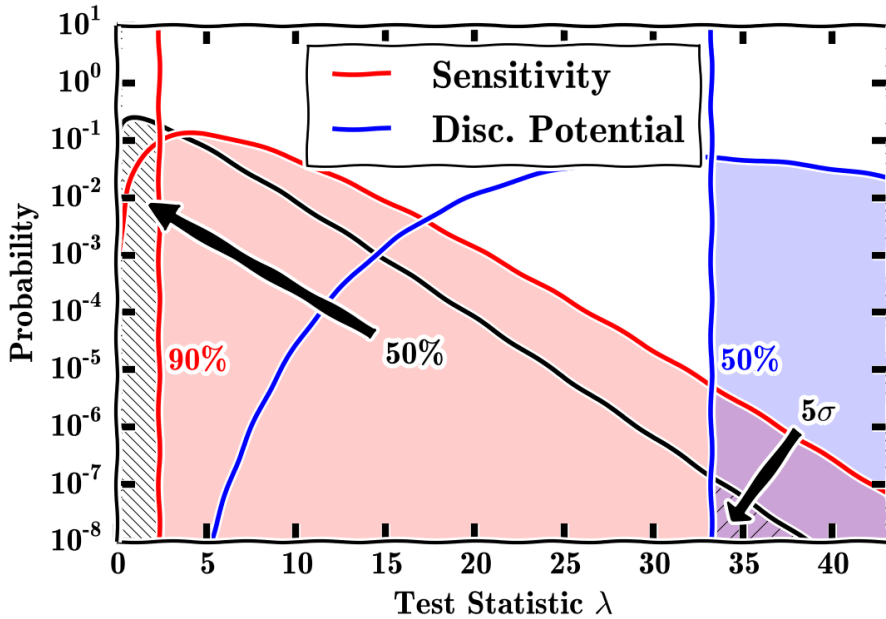


Figure 4.1: A toy plot showing the definitions of sensitivity and discovery potential. [?]

866 4.2 Unbinned Time Integrated Methods

867 Astrophysical point sources may be distinguished from the atmospheric neutrino background
 868 by way of clustering: if astrophysical sources are present in the data, events should be clus-
 869 tered near one another, while atmospheric events are expected to be isotropically distributed.
 870 Additionally, since high energy neutrino events are more likely to be astrophysical in origin,
 871 clustering of these events can be an even stronger indicator of the effect of neutrino point
 872 sources in the data. In short, we would like to construct a test statistic that reflects these
 873 observations. This can be done by way of a likelihood-based test statistic, using a likelihood
 874 composed of signal and background PDFs that describe the spatial and energy properties of
 875 events relative to a source candidate location. For a neutrino sample composed of N total
 876 events, the likelihood of the data for some number of signal (clustered astrophysical) events,
 877 n_s is (eq. 4.1)[?]:

$$\mathcal{L}(n_s, \gamma) = \prod_{i=1}^N \left[\frac{n_s}{N} S_i + \left(1 - \frac{n_s}{N}\right) B_i \right] \quad (4.1)$$

878 Where here, S_i and B_i are PDFs that describe the spatial and energy distributions

879 of signal and background events relative to the source candidate location. S_i and B_i are
 880 themselves composed of spatial and energy components (eq. 4.2 and 4.3).

$$S_i = R(r_i) \times \mathcal{E}(E_i, \delta_i | \gamma) \quad (4.2)$$

881

$$B_i = \frac{1}{\Omega} \times \mathcal{E}(E_i, \delta_i | Atm_\nu) \quad (4.3)$$

882 Note that the source spectral index, γ , enters as a free parameter in the energy portion
 883 of the signal PDF.

884 For the background PDF, the construction is relatively straightforward: background
 885 events originate from all directions equally, so the only effect that produces anisotropies is
 886 the detector acceptance. Since the IceCube detector acceptance does not vary as a function
 887 of right ascension, we can define B_i for a particular declination band to simply be $1/\Omega$,
 888 where Ω is the solid angle of a declination band centered on the source candidate declination.
 889 Similarly, the background energy PDF can be obtained by measuring the energy distribution
 890 of observed events as a function of declination. 2D histograms of event counts as a function
 891 of declination and event energy are assembled, and these distributions are then splined to
 892 create PDFs that can be used to evaluate B_i for events at an arbitrary declination and
 893 energy.

894 Unlike background events, signal events are expected to be clustered near the source
 895 candidate location. For this reason, the spatial component of the signal PDF, $R(r_i)$, is
 896 assumed to be a 2-D gaussian centered on the source candidate location (eq. 4.4):

$$R(r_i) = \frac{1}{2\pi\sigma_i^2} e^{-\frac{r_i^2}{2\sigma_i^2}} \quad (4.4)$$

897 Where r_i is the angular distance between the i th event and the source candidate location
 898 and σ_i is the event angular error.

899 The energy component of S_i is obtained from simulation: Simulated events are weighted
 900 according to a particular astrophysical spectral index, creating a 2D PDF describing the sum

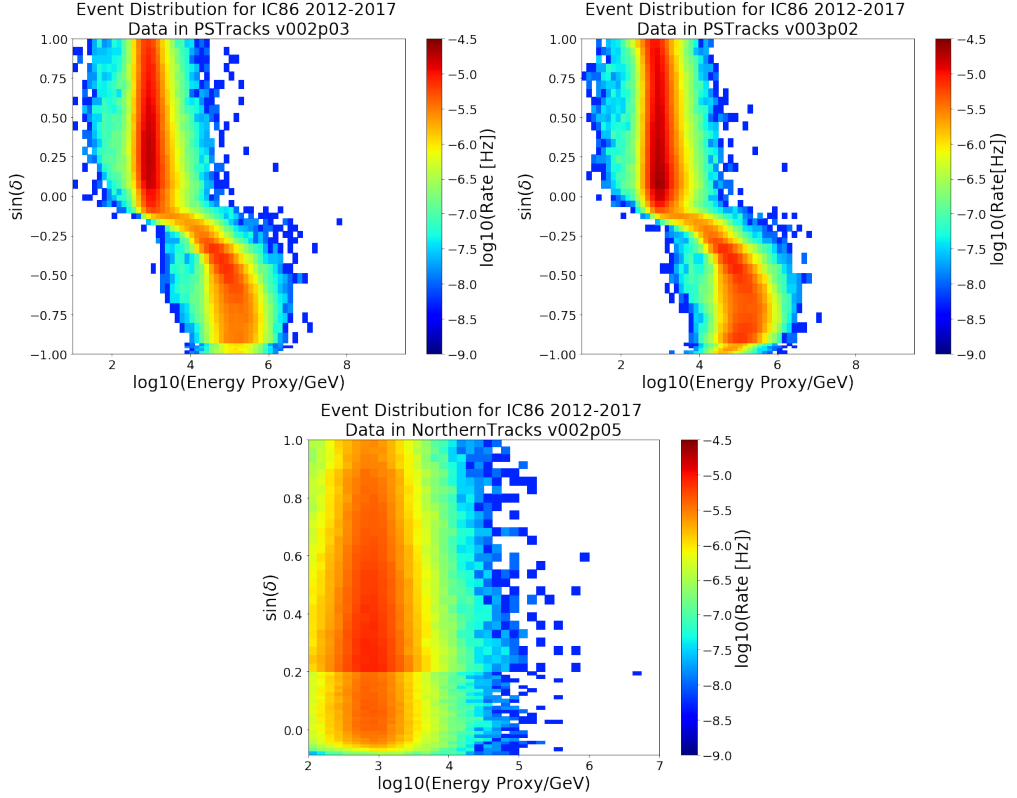


Figure 4.2: 2D histograms of declination and energy proxy for the 3 IceCube track event samples discussed in this document: PointSourceTracks v002p03 (left), PointSourceTracks v003p02 (right) and NorthernTracks v005p02 (bottom). Splines of these distributions are used as background PDFs in the clustering likelihood described in equation 4.1[?]. The NorthernTracks dataset is restricted to the northern sky, and additionally the splines associated with this dataset use finer binning near the horizon, hence the seeming discontinuity near $\sin(\delta) = 0.2$

901 of simulated event weights as a function of declination and energy. These maps are then
 902 divided by the background PDF described above to create a map describing the “signalness”
 903 of events at a particular energy and declination, given a spectral index. As these maps are
 904 created for a range of spectral index values (typically ranging between $\gamma = 1$ and $\gamma = 4$),
 905 a 3-D PDF of event energy, declination, and spectral index hypothesis results from this
 906 process. This is precisely the function $\mathcal{E}(E_i, \delta_i | \gamma)$ that enters the likelihood, and can be used
 907 to fit for γ , given events observed at declination δ with energy E_i .

908 The likelihood described in eq. 4.1 can be maximized as a function of s and γ , resulting
 909 in best fit parameters \hat{n}_s and $\hat{\gamma}$. We can then compute a test statistic for a given data sample
 910 from the likelihood ratio (4.5):

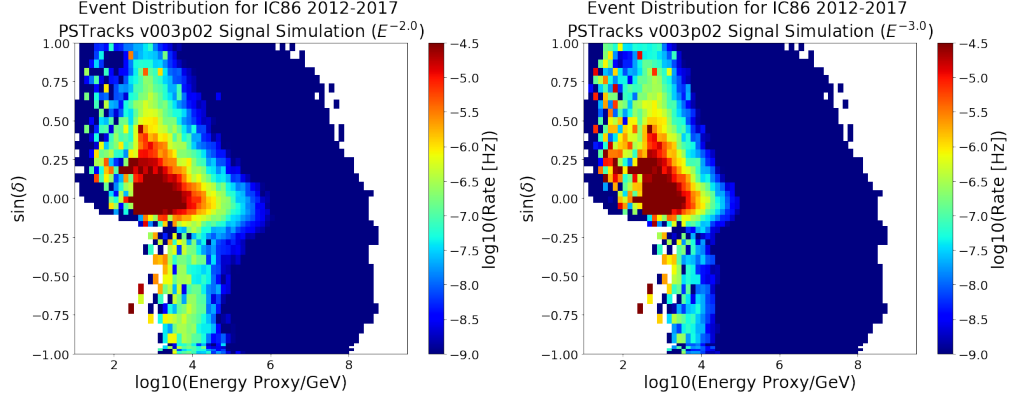


Figure 4.3: Distributions of simulated signal events in PointSourceTracks v003p02 for $E^{-2.0}$ (left) and $E^{-3.0}$ (right) spectra. The ratio of these distributions to the background expectation is then used to calculate the combined spatial and energy 2D PDF ratio ($S(r_i, E_i)/B(r_i, E_i)$) for a particular spectral index hypothesis. Similar distributions can be made for spectral indices ranging from $\gamma = 1.0$ to $\gamma = 4.0$, allowing for the signal spectral index to be fit by the likelihood.

$$TS = -2 \log \frac{\mathcal{L}(n_s = 0)}{\mathcal{L}(\hat{n}_s, \hat{\gamma})} \quad (4.5)$$

911 This test statistic can then be used in the generalized framework described in the sections
 912 above to test the hypothesis of spatial clustering of astrophysical neutrino events near a
 913 particular source location.

914 This framework can be applied to multiple locations at once, and the results combined by
 915 summing the individual test statistics calculated at each location (note that this is equivalent
 916 to calculating the product of the likelihoods). This process is often referred to as “source
 917 stacking”, and can be used to improve sensitivity to dim sources, provided there are multiple
 918 emitters in the source candidate list.

919 Other methods of combining information across multiple source locations exist as well. In
 920 particular, the binomial test is a popular way of doing this. Given a list of source candidates
 921 and their associated p-values, we can search for the most significant combination of source
 922 candidates by employing the binomial test-statistic (eq. 4.6)

$$p(k) = \sum_{i=k}^{N_{eff}} \binom{N_{eff}}{i} p_k^i (1-p_k)^{N_{eff}-i} \quad (4.6)$$

923 Where $p(k)$ is the p-value associated with combining the results of the k most significant
 924 sources, N_{eff} is the effective number of trials (often simply equal to the total number of
 925 source candidates), and p_k is the p-value of the k th most significant source. The minimum
 926 of $p(k)$ can then be computed and treated as a test statistic, to obtain a p-value associated
 927 with the best-fit number of sources (k_{min}) in a particular catalog.

928 4.3 Unbinned Time-Dependent Methods

929 In addition to being clustered in space, astrophysical neutrino events may also be clustered in
 930 time (a neutrino “flare”). Accounting for this temporal clustering may allow us to identify
 931 sources that are insignificant under a corresponding time integrated analysis. Studying
 932 the temporal variation of source candidates can also inform us of the specifics of the source
 933 dynamics of particle production, as the time scale of observed flares is related to the physical
 934 scale of the astrophysical objects in which particle production is occurring. This method
 935 was used in [3] to identify the 2014 neutrino flare candidate with a significance of 3.5σ .

936 4.3.1 Optimizing for a Single Flare

937 We can modify our time-integrated likelihood to account for potential temporal clustering
 938 as well by simply appending a temporal PDF to the existing PDFs that describe the spatial
 939 and energy components of the analysis (eq. 4.7, 4.8):

$$S_i = R(r_i) \times \mathcal{E}(E_i, \delta_i | \gamma) \times \mathcal{T}(t_i) \quad (4.7)$$

$$B_i = \frac{1}{\Omega} \times \mathcal{E}(E_i, \delta_i | Atm_\nu) \times \frac{1}{\Delta T} \quad (4.8)$$

940 Where ΔT is the full livetime of the sample, and the associated temporal background
 941 PDF is $1/\Delta T$, as the background event rate should be constant. In practice, this is assembled
 942 in a data-driven manner by measuring the data sample event rate in each of the 8-hour

943 segments ("runs") that are used to segment the data. In this way, seasonal variations of the
 944 detector event rate are accounted for by the likelihood, as the flare candidates are always
 945 being compared to the local event rate in time.

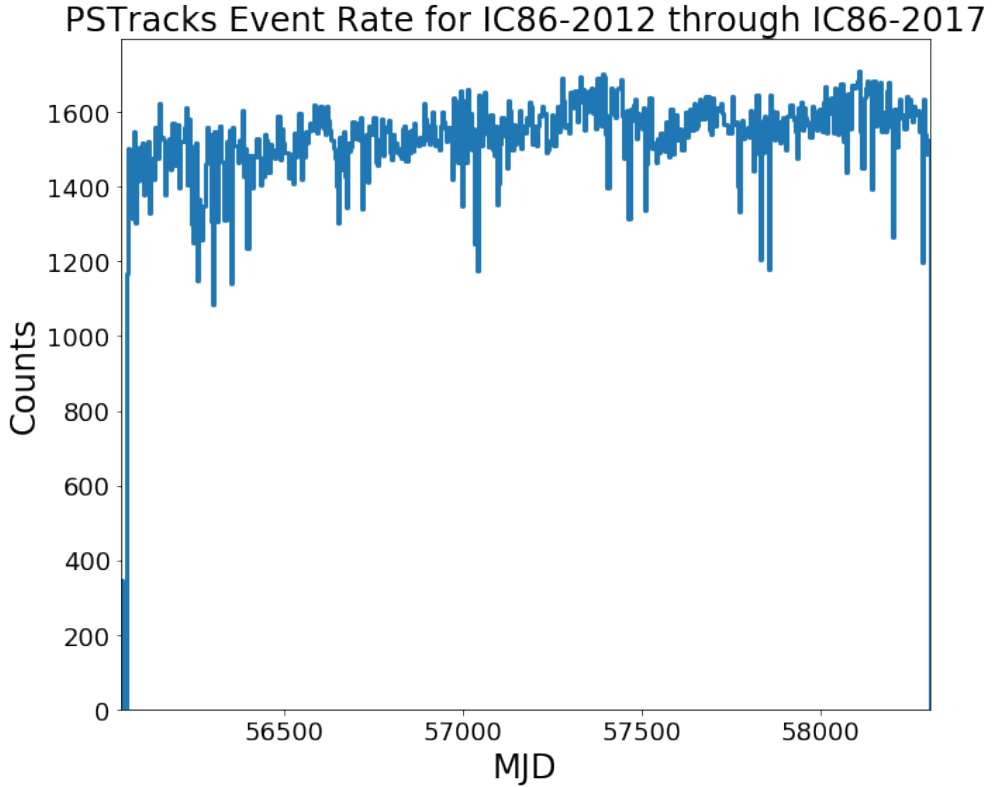


Figure 4.4: The event rate of the IC86 seasons of the PointSourceTracks v3 data sample. This event rate can be used to generate a background temporal PDF in the time-dependent clustering likelihood.

946 The temporal contribution to the signal PDF, $\mathcal{T}(t_i)$, can take various forms depending
 947 on the particular shape that one assumes for the time profile of flare candidates, but the
 948 most basic temporal profile that can be used is a box (eq. 4.9):

$$\mathcal{T}(t_i|t_0, \Delta t) = \begin{cases} 0 & t_i < t_0 \\ \frac{1}{\Delta t} & t_0 \leq t_i \leq t_0 + \Delta t \\ 0 & t_i > t_0 + \Delta t \end{cases} \quad (4.9)$$

949 This box-shaped temporal PDF essentially acts as a mask, filtering for events that occur
 950 within the time window between t_0 and $t_0 + \Delta t$. The events within this time window then

contribute to the likelihood in a similar manner to the time-integrated case. Note that by adding this temporal PDF to the likelihood, we have also introduced 2 new parameters that the likelihood can be maximized with respect to: t_0 and ΔT , which describe the flare start time and duration, respectively.

Similar to the time-integrated case, a likelihood ratio test statistic can be assembled from this likelihood, however this test statistic can be further improved in the time-dependent case by accounting for the duration of flare candidates that were scanned over (eq. 4.10):

$$TS = -2 \log \left[\frac{\Delta T}{\hat{\Delta t}} \frac{\mathcal{L}(n_s = 0)}{\mathcal{L}(\hat{n}_s, \hat{\gamma}, \hat{t}_0, \hat{\Delta t})} \right] \quad (4.10)$$

Where the factor $\frac{\Delta T}{\hat{\Delta t}}$ can be interpreted as a trial factor that accounts for the fact that there are significantly more short flare candidates that can be tested than long ones (e.g. there is only 1 potential flare candidate with $\Delta t = \Delta T$, but there are many flares that can be made with $\Delta t = \Delta T/100$). This factor normalizes the test statistic scale between short and long flares [?].

In practice, this process is extremely computationally intensive due to the number of likelihood minimizations that need to be performed. This can be mitigated by seeding flares with events that already have a high probability of being signal in origin, based off their energy and arrival direction. An ensemble of seed events can be defined to the set of events with S_i/B_i greater than some threshold value, where S_i and B_i refer to the signal and background PDF components of the time integrated likelihood (describing only the spatial and energy properties of contributing events). Typically this threshold is set to be relatively low ($S_i/B_i > 1$), however higher values can also be used if computational requirements are particularly stringent (e.g. if running over the entire sky).

Many analyses compute the test statistic in eq. 4.10 for a variety of flare candidates, and then use the flare with the maximum test statistic as the “best-fit” flare. The test statistic associated with this “best-fit” flare is then compared to a distribution of “best-fit” flares obtained from the background case (generated from data scrambled in right ascension),

resulting in a p-value that describes the strength of the clustering hypothesis relative the null hypothesis of no clustering.

In simulated signal trials, the likelihood-based flare test statistic is able to reconstruct the injected number of signal events in each flare with reasonable accuracy, and the per-flare spectral index fits show similar agreement as well.

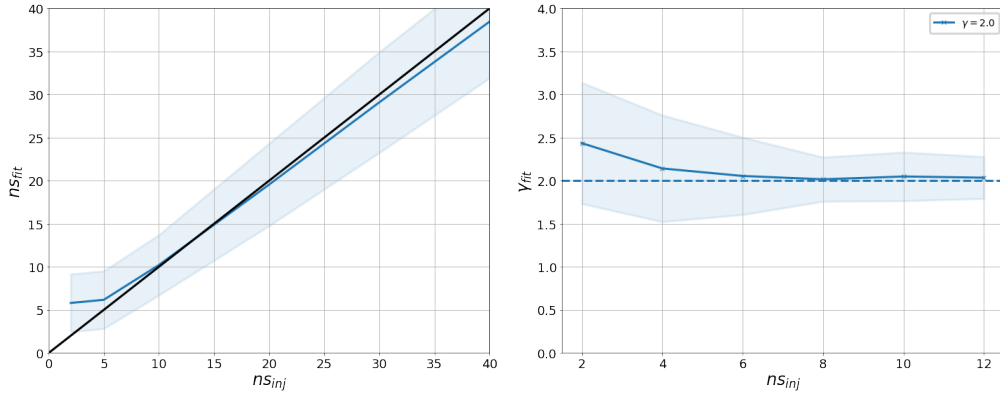


Figure 4.5: The best fit number of signal events in a flare, and the best fit spectral index versus the true number of signal events injected in simulated trials. On average, for flares with $>\approx 5$ events near the horizon ($\delta \approx 0^\circ$), the time-dependent likelihood is able to accurately estimate the true number of signal events.

4.3.2 Improving the Search for Temporal Clustering: Fitting Ensembles of Multiple Flares

As the IceCube detector collects more data, it becomes increasingly useful to be able to test the hypothesis of multiple neutrino flares that may have occurred at a particular location. Fitting only the largest flare is advantageous if the source flare rate is expected to be low enough that sources only flare once over the data-taking period, however if sources flare multiple times the single-flare analysis potentially misses a significant amount of useful information. By incorporating information from multiple flares at a particular location, an analysis can be sensitive to a smaller individual flare intensity. This is analogous to spatial stacking analyses, as can be seen in table 1.1, but we have additionally improved our algorithm to stack *flares* instead of just spatial source candidates. In this section we discuss

992 the construction of this method, and the following sections describe the results of the first
 993 applications of this method to various source catalogs.

994 The process of fitting multiple flares at a particular source candidate location is similar
 995 to the single-flare maximization procedure described above. Flare candidates are seeded by
 996 events with a high S_i/B_i ratio near the candidate location. For each flare candidate, the
 997 test statistic described in equation 4.10 is calculated. Unlike the single flare case, these
 998 flare candidates are then ordered by decreasing test statistic value, and any flares that
 999 overlap in time with a different flare that itself has a higher test statistic are removed.
 1000 Additionally, any flares with a test statistic < 0 are removed. What remains is a temporally
 1001 decorrelated ensemble of flare candidates, each with $TS > 0$. This ensemble functions as a
 1002 neutrino “flare curve” (similar to light curves produced by photon-based telescopes), that
 1003 describes the temporal variability of the signal originating from a source candidate location.
 1004 A “multi-flare” test statistic describing the significance of the temporal variability of this
 1005 source candidate can then be calculated as the sum of the individual flare candidate test
 1006 statistics (eq. 4.11):

$$\widetilde{TS} = \sum_{j=0}^{N_{flares}} TS_j \quad (4.11)$$

1007 Where here, j is an index that refers to the individual flares that compose the neutrino
 1008 flare curve. This test statistic can then be compared to an ensemble of similar test statis-
 1009 tics generated from right-ascension scrambled (background) data to obtain a final p-value
 1010 describing the significance of the set of flares that were fit at a particular source candidate
 1011 location.

1012 An estimation of the total number of signal events can be obtained in a similar manner
 1013 (eq. 4.12), where the total number of signal events associated with a particular source
 1014 candidate is just the sum of the best-fit number of n_s in each contributing flare candidate:

$$\widetilde{n}_s = \sum_{j=0}^{N_{flares}} \hat{n}_{sj} \quad (4.12)$$

1015 Note that this similar to time-integrated source stacking mentioned above, however in-
 1016 stead of stacking test statistics associated with spatially distinct locations, we are instead
 1017 stacking spatially and temporally distinct *flares*.

1018 The multi-flare algorithm is, in some sense, inclusive of the single flare algorithm: by
 1019 fitting all the flares at a source candidate location, we have obviously also fit for the largest
 1020 flare. It is thus trivial to obtain the single-flare significance once the multi-flare result is
 1021 obtained. In order to do this, simply compare the highest flare candidate test statistic that
 1022 was obtained with a distribution of single-flare test statistics obtained in a similar manner
 1023 from background (right-ascension scrambled) data.

1024 In addition to calculating the local significance of the largest flare, the local significance
 1025 of the other flare candidates composing the flare curve fit by the multi-flare algorithm can
 1026 also be obtained in a similar manner. We can define the “local significance” of a particular
 1027 flare (not necessarily the largest) to be the fraction of flares in the background distribution
 1028 with $TS_j > TS_{j,observed}$. Note however, that the calculation of multi-flare significance is done
 1029 in the space of TS_j , not the space of the corresponding local significances p_j . This means
 1030 that the multi-flare significance is *not* simply the product of the component flare p_j ’s, as each
 1031 flare is not entirely statistically independent from the others (e.g. once the largest flare is
 1032 fit, the remaining available livetime in which other flares can be fit is reduced by an amount
 1033 equal to the duration of the largest flare.)

1034 As mentioned above, the multi-flare algorithm is particularly useful in the case of several
 1035 similarly sized flares. In this case, while the single flare algorithms will identify the correct
 1036 number of events in the largest flare, the estimation of the total number of signal events
 1037 associated with the source candidate will be incorrect (as there is a non-negligible portion
 1038 of events that belong to flares that were not identified by the single flare algorithm). By
 1039 contrast, the multiflare algorithm improves the estimation of n_s in the case of multiple
 1040 similarly sized flares, as signal events in all flare candidates (not just the largest one) are
 1041 able to contribute. This improvement is shown in figure 4.7.

1042 As an example of a case where the multi-flare algorithm is advantageous, consider the

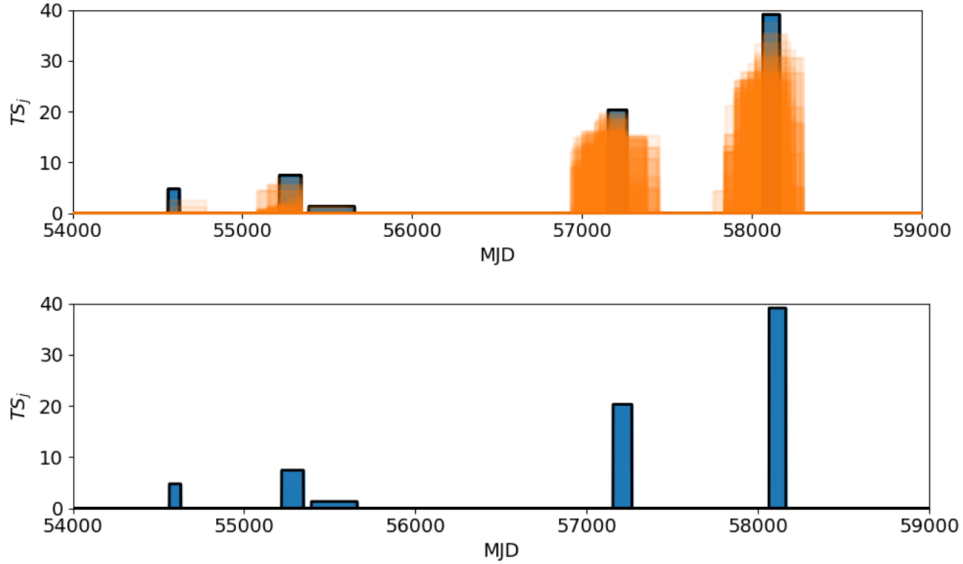


Figure 4.6: A graphical example of the progression of the multi-flare decorrelation algorithm. Colored boxes represent flare candidates that were tested, seeded by events with high S_i/B_i ratios. The height of each box corresponds to the individual flare candidate test statistic, TS_j . Orange flares overlap with another flare with a higher test statistic, and are consequently removed, leaving only the blue flares. The test statistics of the blue flares are then summed, and can be used for hypothesis testing of flaring neutrino emission at this source candidate location.

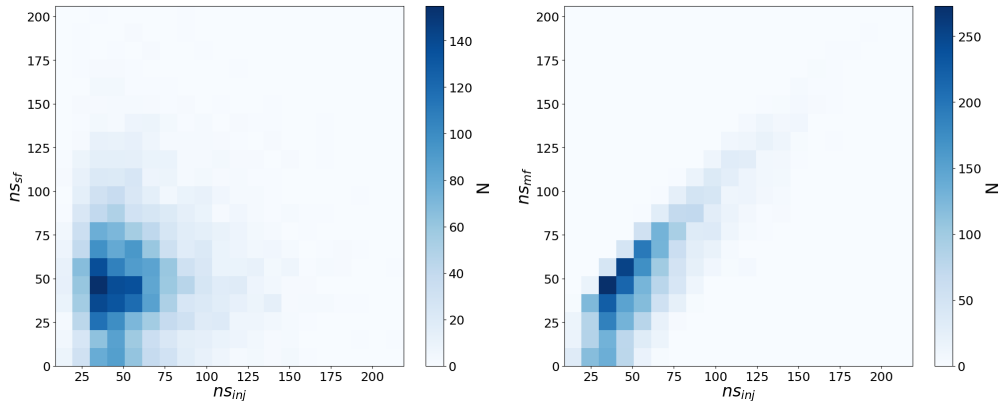


Figure 4.7: Left: the injected vs. fit number of signal events when attempting to use the single flare algorithm to describe an ensemble of neutrino flares. Right: The same plot, but using the multiflare estimation of n_s that accounts for signal events in all flare candidates.

1043 case shown in 4.8, which has 3 flares injected at MJD=55246.3, 55807.4, and 57632.7 at a test
 1044 location of (RA, Dec) = $(77.45^\circ, 5.61^\circ)$. The single flare method fits only the flare at MJD =
 1045 55246.3 (with $TS = 22.66$), while the multiflare method fits all flares together, with a multi-
 1046 flare test statistic of $\widetilde{TS} = 60.52$. While the largest individual flare only has a significance of

1047 3.29 σ , by combining information from all the flares that were fit at this location, we arrive at
 1048 a multi-flare significance of 4.7 σ . Note that because we have “stacked” our flare candidates
 1049 using their individual test-statistic (rather than their local p-value), there is no further trial
 1050 correction required unless one wishes to combine results across a catalog, in which case a
 1051 trial factor associated with the number of source candidate locations must be included.

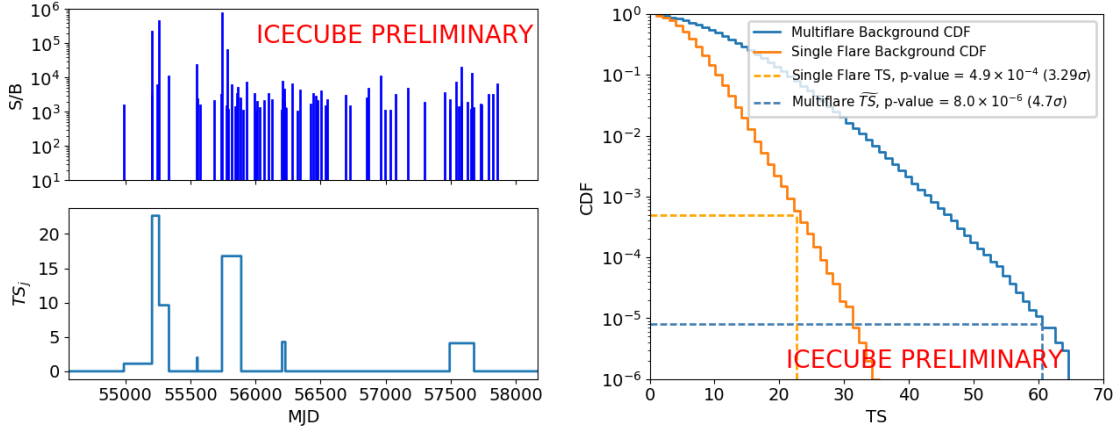


Figure 4.8: Left, top: Events that pass the S/B threshold cut for generating windows, for a source located at $(\text{ra}, \text{dec}) = (77.45^\circ, 5.61^\circ)$. There are 3 injected flares, centered at $\text{MJD}=55246.3$, 55807.4 , and 57632.7 . Left, bottom: The single flare method fits only the flare at $\text{MJD} = 55246.3$ (with $\text{TS} = 22.66$), while the multiflare method fits all flares together, with a global test statistic of $\bar{\text{TS}} = 60.52$. Right: The background test statistic distributions for a single source, located at $\text{declination} = 5.61^\circ$. The background multiflare test statistic distribution is shown in blue, while the single flare method is shown in orange. The vertical lines represent the test statistics associated with the flare curve on the left. The single flare p-value for this source is 4.9×10^{-4} (3.29σ), while the multiflare p-value is 8.0×10^{-6} (4.7σ).

1052 **Chapter 5**

1053 **Applications of the Multi-flare**

1054 **Algorithm to Source Catalogs**

1055 The multi-flare algorithm introduced in the previous section may be applied to an ensemble
1056 of sources that share common features. This is common practice in neutrino astronomy, as
1057 examining emission from a catalog allows us to explore the possibility of neutrino emission
1058 from a class of sources, rather than a specific individual source. Here, we explore two
1059 catalogs designed to explore source features related to those associated with the analysis of
1060 TXS 0506+056. Namely, the fact that the analysis was initially triggered by a high-energy
1061 neutrino event, and also the fact that TXS 0506+056 is a blazar. For the former, we assemble
1062 a catalog of high energy IceCube events to treat as “sources” (a “self-triggered” catalog
1063 analysis), while for the latter we use the pre-existing catalog of Fermi 3LAC blazars [?].

1064 In both cases, the multi-flare algorithm is applied at each source candidate location,
1065 resulting in a multi-flare test statistic (and corresponding pre-trial p-value) associated with
1066 each source candidate. To test for potential sub-populations of strong emitters within the
1067 catalog, we additionally calculate a best-fit number of multi-flare sources via iteratively
1068 summing the sources with the largest test statistics (5.1). For a given data set, the sources are
1069 ordered by their multiflare test statistic, \widetilde{TS} . A p-value for $k = 1, 2, 3, \dots N_{srcs}$ is calculated,
1070 and subsequently the k that produces the minimum p-value is selected (k_{best}).

$$\widetilde{TS}_{all} = \sum_{m=0}^{k_{best}} \widetilde{TS}_m \quad (5.1)$$

1071 An additional trial factor is then calculated by applying this procedure to maps of data
 1072 with randomized right ascension values to assemble a distribution of \widetilde{TS}_{all} representative of
 1073 the null hypothesis. A final p-value can then be obtained by comparing an observed \widetilde{TS}_{all}
 1074 with this null hypothesis distribution.

1075 For all the analyses detailed in this section, the NorthernTracks v002p05 sample was used.
 1076 This sample is described earlier in this document (section 2.5).

1077 5.1 Self-Triggered Catalog

1078 For this catalog, we select the locations of all the events in the NorthernTracks v002p05 data
 1079 sample that have a reconstructed energy proxy greater than 200 TeV. This energy threshold
 1080 is chosen as it is roughly the point where 50% or more of neutrino events are expected to
 1081 be astrophysical in origin. We can consequently expect that this catalog contains a non-
 1082 negligible number of astrophysical neutrino sources, and can test the hypothesis of additional
 1083 time dependent neutrino emission from these locations. Events that have been selected as
 1084 source candidates for the catalog are subsequently removed from the sample, and do not
 1085 otherwise contribute to the calculation of a multi-flare test statistic.

1086 This catalog contains 32 source candidates, all in the northern sky, and can be seen in
 1087 figure ???. Notably, this catalog does not include IC170922A (the alert event that triggered
 1088 the followup analysis on TXS 0506+056), as at the time this analysis was conducted, the
 1089 data sample does not extend past the 2015 season, and IC170922A occurred in the 2017
 1090 season.

1091 Applying the multi-flare algorithm described above to this catalog of the locations of
 1092 32 high energy neutrino events results in a best-fit number of sources of $k_{best} = 4$, with
 1093 an associated p-value of $p = 0.017$ (2.13σ), shown in figure 5.4. Detailed results for all 32

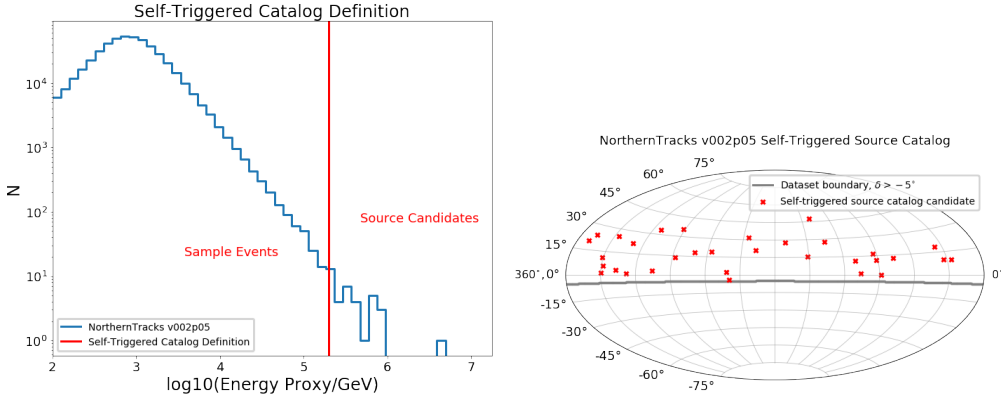


Figure 5.1: Left: The self-triggered catalog definition: Events with energy proxies to the right of the vertical red line (200 TeV) are treated as source candidates. Events to the left of the red line are then investigated for clustering around the locations of the source candidate events. Right: The self-triggered catalog assembled from the NorthernTracks v002p05 data sample, consisting of all events in the sample with reconstructed energy proxy greater than 200 TeV. The locations of these events are treated as source candidates for the purposes of applying the multi-flare algorithm, however the events themselves are removed from the sample prior to calculating a test statistic.

1094 source candidates, including fitted number of events and pre-trial p-values, can be viewed in
 1095 table 5.1.

1096 As mentioned in previous sections, a significant advantage of the multi-flare algorithm is
 1097 the generation of neutrino “light curves” (or “flare curves”) that show the historical activity
 1098 of a source candidate. The flare curves associated with the 4 most significant sources in the
 1099 self-triggered catalog can be seen in figure 5.3.

| RA | Dec | \hat{n}_s | p (pre-trial) |
|--------|-------|-------------|---------------|
| 36.69 | 18.32 | 47.21 | 0.00197 |
| 272.14 | 35.66 | 30.71 | 0.00729 |
| 170.19 | 27.85 | 45.75 | 0.00834 |
| 93.26 | 16.33 | 30.02 | 0.02667 |

Table 5.1: The top 4 most significant multi-flare source candidates in the self-triggered catalog composed of high energy IceCube neutrino events. Collectively, these sources form an excess with a significance of $p = 0.017$.

1100 Though not statistically significant, these results have several interesting features. Though
 1101 the high-energy “seed” events are removed prior to the calculation of a flare curve, 7 of the
 1102 flare curves generated include flares that would have included a high energy seed event.

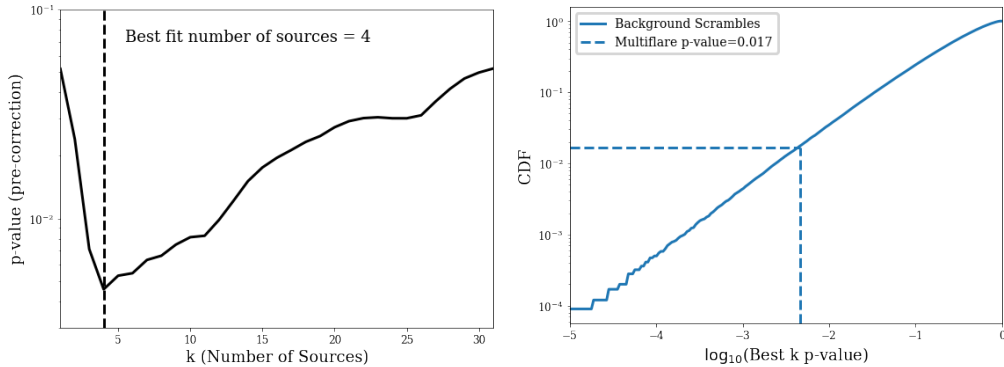


Figure 5.2: Left: The local significance of stacking the k highest test statistic sources, as a function of k . The best fit value of $k = 4$ can be seen as the minimum of this curve. Right: The trial corrected result for stacking the top 4 sources together, shown as a vertical line superimposed on the background distribution obtained by applying the algorithm to right-ascension scrambled data.

1103 Though not statistically significant, this is certainly above average, as only 11% of back-
 1104 ground trials have 7 or more flare curves with seed event/flare correlations.

1105 It is also potentially interesting to investigate the distributions of the parameters fit by
 1106 the multi-flare likelihood. By comparing the observed distributions with those expected from
 1107 background scrambles, we can check for inconsistencies of our data with the null hypothesis.

1108 5.2 Fermi 3LAC Blazars

1109 The 2014 TXS 0506+056 neutrino flare was notable not only for its association with a high
 1110 energy IceCube alert, but also for its spatial coincidence with the blazar TXS 0506+056. In
 1111 searching for additional neutrino sources, it is then not unreasonable to assemble a search
 1112 for neutrino flares associated with a large catalog of blazars. For this purpose, we use the
 1113 Fermi 3LAC catalog [?] to define a set of source candidates. Previous analyses searching
 1114 for spatial coincidence with earlier iterations of this catalog have been performed, but were
 1115 unable to identify any statistically significant excess [?]. Here, we instead specifically search
 1116 for transient emission using multi-flare algorithm described above.

1117 The Fermi 3LAC catalog is a catalog of AGNs detected by Fermi-LAT, consisting of
 1118 gamma ray sources in the third Fermi-LAT catalog (3FGL) [?] between 100 MeV and 300

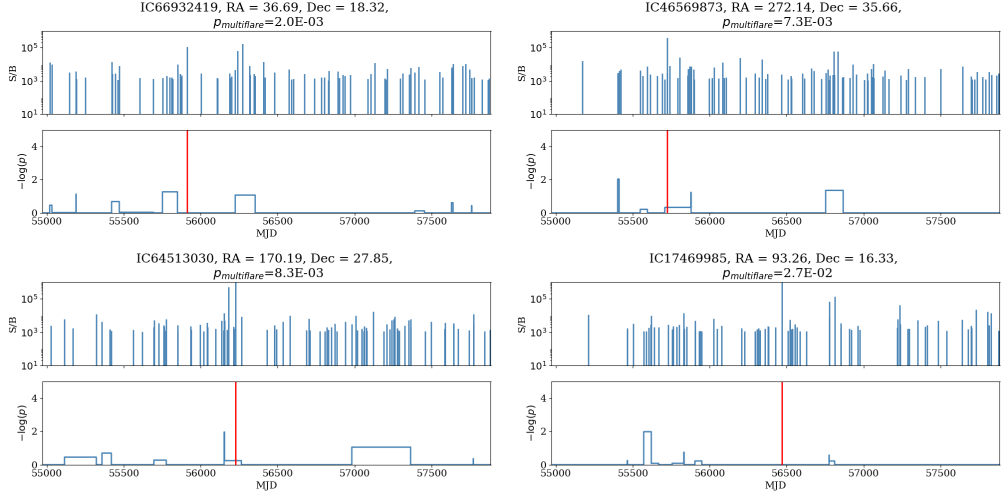


Figure 5.3: The neutrino “flare curves” associated with the 4 most significant multiflare source candidates in the self-triggered catalog. The top panel of each subplot shows the event weights, calculated by taking the ratio of the spatial and energy components of the signal and background PDFs described in equation 4.2 and 4.3, while the bottom panels show the fitted ensemble of decorrelated flares, with the local per-flare p-value plotted on the y-axis. The vertical red line denotes the arrival time of the high energy event used to define the source candidate location. This event is removed from the sample prior to applying the multiflare-algorithm, and consequently these events do not contribute to the flare curves shown in this figure.

1119 GeV with a Fermi test statistic greater than 25 between August 4, 2008, and July 31, 2012 [?].
 1120 The catalog contains 1591 objects, the majority (98%) of which are blazars, roughly evenly
 1121 split between FSRQs and BL Lacs. Notably, TXS 0506+056 is a member of this catalog.
 1122 In constructing this analysis, we select for blazars at declinations greater than -5° , as
 1123 the IceCube data sample (NorthernTracks v002p05) does not extend below this point. We
 1124 impose no further cuts, and all sources are weighted equally when calculating a multi-flare
 1125 test statistic. The equal weighting is chosen due to the unknown distribution of observed
 1126 neutrino flare intensities, which is a combination of the redshift distribution and the unknown
 1127 distribution of intrinsic neutrino flare intensities. Since this analysis seeks to be as model-
 1128 agnostic as possible, no additional weighting scheme is implemented. The final catalog to be
 1129 used for the multi-flare analysis consists of 1023 blazars, the locations of which are shown
 1130 in figure 5.6. This analysis is temporally untriggered, thus only the locations of the 3LAC
 1131 blazars are used; since the multi-flare algorithm fits for the neutrino flare candidate duration

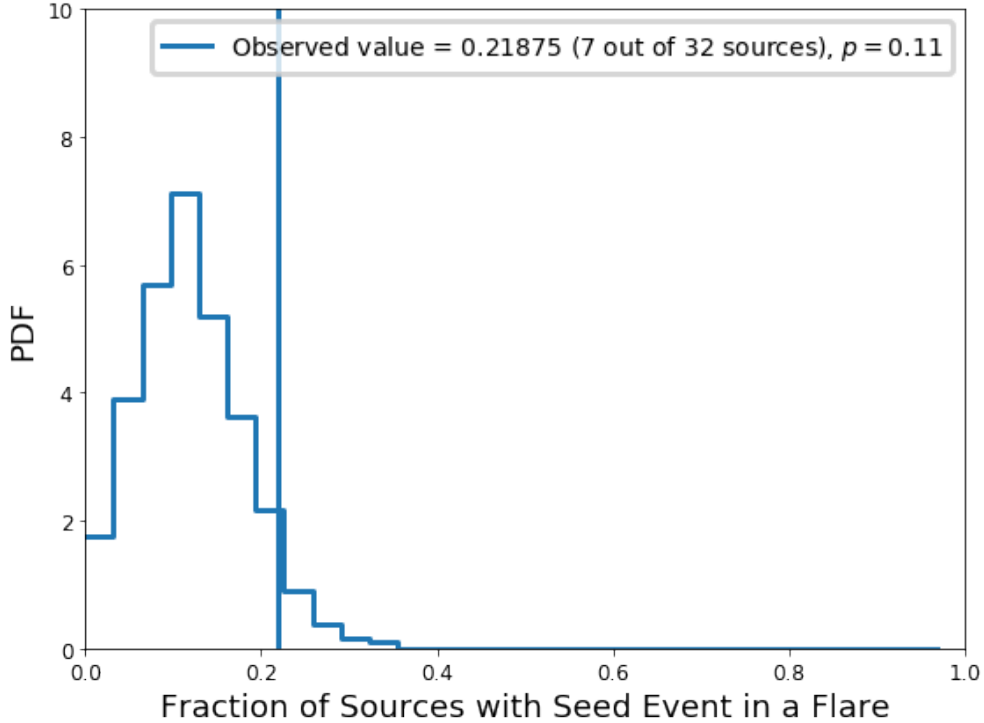


Figure 5.4: The distribution of number of flare curves that have a temporal correlation between the high energy seed event, and a fitted flare, obtained from sets of data where the right ascension of events has been randomized. The observed value (7 out of 32 sources, or 21.9%) is shown as a blue vertical line. 11% of trials have more than 7 correlations between seed events and fitted flares.

1132 purely from the neutrino data, no information from the gamma ray light curves for the source
 1133 candidates is incorporated into this analysis.

1134 The results of applying the multi-flare algorithm to this catalog of 3LAC blazars can be
 1135 summarized in figure 5.8. The optimization procedure for the most significant combination
 1136 of sources returned a best fit number of sources of $k = 125$, with an associated post-trial
 1137 p-value of $p = 0.06$. A list of these source candidates can be seen in table 5.2. As the
 1138 significance of this excess is consistent with the null hypothesis, we do not claim discovery
 1139 of neutrino flares associated with 3LAC blazars.

1140 Interestingly, despite the presence of the 2014 neutrino flare identified in [3], TXS 0506+056
 1141 is not the most significant source candidate, having a pre-trial p-value of only $p = 9.24 \times 10^{-3}$.
 1142 This is not unexpected, considering that there does not appear to much activity (in terms
 1143 of neutrino flares) at this location beyond the 2014 flare itself. As the multi-flare algorithm

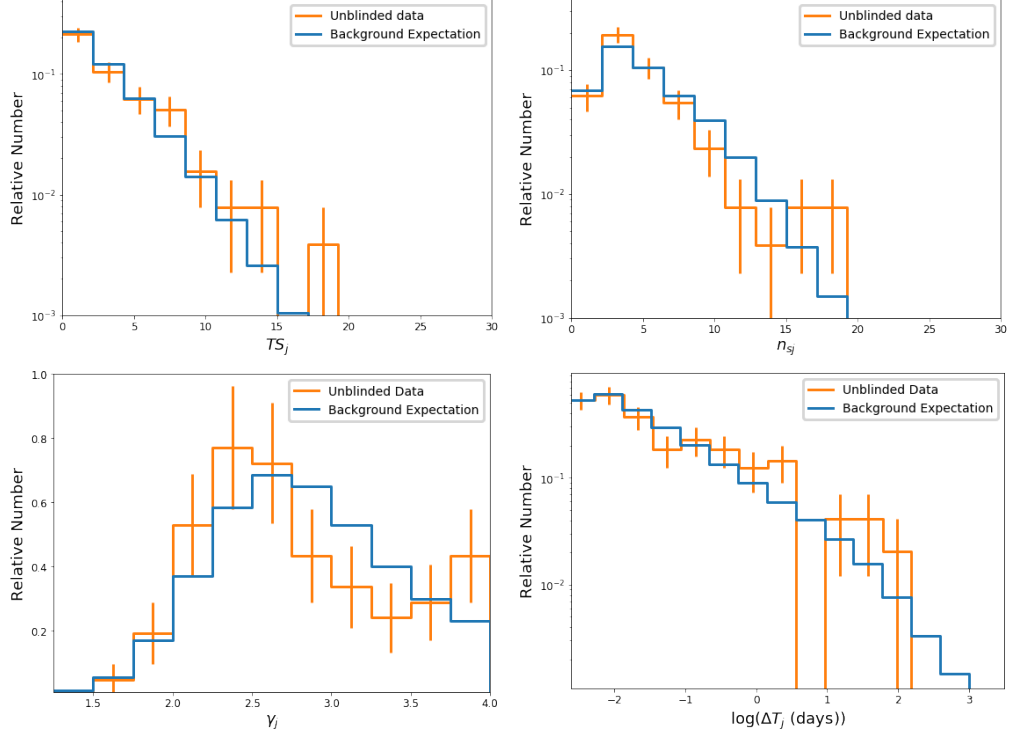


Figure 5.5: Distributions of fitted flare parameters for flares associated with the self-triggered catalog in both background scrambles (blue) and unblinded data (orange). While there is potentially some deformation in the distribution of fitted spectral indices (bottom left), a 2-sample K-S test comparing the observed and background distributions only returns a p-value of $p = 0.26$, indicating that the blue and the orange distributions are not significantly inconsistent with one another.

will return a high significance when there are multiple, moderately significant flares to stack together, it is unsurprising that there are other sources that have a higher multi-flare significance. As an example, the source candidate with the highest multi-flare significance is 1RXS J154604.6+081912. Rather than having a single large flare, the multi-flare algorithm fits multiple flares at this source candidate location, which combined have a significance of $p = 8.1 \times 10^{-5}$, despite none of the individual flares having a local significance much greater than $p = 0.01$.

Similar to the self-triggered catalog, we can additionally examine the distributions of the flare parameters that were fit for all the sources in the 3LAC catalog. No significant deviations from the background expectation are observed in any of the flare parameter distributions, as seen in figure 5.8.

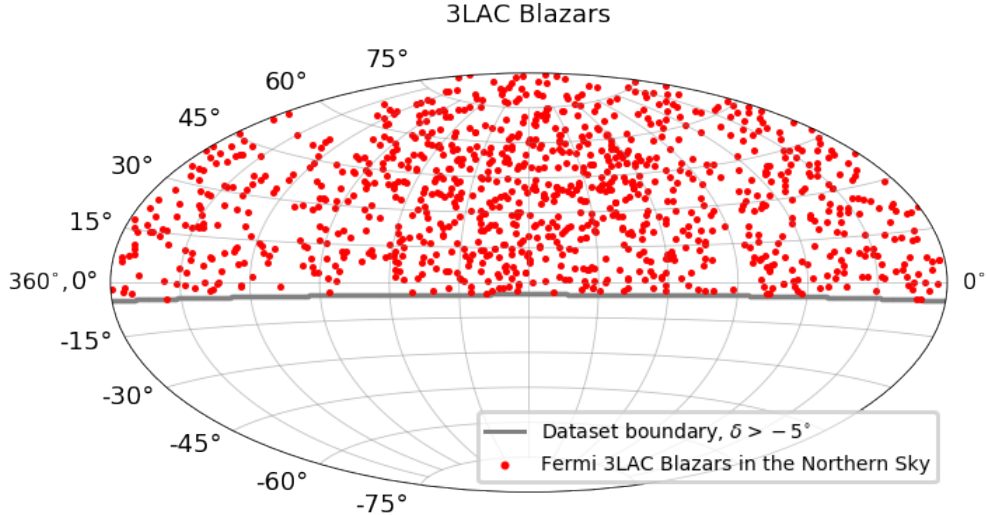


Figure 5.6: The locations of the 3LAC blazars that compose the catalog used for a multi-flare analysis. Blazars with $\delta < 5^\circ$ are not considered, as the IceCube NorthernTracks v002p05 data sample does not extend into this region. There are 1023 blazars that are considered as source candidates for the multi-flare analysis.

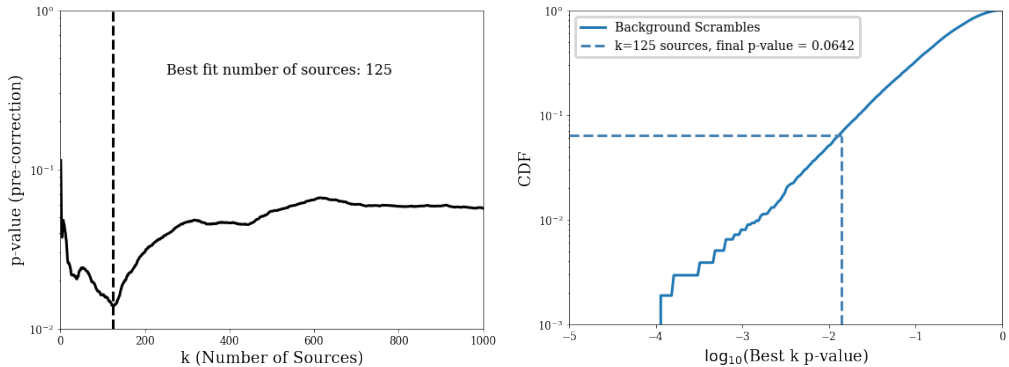


Figure 5.7: Left: The local significance of stacking the k highest test statistic sources in the 3LAC blazar catalog, as a function of k . The best fit value of $k = 125$ can be seen as the minimum of this curve. Right: The trial corrected result for stacking the top 125 sources together, shown compared to the background distribution obtained by applying the algorithm to right-ascension scrambled data. As the final p-value associated with the top 125 blazar sources is only $p = 0.06$, there was no significant excess of neutrino flares observed to be associated with 3LAC blazars.

1155 As with the self-triggered catalog, we also obtain neutrino flare curves describing the
 1156 historical variability of each source candidate. Figure 5.9 shows the flare curves of several
 1157 3LAC source candidates of note, including TXS 0506+056. While none of these sources are
 1158 significant enough to claim discovery, flare curves like the ones shown here are a potentially
 1159 valuable tool for multi-messenger analyses in the future that may seek to correlate neutrino

1160 emission with other astrophysical messengers.

1161 Though the application of the multi-flare algorithm to this catalog of 3LAC blazars did
 1162 not result in a significant detection, it does allow us to constrain the behavior of neutrino
 1163 flares associated with 3LAC blazars. Given that this method stacks flares together, the lack
 1164 of a significant results suggest that there is an upper limit to how bright and numerous
 1165 blazar neutrino flares may be. We express these limits in terms of the flare rate (how many
 1166 flares occurred over the lifetime of the data sample), and the per-flare E^2 flux. This allows
 1167 us to compare to previously calculated limits obtained from a time-integrated analysis [?].
 1168 These upper limits can be seen in figure 5.10

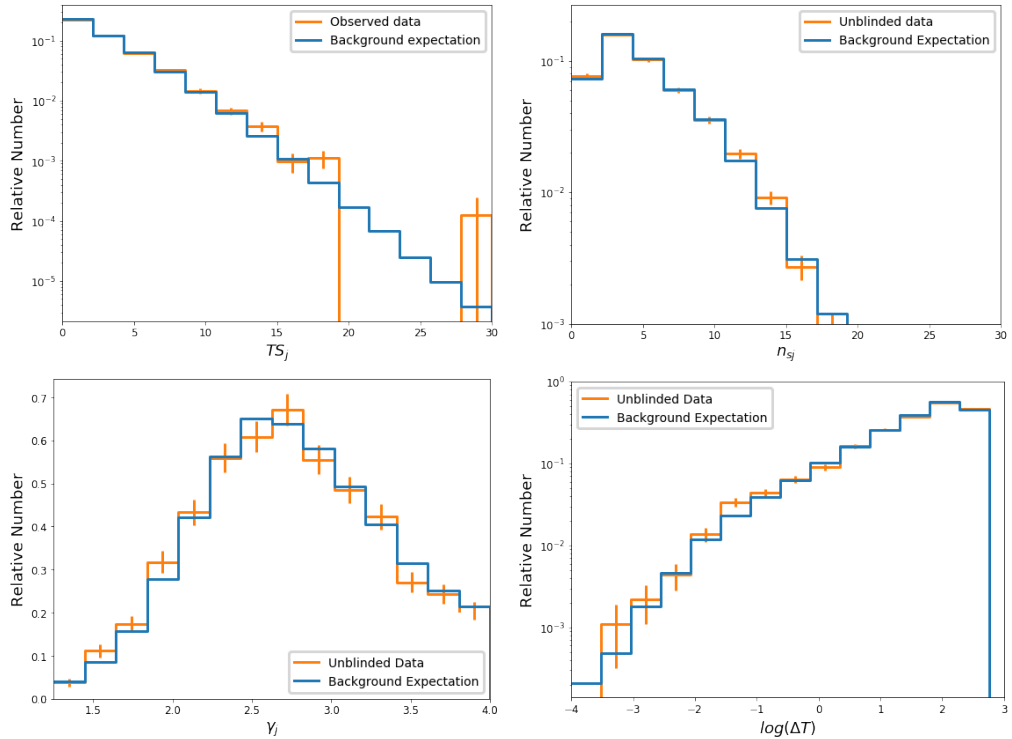


Figure 5.8: Distributions of fitted flare parameters for flares associated with the 3LAC blazar catalog in both background scrambles (blue) and unblinded data (orange). All distributions of fit parameters from observed data appear to be consistent with the background expectation. As this catalog includes TXS 0506+056, the 2014 neutrino flare originally discovered in the IC170922A follow-up analysis [3] is visible as the rightmost entry in the histogram of flare TS_j values in the plot in the upper left, having a value of $TS_j = 27.9$. There are no other flares that were fit in this catalog with $TS_j > 20$.

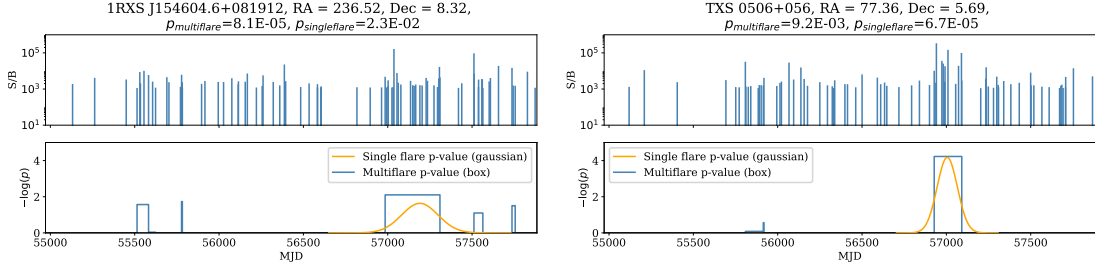


Figure 5.9: Neutrino flare curves for several sources of note in the multi-flare 3LAC blazar catalog analysis. The flare curves generated by the multi-flare algorithm are shown in blue, while the results of a corresponding single-flare analysis (that only fits the largest flare on each source) are shown in orange. Left: 1RXS J154604.6+081912, the most significant 3LAC blazar in the multi-flare analysis, having a pre-trial multi-flare p-value of $p = 8.11 \times 10^{-5}$. Note that for this particular source, the multi-flare significance driven by a set of five moderately significant flares, none of which are particularly significant on their own. The significance of this source in the single-flare analysis was only $p = 0.02$. Right: The flare curve for TXS 0506+056, showing the sizeable 2014 neutrino flare originally observed in [3]. The multi-flare p-value for TXS 0506+056 is only $p = 9.24 \times 10^{-3}$, as other than the 2014 neutrino flare, there are no other particularly significant neutrino flare candidates at this location.

Table 5.2: The top 125 multiflare source candidates in the 3LAC blazar catalog.

| Source Candidate Name | Source Class | RA (deg) | Dec (deg) | \hat{n}_s | p (pre-trial) |
|-----------------------|--------------|----------|-----------|-------------|-----------------|
| 1RXS J154604.6+081912 | bll | 236.52 | 8.32 | 53.49 | 8.11e-5 |
| RBS 1467 | bll | 227.18 | 27.15 | 55.11 | 3.05e-4 |
| GB6 J0723+2859 | fsrq | 110.98 | 28.99 | 40.48 | 4.58e-4 |
| RBS 1558 | bll | 241.59 | 56.51 | 28.88 | 1.92e-3 |
| PMN J2324+0801 | bll | 351.19 | 8.04 | 28.15 | 3.11e-3 |
| B2 2214+24B | bll | 334.25 | 24.36 | 36.90 | 3.79e-3 |
| GB6 J0850+4855 | bll | 132.50 | 48.92 | 38.18 | 4.75e-3 |
| 4C +20.25 | fsrq | 171.49 | 20.10 | 27.83 | 5.02e-3 |
| MG2 J094148+2728 | fsrq | 145.45 | 27.48 | 60.58 | 5.12e-3 |
| TXS 2241+406 | bll | 341.05 | 40.95 | 22.61 | 5.23e-3 |
| TXS 0213+619 | bcu III | 34.26 | 62.19 | 30.15 | 5.32e-3 |

Continued on next page

Table 5.2 – *Continued from previous page*

| Source Candidate | Source Class | RA (deg) | Dec (deg) | \hat{n}_s | p (pre-trial) |
|---------------------|--------------|----------|-----------|-------------|-----------------|
| GB6 J0100+0745 | bll | 15.09 | 7.76 | 37.33 | 6.45e-3 |
| RX J0850.5+3455 | bll | 132.65 | 34.92 | 20.42 | 7.16e-3 |
| B2 1436+37B | fsrq | 219.72 | 37.18 | 49.47 | 7.83e-3 |
| MG1 J165034+0824 | fsrq | 252.66 | 8.41 | 39.19 | 7.83e-3 |
| PKS 0256+075 | fsrq | 44.86 | 7.79 | 42.53 | 9.04e-3 |
| TXS 0506+056 | bll | 77.36 | 5.69 | 20.71 | 9.24e-3 |
| 1ES 1421+582 | bll | 215.66 | 58.03 | 28.49 | 0.0100 |
| TXS 0518+211 | bll | 80.44 | 21.21 | 48.49 | 0.0118 |
| W Comae | bll | 185.38 | 28.23 | 30.32 | 0.0123 |
| NVSS J141828+354250 | bcu II | 214.62 | 35.71 | 40.74 | 0.0128 |
| PKS 1532+01 | fsrq | 233.72 | 1.52 | 30.78 | 0.0131 |
| PKS 1424+240 | bll | 216.75 | 23.80 | 52.78 | 0.0148 |
| B3 2319+444 | fsrq | 350.58 | 44.76 | 41.93 | 0.0160 |
| PKS 0039+230 | fsrq | 10.52 | 23.33 | 48.89 | 0.0168 |
| B3 2238+410 | bll | 340.28 | 41.34 | 21.24 | 0.0175 |
| TXS 2315+189 | bcu II | 349.60 | 19.25 | 31.98 | 0.0197 |
| B3 2322+396 | bll | 351.32 | 39.96 | 30.07 | 0.0199 |
| NVSS J080637+774607 | bcu II | 121.66 | 77.77 | 52.32 | 0.0215 |
| MG1 J010908+1816 | bll | 17.28 | 18.27 | 26.59 | 0.0220 |
| 1H 0323+342 | nlsy1 | 51.17 | 34.18 | 10.09 | 0.0221 |
| NVSS J131921+775823 | bcu II | 199.84 | 77.97 | 16.99 | 0.0224 |
| RX J1351.3+1115 | bll | 207.84 | 11.25 | 27.93 | 0.0228 |
| RGB J1808+468 | bll | 272.00 | 46.83 | 29.19 | 0.0252 |
| RX J1149.5+2439 | bll | 177.38 | 24.66 | 33.52 | 0.0266 |
| TXS 2157+102 | bll | 330.03 | 10.50 | 47.04 | 0.0271 |

Continued on next page

Table 5.2 – *Continued from previous page*

| Source Candidate | Source Class | RA (deg) | Dec (deg) | \hat{n}_s | p (pre-trial) |
|-----------------------|--------------|----------|-----------|-------------|---------------|
| S5 1357+76 | fsrq | 209.48 | 76.72 | 35.44 | 0.0274 |
| S5 1803+784 | bll | 270.19 | 78.47 | 27.73 | 0.0287 |
| GB6 J1439+4958 | bll | 219.95 | 49.97 | 32.32 | 0.0291 |
| B2 2234+28A | bll | 339.09 | 28.48 | 25.36 | 0.0298 |
| GB6 J0929+5013 | bll | 142.31 | 50.23 | 20.09 | 0.0306 |
| RGB J2054+002 | bll | 313.74 | 0.26 | 26.79 | 0.0315 |
| 1ES 1028+511 | bll | 157.83 | 50.89 | 35.27 | 0.0333 |
| GB6 J0331+6307 | bcu II | 52.97 | 63.14 | 26.86 | 0.0335 |
| PKS 2320-035 | fsrq | 350.88 | -3.28 | 15.57 | 0.0350 |
| GB6 J0934+3926 | bll | 143.53 | 39.44 | 32.46 | 0.0352 |
| B2 1811+31 | bll | 273.40 | 31.74 | 35.37 | 0.0356 |
| GB6 J0937+5008 | fsrq | 144.30 | 50.15 | 27.81 | 0.0357 |
| TXS 1015+057 | fsrq | 154.62 | 5.51 | 19.30 | 0.0361 |
| TXS 1614+473 | fsrq | 243.92 | 47.19 | 16.66 | 0.0374 |
| 4C +04.42 | fsrq | 185.59 | 4.22 | 19.22 | 0.0376 |
| MG2 J110606+2812 | fsrq | 166.53 | 28.21 | 41.99 | 0.0396 |
| RX J1246.9+4423 | bll | 191.75 | 44.39 | 22.30 | 0.0396 |
| B2 2308+34 | fsrq | 347.77 | 34.42 | 41.08 | 0.0408 |
| TXS 2106-030 | bll | 317.19 | -2.84 | 16.86 | 0.0410 |
| NVSS J125820+612049 | bll | 194.59 | 61.35 | 36.36 | 0.0425 |
| SBS 0812+578 | bll | 124.09 | 57.65 | 41.15 | 0.0426 |
| WN B1609.6+8517 | bcu II | 240.13 | 85.16 | 37.14 | 0.0434 |
| PMN J2227+0037 | bll | 336.99 | 0.62 | 28.56 | 0.0440 |
| 1RXS J234332.5+343957 | bll | 355.89 | 34.66 | 25.27 | 0.0440 |
| GB6 J0529+0934 | bcu II | 82.26 | 9.58 | 32.69 | 0.0450 |

Continued on next page

Table 5.2 – *Continued from previous page*

| Source Candidate | Source Class | RA (deg) | Dec (deg) | \hat{n}_s | p (pre-trial) |
|-----------------------|--------------|----------|-----------|-------------|-----------------|
| MG2 J131037+2447 | bcu III | 197.66 | 24.81 | 27.71 | 0.0458 |
| 3C 454.3 | fsrq | 343.49 | 16.15 | 37.56 | 0.0459 |
| GB6 J0929+7304 | bcu II | 142.43 | 73.07 | 25.62 | 0.0459 |
| ZS 0214+083 | bll | 34.32 | 8.62 | 36.08 | 0.0485 |
| 3C 264 | rdg | 176.27 | 19.61 | 36.47 | 0.0485 |
| RXS J094620.5+010459 | bll | 146.58 | 1.08 | 19.50 | 0.0486 |
| NRAO 512 | fsrq | 250.12 | 39.78 | 21.52 | 0.0490 |
| 1H 0323+022 | bll | 51.56 | 2.42 | 43.87 | 0.0494 |
| GB6 J1027+7428 | bcu II | 156.85 | 74.47 | 31.92 | 0.0495 |
| RX J0805.4+7534 | bll | 121.36 | 75.57 | 30.25 | 0.0505 |
| 4C +73.07 | bcu II | 142.25 | 72.95 | 22.60 | 0.0514 |
| B3 1222+438 | bll | 186.21 | 43.59 | 28.13 | 0.0516 |
| MG1 J120448+0408 | fsrq | 181.22 | 4.14 | 33.72 | 0.0525 |
| GB6 J0148+5202 | bcu III | 27.08 | 52.03 | 19.63 | 0.0556 |
| 7C 1823+6856 | bll | 275.89 | 68.96 | 21.57 | 0.0561 |
| MG2 J180948+2910 | bll | 272.44 | 29.17 | 34.89 | 0.0591 |
| NVSS J022304+682154 | bcu II | 35.77 | 68.37 | 31.49 | 0.0591 |
| OM 280 | bll | 177.58 | 24.30 | 42.49 | 0.0626 |
| PKS 1717+177 | bll | 259.80 | 17.75 | 24.64 | 0.0627 |
| 1RXS J133021.4+444117 | bll | 202.59 | 44.69 | 22.24 | 0.0650 |
| S4 1726+45 | fsrq | 261.87 | 45.51 | 34.78 | 0.0664 |
| RX J1702.6+3115 | bll | 255.66 | 31.26 | 25.34 | 0.0664 |
| SBS 1410+530 | bcu I | 212.96 | 52.82 | 24.04 | 0.0666 |
| MG1 J154628+1817 | bll | 236.60 | 18.29 | 40.11 | 0.0668 |
| MG2 J190411+3627 | bcu II | 286.05 | 36.45 | 34.19 | 0.0713 |

Continued on next page

Table 5.2 – *Continued from previous page*

| Source Candidate | Source Class | RA (deg) | Dec (deg) | \hat{n}_s | p (pre-trial) |
|-----------------------|--------------|----------|-----------|-------------|---------------|
| TXS 2331+073 | fsrq | 353.55 | 7.61 | 27.29 | 0.0731 |
| PKS 2047+098 | bcu II | 312.44 | 10.05 | 19.18 | 0.0734 |
| GB6 J1542+6129 | bll | 235.74 | 61.50 | 34.32 | 0.0736 |
| S5 0159+723 | bll | 30.89 | 72.55 | 30.54 | 0.0765 |
| TXS 2032+117 | fsrq | 308.65 | 11.91 | 21.51 | 0.0777 |
| S5 1027+74 | bcu I | 157.84 | 74.70 | 30.89 | 0.0777 |
| RGB J1426+340 | bll | 216.53 | 34.07 | 45.49 | 0.0778 |
| B3 0350+465 | bcu III | 58.63 | 46.72 | 22.88 | 0.0778 |
| RGB J1742+597 | bll | 265.63 | 59.75 | 37.12 | 0.0781 |
| 1RXS J125117.4+103914 | bll | 192.82 | 10.65 | 18.18 | 0.0782 |
| MG3 J184126+2910 | bcu II | 280.34 | 29.16 | 37.55 | 0.0787 |
| TXS 1645+635 | fsrq | 251.49 | 63.50 | 36.91 | 0.0793 |
| B3 1058+413 | bcu III | 165.35 | 41.06 | 44.91 | 0.0799 |
| 87GB 152947.5+574636 | bll | 232.74 | 57.61 | 21.01 | 0.0802 |
| GB6 J0229+6706 | bcu III | 37.34 | 67.11 | 11.03 | 0.0806 |
| MG1 J125348+0326 | bll | 193.45 | 3.44 | 27.69 | 0.0806 |
| GB6 J0342+3858 | fsrq | 55.57 | 38.99 | 33.59 | 0.0806 |
| PMN J0148+0129 | bll | 27.14 | 1.48 | 18.43 | 0.0818 |
| 87GB 164812.2+524023 | bll | 252.35 | 52.59 | 33.97 | 0.0827 |
| GB6 J0024+0349 | fsrq | 6.19 | 3.82 | 31.06 | 0.0830 |
| B3 1307+433 | bll | 197.36 | 43.08 | 22.38 | 0.0839 |
| NVSS J092542+595812 | bll | 141.43 | 59.97 | 17.27 | 0.0913 |
| TXS 1549+089 | bll | 238.01 | 8.85 | 30.66 | 0.0915 |
| RX J0202.9-0223 | bcu II | 30.72 | -2.39 | 11.81 | 0.0922 |
| PKS 1203+04 | ssrq | 181.58 | 4.10 | 39.00 | 0.0926 |

Continued on next page

Table 5.2 – *Continued from previous page*

| Source Candidate | Source Class | RA (deg) | Dec (deg) | \hat{n}_s | p (pre-trial) |
|---------------------|--------------|----------|-----------|-------------|-----------------|
| 3C 221 | rdg | 143.78 | 39.70 | 28.81 | 0.0931 |
| RBS 0909 | bll | 162.86 | 39.72 | 30.20 | 0.0942 |
| NVSS J121500+500216 | bll | 183.75 | 50.04 | 36.18 | 0.0956 |
| RX J1101.3+4108 | bll | 165.35 | 41.15 | 39.73 | 0.0962 |
| OX 131 | fsrq | 320.25 | 19.02 | 28.54 | 0.0970 |
| PKS 0017+200 | bll | 4.91 | 20.36 | 25.43 | 0.0973 |
| 1ES 0647+250 | bll | 102.69 | 25.05 | 33.94 | 0.0990 |
| TXS 0237+655 | bcu II | 40.34 | 65.72 | 22.76 | 0.102 |
| NVSS J224753+441317 | bll | 341.97 | 44.22 | 29.52 | 0.102 |
| OI 280 | fsrq | 117.72 | 12.52 | 22.89 | 0.102 |
| B2 1348+30B | fsrq | 207.72 | 30.58 | 27.45 | 0.102 |
| TXS 1833+137 | bcu III | 278.90 | 13.81 | 23.62 | 0.105 |
| RX J1027.4+6317 | bll | 156.85 | 63.30 | 31.32 | 0.105 |
| PKS 2354-021 | bll | 359.35 | -1.87 | 5.92 | 0.105 |

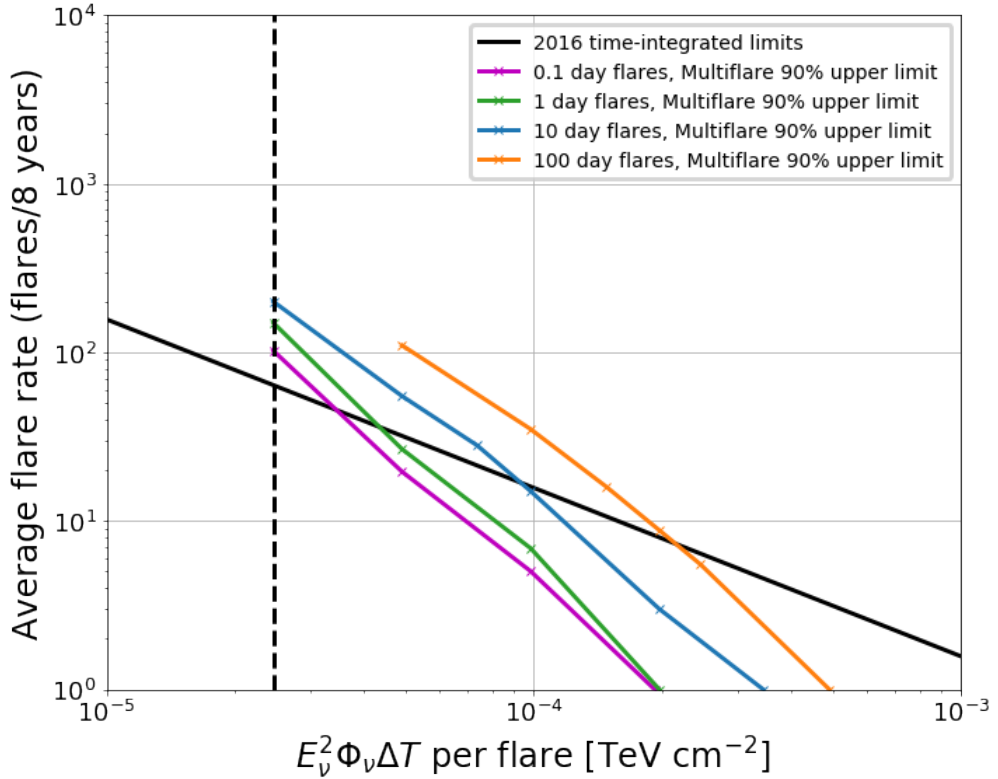


Figure 5.10: The 90% upper limits associated with the non-detection of a multi-flare signal using the 3LAC blazar catalog. The solid black line represents the time integrated limits obtained from [?]. Colored curves represent limits associated with various flare durations, as the multi-flare method imposes more stringent limits in the case that flares are shorter (for a fixed E^2 flux per flare). Note that the parameter space that is realistically accessible to a time-dependent analysis is somewhat compressed: points below the x-axis do not produce more than 1 flare in the data sample, on average, and points to the left of the vertical dashed line have an average flare size of < 1 event. The limits associated with flares with durations $\Delta t < 0.1$ days are expected to be similar to the limits associated with 0.1-day flares, as the improvement in sensitivity asymptotes as the injected flare duration decreases.

1170 Chapter 6

1171 An All-Sky Multi-flare Analysis

1172 6.1 Motivation

1173 While the previous section outlined the application of the multi-flare algorithm to a pair
1174 of source catalogs, an additional obvious application of the method is to simply apply the
1175 algorithm across the entire neutrino sky. While catalog searches have the advantage of a
1176 greatly reduced trial factor, they also rely on having a mostly-correct guess of the underlying
1177 source population. By contrast, an all-sky search could potentially reveal sources without
1178 requiring any prior knowledge of what the specific sources could be, and could additionally
1179 even identify astrophysical neutrino sources with no multi-messenger counterpart. Given the
1180 results of a temporally untriggered neutrino flare associated with TXS 0506+056 [3], it is
1181 only natural to ask whether other such flares exist in IceCube’s astrophysical neutrino data.
1182 An all-sky multi-flare analysis would be an appropriate approach of detecting a population
1183 of TXS-like flares, should they exist.

1184 Similar to the Fermi all-sky variability analysis (FAVA) produced by the Fermi collabora-
1185 tion [?], an IceCube multi-flare skymap provides a description of the temporal variability
1186 of every point in the sky. Even in the absence of a statistically significant population of
1187 neutrino flares, these neutrino “flare curves” may be of use for multi-messenger analyses in
1188 the future, similar to what was done for TXS 0506+056 [3][2].

1189 6.2 Analysis Construction

1190 Conceptually, the construction of an all-sky multi-flare analysis is fairly straightforward: a
 1191 grid of pixels with is defined over the entire sky using the HEALPY software package [?]. Using
 1192 a HEALPY grid with a `Nside=256` results in a grid of 786,432 pixels, each with a radius
 1193 of 0.12° . Pixels with declinations $\delta > 85^\circ$ or $\delta < -85^\circ$ are excluded, as the data-driven
 1194 method of estimating background using data scrambled in right ascension does not perform
 1195 well in this region due to the small statistics of declination bands near the poles. The multi-
 1196 flare algorithm is then applied to the central location of each pixel, resulting in a map of
 1197 multi-flare test statistics, each associated with an individual pixel.

1198 The significance of each pixel can then be calculated by comparing the observed multi-
 1199 flare test statistic to a distribution of similar test statistics obtained by applying the above
 1200 procedure to maps of IceCube events that have had their right ascension locations random-
 1201 ized, providing a description of the null hypothesis. Pixels are divided into 40 declination
 1202 bands, and for each declination band a chi-squared distribution is fit to the distribution of
 1203 test statistics in that declination range. A pre-trial local significance for each pixel is calcu-
 1204 lated by comparing a particular pixel test statistic to the chi-squared distribution that was
 1205 fit in the corresponding declination band. Once this has been done for every pixel, a map of
 1206 multi-flare p-values has been obtained, describing the local multi-flare significance of every
 1207 pixel in the sky.

1208 Once a p-value map has been generated, several basic tests can be conducted. The most
 1209 obvious test is to simply check if the most significant pixel is more significant than is expected
 1210 from the background case (a “hotspot” test). A distribution of most significant multi-flare
 1211 p-values is created by applying the procedure above to a set of background maps. The most
 1212 significant pixel in the observed multi-flare map can then be compared to this distribution to
 1213 obtain a final hotspot significance that has been trial-corrected for the all sky trial factor. As
 1214 the event selection is different in the northern and southern skies, this process is conducted
 1215 separately for declinations $\delta > -5^\circ$ and $\delta < -5^\circ$.

1216 Populations of multi-flare sources may also be tested for using a binomial test. A set of
 1217 “spatially independent” local hotspots may be obtained by defining a list of all pixels that
 1218 are at least 1° away from a more significant pixel. The binomial test statistic p-value of the
 1219 population test is then defined as (eq. 6.1):

$$p(k) = \sum_{i=k}^{N_{eff}} \binom{N_{eff}}{i} p_k^i (1 - p_k)^{N_{eff}-i} \quad (6.1)$$

1220 Here, $p(k)$ is correlated with the significance of observing k hot spots with a p-value of p_k
 1221 or less, and N_{eff} is the effective number of trials associated with the list of hot spots, chosen
 1222 to produce proper containment of the final binomial p-values (e.g. a final binomial p-value
 1223 of $p = 0.1$ or less should only occur in 10% of background trials). In this case, $N_{eff} = N_{pixels}$
 1224 produces proper containment. Hot spots are ordered by decreasing significance, and k is
 1225 varied to identify the most significant combination. The $p(k)$ associated with the best fit k
 1226 is then compared to a distribution of $p(k)$ ’s obtained in a similar manner from data scrambled
 1227 in right ascension, resulting in a final post-trial binomial p-value. Like with the study of
 1228 the most significant pixel, this process is conducted separately in the northern and southern
 1229 skies.

1230 Since the multi-flare algorithm fits for every flare candidate at a particular pixel, it is
 1231 trivial to extract the single-flare skymap results from this process as well. The procedure
 1232 is almost identical to that which was outlined above, except instead of using the multi-flare
 1233 test statistic at each pixel, the test statistic of the flare with the highest test statistic at each
 1234 pixel is used. The hotspot and population tests then proceed as normal.

1235 This particular analysis uses the PSTracks003p02 data set.

1236 6.3 Results

1237 6.3.1 Hotspots and Populations Analysis

1238 The multi-flare pre-trial p-value map can be seen in figure 6.1, with the locations of the
 1239 brightest multi-flare pixels marked. The most significant locations identified by the multi-
 1240 flare algorithm have pre-trial p-values of $p = 9.2 \times 10^{-6}$, located at (RA, Dec)=($145.02^\circ, 36.42^\circ$)
 1241 and $p = 3.5 \times 10^{-7}$, located at (RA, Dec)=($126.21^\circ, -24.81^\circ$). These pre-trial p-values can be
 1242 corrected to account for the all-sky trial factor using the process described above, resulting
 1243 in post-trial p-values of $p = 0.69$ for the northern sky hot spot and $p = 0.06$ for the southern
 1244 sky hot spot.

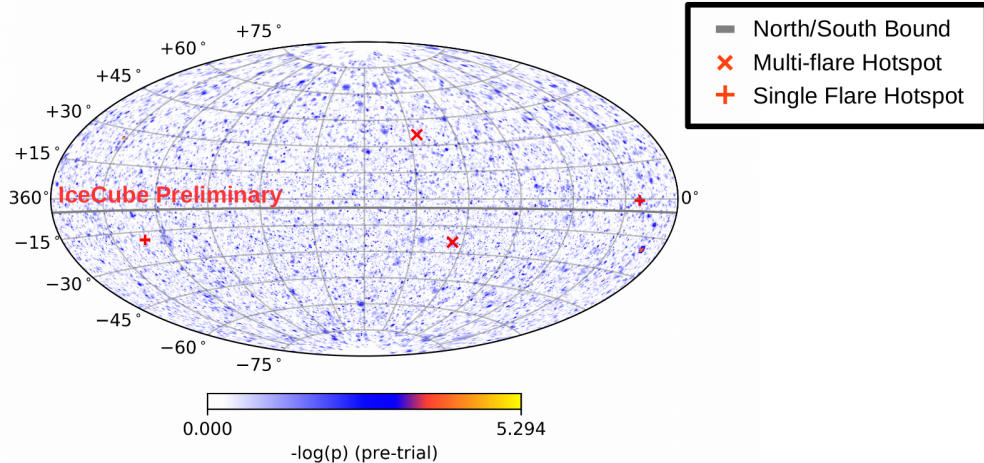


Figure 6.1: The p-value map produced by applying the multi-flare algorithm to the entire neutrino sky between $-85^\circ < \delta < 85^\circ$. The locations of the most significant multi-flare pixels in each hemisphere are shown as red “x’s”, while the locations of the most significant individual flares in each hemisphere are shown as red “+’s”. The gray line denotes the boundary between what is considered the “northern” and “southern” sky by the IceCube data sample that was used.

1245 The flare curves for the multi-flare hotspots can be seen in figure 6.3. Note that the
 1246 multi-flare test statistic is a measure of the activity of a source integrated over the entire
 1247 livetime of the data sample. While no individual flares that were fit at either the northern
 1248 or southern hotspot are particularly significant on their own, the combination of many

1249 moderately significant flares is what makes these pixels the brightest multi-flare pixels in
 1250 their respective hemispheres.

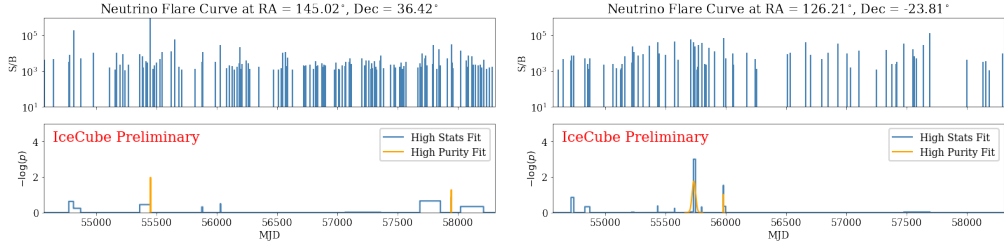


Figure 6.2: The flare curves returned by the multi-flare algorithm for the most significant pixel in the northern sky (left), and southern sky (right). For comparison, a complementary high-purity fit that uses a gaussian hypothesis and more stringent cuts on flare decorrelation is shown in orange. In both the northern and southern sky, the multi-flare significance is fueled not by individual flares with high local significance, but rather by a large number of moderately significant flares.

1251 Since the application of the high-statistics multi-flare analysis involves fitting every pos-
 1252 sible flare in the data, it is trivial to additionally calculate the significance of the largest in-
 1253 dividual flare candidate that was fit in both the northern and southern sky. We find that the
 1254 most significant flare candidate in the northern sky is located at $(\text{RA}, \text{Dec}) = (21.97^\circ, -0.60^\circ)$
 1255 (recall that the “northern sky” refers to declinations between -5° and 85°), and has a pre-
 1256 trial significance of $p = 5.08 \times 10^{-6}$ ($p = 0.82$ post-trial). The most significant flare candidate
 1257 in the southern sky is located at $(\text{RA}, \text{Dec}) = (311.66^\circ, -18.84^\circ)$, and has a pre-trial signifi-
 1258 cance of $p = 6.8 \times 10^{-6}$ ($p = 0.53$ post-trial).

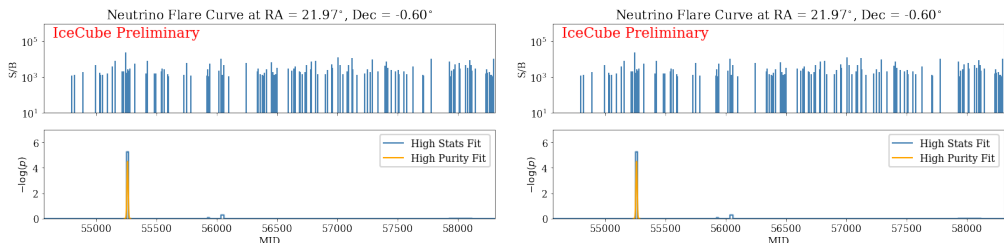


Figure 6.3: The flare curves returned by the multi-flare algorithm for the most significant flares identified in the northern sky (left), and southern sky (right). For comparison, a complementary high-purity fit that uses a gaussian hypothesis and more stringent cuts on flare decorrelation is shown in orange. Since neither of these locations appear to display significant activity beyond the large individual flares, these do not constitute particularly significant locations from a multi-flare perspective.

1259 In addition to examining the most significant pixels that were seen, it is also informative
 1260 to conduct a population analysis on the set of spatially independent ($> 1^\circ$ separation)
 1261 hotspots using the binomial test framework described above. In both the northern and
 1262 southern sky, the binomial test was conducted for the set of spatially independent hotspots,
 1263 defined by both the local multi-flare and single-flare significance. In all cases, the best-fit
 1264 combination of hotspots was $k = 1$, tagging only the most significant pixel, and none of the
 1265 associated binomial p-values were significant (results may be viewed in table 6.1).

| Analysis | Search | Hemisphere | Pre-trial p-value | Post-trial p-value |
|--------------|-----------------|------------|-----------------------|--------------------|
| Multi-flare | Hottest spot | North | 9.2×10^{-6} | 0.69 |
| | | South | 3.5×10^{-7} | 0.06 |
| | Population test | North | 0.98 | 0.98 |
| | | South | 0.12 | 0.12 |
| Single Flare | Hottest spot | North | 5.08×10^{-6} | 0.82 |
| | | South | 6.70×10^{-6} | 0.53 |
| | Population test | North | 0.88 | 0.88 |
| | | South | 0.91 | 0.91 |

Table 6.1: Summary of the tests that were performed on the unblinded multi-flare skymap. Both hotspot and population analyses were conducted using both the local multi-flare significance (summing contributions from all flare candidates at a particular location) and the local single-flare significance (taking only the largest flare fit at each location). There were no significant transient neutrino sources identified by any of the tests conducted.

1266 The results of the population analysis are unsurprising, given the distribution of per-
 1267 pixel local p-values observed from the data. In the presence of a significant population of
 1268 flaring neutrino sources, some deformation of the local p-value distribution should be visible,
 1269 however as can be seen in figure 6.5, the observed distribution is entirely consistent with
 1270 what is expected from background maps.

1271 Similar to the p-value distributions, the distributions of fitted flare parameters are also
 1272 consistent with the background expectation, as can be seen in figure 6.6. There does not
 1273 appear to be a significant sub-population of transient sources with a particular flare duration,
 1274 spectral index, flare rate, or flare flux.

1275 The observed diffuse astrophysical neutrino flux [?] places restrictions on how bright and

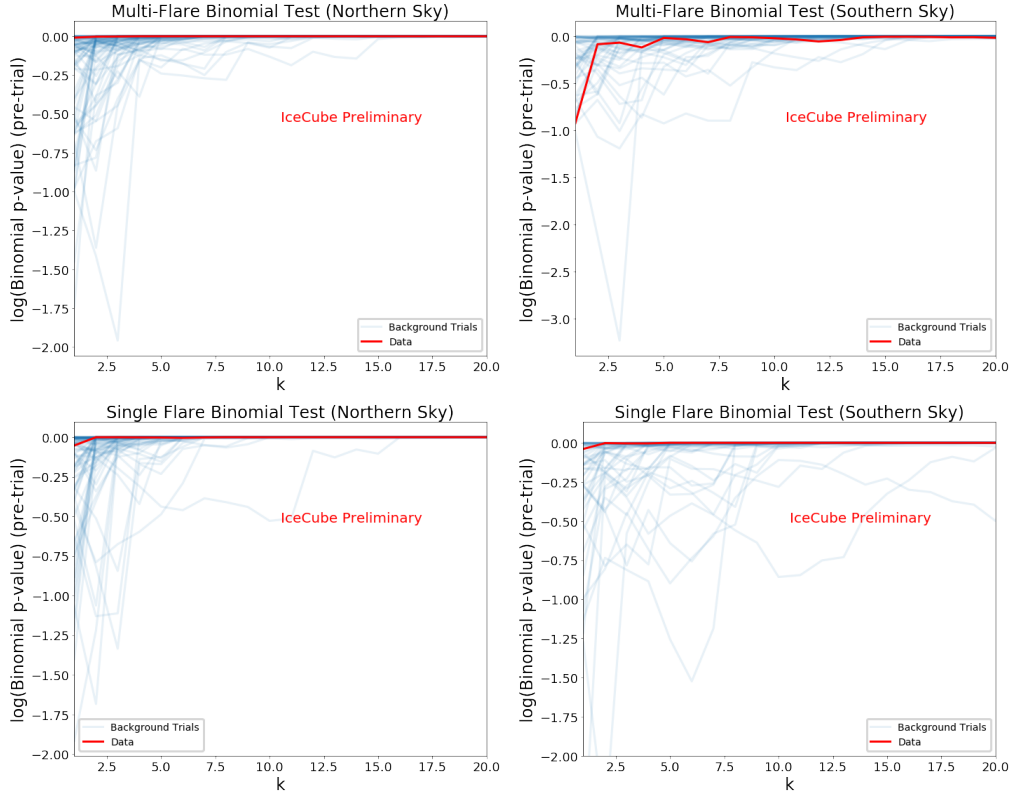


Figure 6.4: The local significance of the binomial test for various values of k , the fitted number of hotspots, for both single and multi-flare binomial tests conducted in both the northern and southern hemispheres. Unblinded data is shown in red, while results obtained from background maps are shown in blue. In all cases using unblinded data, the observed binomial test curve has a global minimum at $k = 1$, with an associated p-value that is consistent with the background expectation.

numerous neutrino flares may be. The non-detection of a population of transient astrophysical neutrino sources can be used to further constrain this space. These limits can be seen in figure 6.7, which shows 90% upper limits on source flare rate and burst energy in neutrinos, as well as limits that can be placed on the per-source flare rate. Note that these limits are a statistical statement about the data itself: If the “true” parameters describing a population of transient neutrino sources lies above these lines, the data would have had a larger population of significant flares than what was observed.

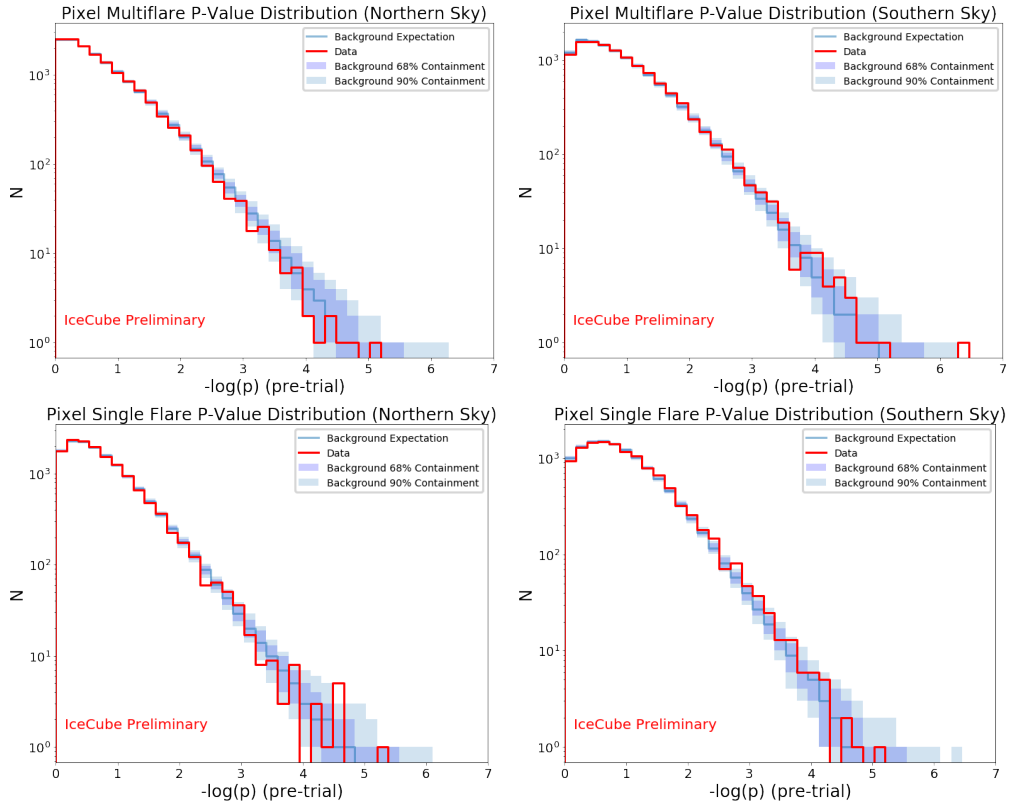


Figure 6.5: The local p-value distributions for the local multi-flare pixel significance (top) and the local single-flare pixel significance (bottom), for both data (red) and background maps (blue bands). In all cases, the observed distribution is consistent with the background expectation.

1283 6.3.2 Locations of External Interest

1284 Though this analysis was designed to be spatially untriggered (scanning over the entire sky,
 1285 rather than the locations of a select few sources), the neutrino “flare curves” produced are a
 1286 potentially powerful tool for exploring the historical behavior of source candidates identified
 1287 though other methods. The skymap produced here is similar to the TXS 0506+056 followup
 1288 analysis [3], except that this analysis has now been performed at almost every location in
 1289 the sky. This allows for easy followup of external triggers, as identifying potential transient
 1290 neutrino emission associated with a source candidate is as easy as examining the flare curve
 1291 at that location in the sky.

1292 To demonstrate the use of the all-sky flare curve map produced here, we examine the
 1293 flare curves of several time-integrated source candidates identified by [4] in order to explore

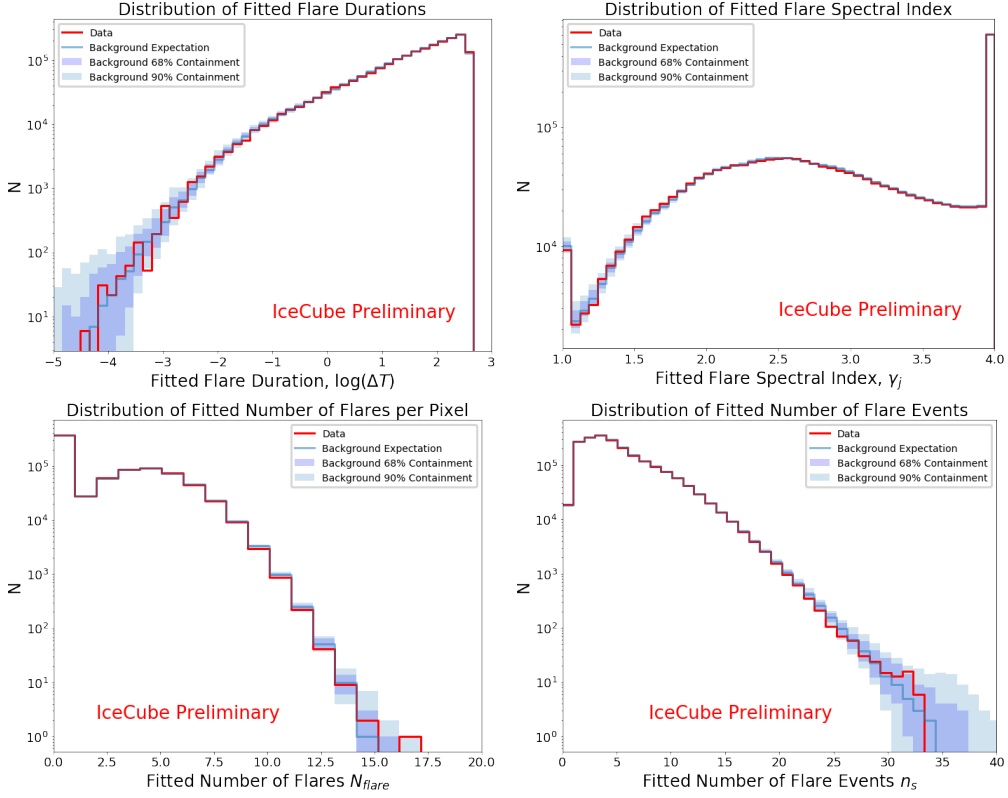


Figure 6.6: Distributions of fitted flare parameters: flare duration (top, left), spectral index (top, right), number of flares fit at a particular candidate location. The peaks at $\gamma = 1.0$ and $\gamma = 4.0$ seen in the spectral index fit plot are due to the edges of the tested parameter space, as only spectral indices ranging from $\gamma = 1.0$ to $\gamma = 4.0$ were tested. In most cases, these flares are also low significance, containing few events, resulting in a poor estimate of the spectral index.

1294 the potential of temporally clustered neutrino emission from these locations.

1295 6.3.2.1 NGC 1068

1296 The most significant location identified by the all-sky time-integrated analysis is spatially
 1297 coincident with the Seyfert II galaxy NGC 1068. This source was also tested as part of
 1298 a catalog of 110 candidate neutrino emitters, and was the brightest object in the catalog,
 1299 with an associated post-trial significance of 2.9σ [4]. These significances all arise from time-
 1300 integrated tests that do not take into account the arrival time of the contributing neutrino
 1301 events. It is then potentially interesting to explore the temporal structure of this excess with
 1302 the flare curves that were produced as part of the multi-flare skymap.

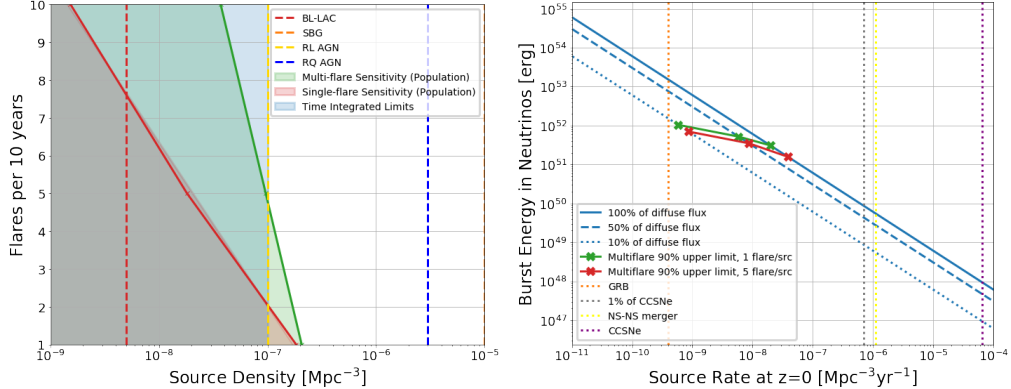


Figure 6.7: Left: 90% upper limits on neutrino source density and per-source flare rate obtained from the all-sky multi-flare analysis. In this plot, transient sources are assumed to compose 100% of the astrophysical neutrino flux, with the FIRESONG simulation package [?] being used to distribute the flux among sources according to the Hopkins and Beacom (2006) source evolution model [?]. Flares are simulated to have a duration of 20 days, and a spectral index of $\gamma = 2.28$. All flares on the same source are assumed to have the same intrinsic intensity, equal to the time integrated source flux divided by the number of flares. Right: The 90% upper limits on the source rate (source density \times flare rate) as a function of neutrino burst energy. Blue lines correspond to combinations of source rate and neutrino burst energy that reproduce specific fractions of the diffuse astrophysical neutrino flux. In both plots, the parameters associated with several candidate source populations are shown for comparison..

1303 The flare curve generated at the location of NGC 1068 can be seen in figure 6.8. Though
 1304 this location is significant under the time-integrated analysis, the multi-flare p-value is only
 1305 $p = 0.016$ (pre-trial), with no individual flare candidate having a local significance greater
 1306 than $p = 0.072$. Note however, that these results are not in tension with the time-integrated
 1307 significance, as the time-integrated analysis tests only for an excess of events over the entire
 1308 livetime of the sample. By contrast, a source with high multi-flare significance requires that
 1309 events not only be clustered spatially, but temporally as well. As such, sources with high
 1310 time-integrated significance do not necessarily have a correspondingly high multi-flare signif-
 1311 icance, particularly if there is not significant temporal clustering of events that contribute
 1312 to the time-integrated result.

1313 Nonetheless, we have here provided a description of the historical behavior of the neutrino
 1314 emission associated with NGC 1068. Despite the time-integrated excess observed in previous
 1315 analyses, there does not appear to be significant temporal clustering of events at this location.

1316 Physically, this suggests either that NGC 1068 is a constant neutrino emitter (i.e. the
 1317 neutrino emission does not occur all in a single destructive event), the “flare” duration is
 1318 longer than the livetime of the detector (corresponding to a very large acceleration region),
 1319 or the component neutrino flares are exceptionally dim (< 1 event on average per flare),
 1320 but very numerous. The difference between the latter case and a constant neutrino emitter is
 1321 semantics from the point of view of current IceCube data, and distinguishing between these
 1322 two cases would likely require a significantly larger and improved detector.

1323 **6.3.2.2 Other Time-Integrated Candidates: PKS 1424+240 and GB6**

1324 **J1542+6129**

1325 In addition to identifying NGC 1068 as a potential source candidate, the population analysis
 1326 component of the time integrated analysis [4] also identified an excess of 3.3σ associated
 1327 with the combination of the sources NGC 1068, TXS 0506+056, PKS 1424+240, and GB6
 1328 J1542+6129. Figure 6.9 shows the flare curves that were obtained at the locations of PKS
 1329 1424+240 and GB6 J1542+6129.

1330 Similar to NGC 1068, PKS 1424+240 does not display significant temporal clustering
 1331 of neutrino events, and has a local multi-flare p-value of $p = 0.085$. By contrast, GB6
 1332 J1542+612 seems to have a somewhat significant flare candidate beginning at MJD=57564.878
 1333 and ending at MJD=57944.512. The pre-trial significance of this flare candidate alone is
 1334 $p = 0.00173$ (2.9σ). Combining all the flares candidates at the location of GB6 J1542+612
 1335 using the multi-flare test statistics results in a local multi-flare significance of $p = 0.0098$
 1336 (2.3σ). While this is not particularly significant (especially when the all-sky trial factor is
 1337 considered), it does inform us that the period between MJD=57564.878 and MJD=57944.512
 1338 was likely a large contributor to the time-integrated significance for this particular source. If
 1339 there are further multi-messenger signals from this location in the future, the neutrino flare
 1340 candidates at this location may become of interest.

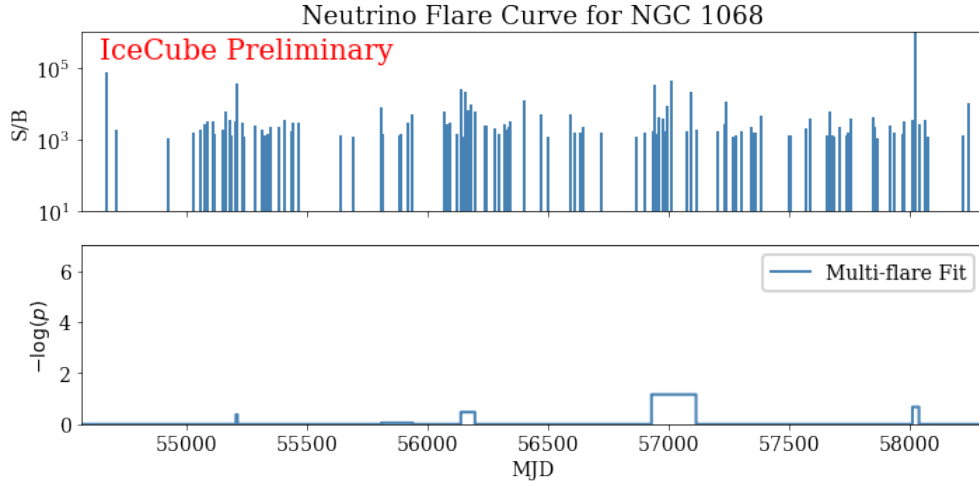


Figure 6.8: The flare curve at the location of NGC 1068, a source candidate that was identified as potentially interesting in the time-integrated analysis [4]. While this is the brightest spot in the time-integrated analysis, the multi-flare analysis does not reveal any significant temporal clustering of events at this location, resulting in a local multi-flare significance of $p = 0.016$

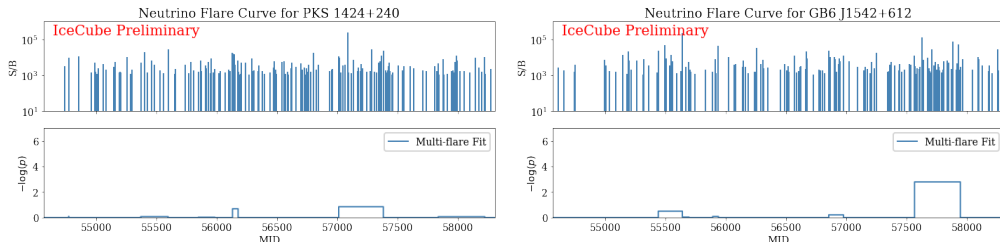


Figure 6.9: The flare curves at the locations of PKS 1424+240 and GB6 J1542+612. While PKS 1424+240 does not display any significant temporal clustering (having a local multi-flare p-value of $p = 0.085$), GB6 J1542+612 has a potentially interesting flare candidate beginning at MJD=57564.878 and ending at MJD=57944.512. This flare candidate has a local flare significance of $p = 0.00173$ (2.9σ), contributing to the overall pre-trial multi-flare significance for GB6 J1542+612 of $p = 0.0098$ (2.3σ).

1341 6.3.2.3 Follow-up of the ANTARES Source Candidate J0242+1101

1342 *Author note: Due to the timing of the request for this follow-up, this section was added 1
1343 week before the submission of this thesis. Results are very preliminary, but I've included it
1344 because I think it's a nice example of how these multi-flare fits can be used to cross check
1345 results from other neutrino telescopes*

1346 The ANTARES telescope [?] is a water cherenkov telescope, similar to IceCube, but lo-
1347 cated in the Mediterranean sea instead of the at the South Pole. It is significantly smaller

1348 than the IceCube detector, consisting of only 12 lines of 25 optical modules each. The lo-
 1349 cation of ANTARES in the northern hemisphere makes it ideal for studying astrophysical
 1350 neutrino events from the southern sky, as the Earth absorbs the atmospheric muon back-
 1351 ground in this region, similar to how IceCube is more sensitive to events from the northern
 1352 sky.

1353 Though ANTARES does not fit for a significant astrophysical diffuse flux [?], the collab-
 1354 oration has still performed searches for point sources of astrophysical neutrinos. Notably, at
 1355 the most recent International Cosmic Ray Conference (2021)¹, the ANTARES collaboration
 1356 presented a temporally untriggered search for correlations between radio-bright blazars and
 1357 neutrino flare candidates in ANTARES data [?]. The ANTARES collaboration noted that
 1358 one of their most significant candidates, J0242+1101, overlapped with the detection of a
 1359 high-energy IceCube event, and contacted the IceCube collaboration for follow-up.

1360 It should be noted that the ANTARES results on their own are not statistically signifi-
 1361 cant: the most significant source candidate has a post-trial p-value of only 40%, and only 7
 1362 source candidates have pre-trial significances greater than 3σ (equivalent to the background
 1363 expectation when testing 2774 sources). Nonetheless, for the sake of completeness, the Ice-
 1364 Cube collaboration assembled a followup analysis, of which the multi-flare fits shown below
 1365 were a part.

1366 Since multi-flare fits were created for the entire sky as part of the multi-flare skymap
 1367 analysis described above, follow-up is potentially as easy as pulling the appropriate flare curve
 1368 from the stored skymap file containing flare fits at every location. However, for the sake of
 1369 completeness, in this particular case the multi-flare analysis was re-run at the exact location
 1370 of the ANTARES source candidate ($J0242+1101$, $RA=40.62^\circ$, $Dec=11.01^\circ$), in addition
 1371 to modifying the flare candidate seeding procedure to ensure that flare candidates with
 1372 durations up to $\Delta t = 1000$ days were tested.

1373 The results of the multi-flare followup for J0242+1101 can be seen in figure 6.10. No
 1374 significant flares were fit, with the largest flare candidate in IceCube data having a local
 1375 significance of only $p = 0.31$. There was also not an excess of flares observed, with the pre-

1376 trial multi-flare significance of this location being $p = 0.52$. The 50 TeV IceCube event that
 1377 was noted by ANTARES in [?] does not appear to be significant in the timing distribution
 1378 of Icecube events, as the flare search algorithm was unsuccessful in pairing that event up with
 1379 other IceCube events to fit a significant flare.

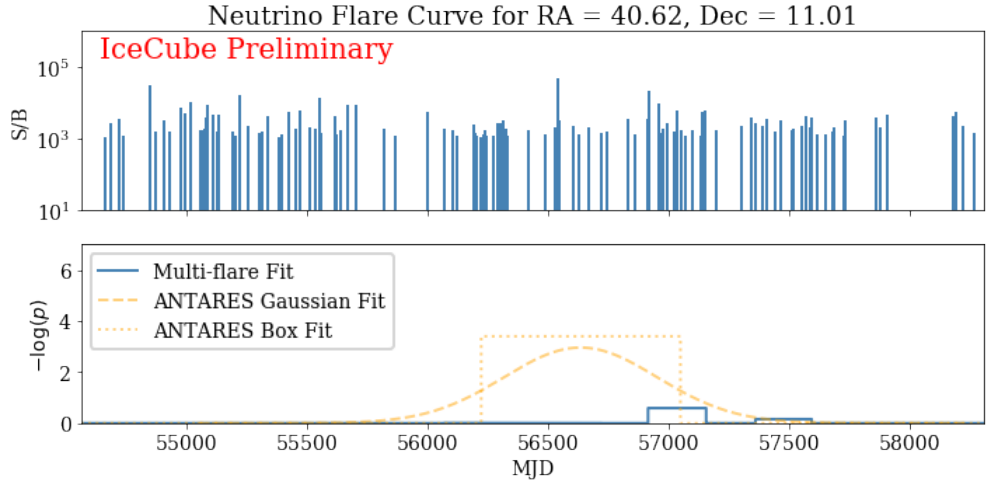


Figure 6.10: The flare curve at the location of J0242+1101, a source candidate that was identified as potentially interesting by the ANTARES collaboration. The results of the untriggered flare fits performed by the ANTARES collaboration are shown in orange, while the blue shows the IceCube data (top-panel), and corresponding multi-flare fit (bottom panel). There does not appear to be a flare as strong as the reported ANTARES flare in IceCube data, with the IceCube multi-flare followup presented here returning a p-value of only $p = 0.52$.

1380 **6.3.2.4 TXS 0506+056**

1381 In addition to being part of the excess that was identified in the all-sky time-integrated
 1382 analysis, TXS 0506+056 is notable for both the multi-messenger coincidence sparked by the
 1383 high energy IceCube alert IC-170922A [2], as well as the archival analysis that revealed a
 1384 3.5σ neutrino flare that occurred in 2014, prior to the 2017 high energy alert event [3].

1385 The all-sky multi-flare analysis presented in this work includes the location of TXS
 1386 0506+056, and we can consequently generate a flare curve for this source candidate. The
 1387 flare curve observed in the all-sky multi-flare analysis can be seen in figure 6.11. TXS

¹<https://icrc2021.desy.de/>

1388 0506+056 has a local multi-flare significance of $p = 3.37 \times 10^{-4}$ (3.4σ), with the main
 1389 contributor being the 2014 neutrino flare candidate, beginning on MJD=56927.86 and ending
 1390 on MJD=57072.99.

1391 Readers who have been paying close attention to the content of this thesis (a group which
 1392 at this point probably includes my thesis committee and like, no one else) may notice that
 1393 the flare curve shown in figure 6.11 seems to be in disagreement with the published result
 1394 with regards to the 2014 TXS flare . While the result shown in [3] reports a significance for
 1395 the 2014 flare candidate of 3.5σ , the all-sky multi-flare analysis presented here observes a
 1396 local significance for this flare of only $p = 0.0054$ (2.5σ).

1397 The difference in significance between the two results can be explained by the different
 1398 event selections that were used in each analysis. Descriptions of these event samples may
 1399 be found in section 3 of this thesis. While [2] used the PointSourceTracks v002p03 event
 1400 sample, the all-sky multi-flare analysis presented here uses the PointSourceTracks v003p02
 1401 event sample. The most relevant difference between the two event samples in this case are
 1402 the pre-cuts: PointSourceTracks v003p02 introduces a cut prior to the event selection BDT
 1403 that requires events to have a reconstructed track length greater than 200 meters. This
 1404 pre-cut does not exist in PointSourceTracks v002p03.

1405 As a result of the track length precut that was introduced in PointSourceTracks v003p02,
 1406 two events (referred to by their event IDs: 40914587 and 56262988) that were major contrib-
 1407 utors to the 2014 TXS 0506+056 neutrino flare candidate were removed. These events have
 1408 a cascade-like topology, though in PointSourceTracks v002p03, they are reconstructed as if
 1409 they were tracks, leading to potentially inaccurate descriptions of the event direction and
 1410 energy. Since these events are cascade-like, they have a short reconstructed track length,
 1411 and as such these events do not exist in PointSourceTracks v003p02. It is additionally worth
 1412 noting that even as cascades, these events are poorly localized, as they are only partially
 1413 contained in the detector. Attempts at reconstructing these events as cascades using the
 1414 methods described in [?] failed to produce any kind of useful directional estimate.

1415 Manually removing the two cascade events from the PointSourceTracks v002p03 data

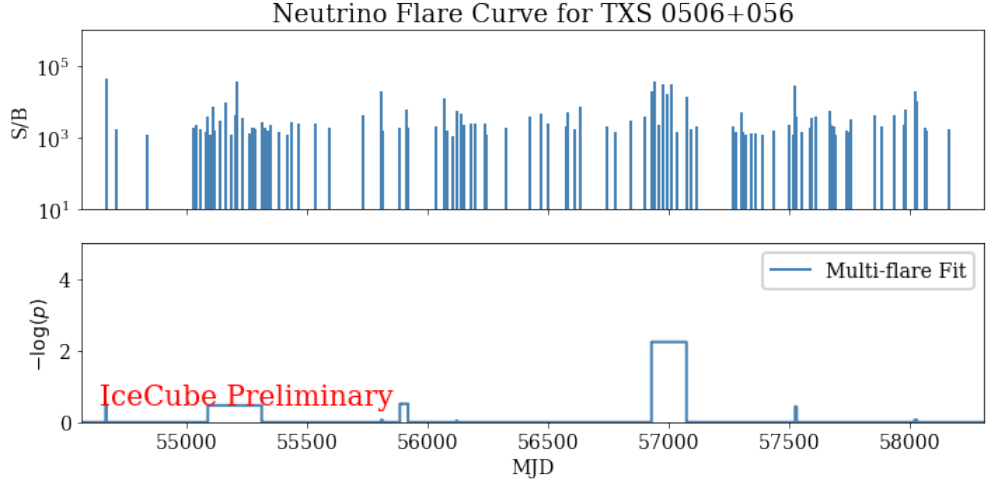


Figure 6.11: The flare curve obtained from the all-sky multi-flare analysis for TXS 0506+056. The pre-trial multi-flare significance of this location is $p = 3.37 \times 10^{-4}$ (3.4σ). Interestingly, the 2014 flare candidate is not seen at the original significance of 3.5σ that was reported in [2]. While the 2014 flare candidate is present, this analysis obtains an associated local significance of only $p = 0.0054$ (2.5σ).

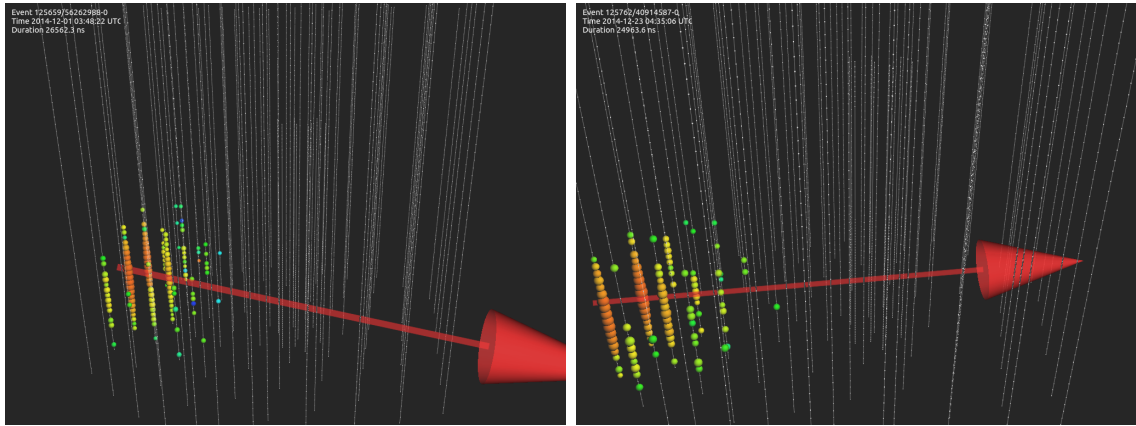


Figure 6.12: The two cascade-like events (event IDs: 40914587 and 56262988) that contributed to the 2014 TXS 0506+056 neutrino flare candidate in PointSourceTracks v002p03, but are not present in PointSourceTracks v003p02. The red arrows show the directional reconstruction associated with the track reconstruction that was used, however given the cascade topology of these events, this reconstruction is likely to be inaccurate.

1416 sample and recomputing the significance of the 2014 TXS 0506+056 neutrino flare results in
 1417 a drop in significance comparable to what was seen when using PointSourceTracks v003p02,
 1418 as can be seen in table 6.2. The drop in significance cannot be otherwise adequately explained
 1419 by changes to the angular reconstruction or other differences between the two versions of
 1420 the data sample. The time-integrated sensitivity of the two samples is comparable, and

1421 favors PointSourceTracks v3 at the declination of TXS 0506+056. As such, the drop in
 1422 significance of the 2014 TXS 0506+056 flare candidate is unlikely to have been caused by
 1423 PointSourceTracks v003p02 being an overall less sensitive sample.

Untriggered Flare Cross-check Results

| Sample | p (pre-trial) | T_{start} | T_{stop} | n_s | γ |
|----------------------------------|-----------------|--------------------|-------------------|-------|----------|
| PSTracks v2 [3] | 7.0e-5 | 56937.81 | 57096.22 | 14.39 | 2.20 |
| PSTracks v2 w/o cascades | 1.17e-3 | 56937.81 | 57112.65 | 12.22 | 2.26 |
| PSTracks v3 (multi-flare skymap) | 5.4e-3 | 56927.86 | 57072.99 | 11.87 | 2.22 |

Table 6.2: The results of repeating the untriggered flare analysis preformed in [3], but using PSTracks v3 in place of PSTracks v2, the dataset that was originally used. The apparent drop in significance when using PSTracks v3 can be explained by cascade-like events present in v2 that have been removed from v3.

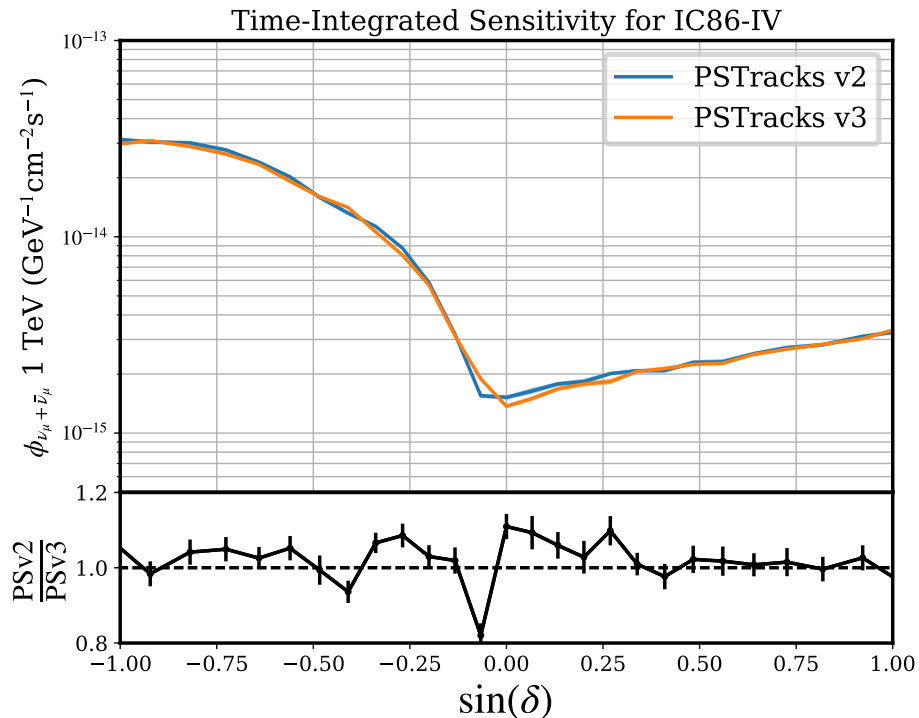


Figure 6.13: A comparison of the time integrated sensitivities of PointSourceTracks v002p03 and PointSourceTracks v003p02. At the declination of TXS 0506+056 ($\delta = 5.7^\circ$), PointSourceTracks v003p02 has a slightly better sensitivity.

1424 It should be noted that the result published in [3] is not incorrect, despite using an
 1425 older data sample that contains unforeseen background events. Since the methods used for

1426 the original untriggered flare analysis use a data-driven background estimation, the cascade
 1427 background in PointSourceTracks v002p03 is accounted for in the original 3.5σ significance
 1428 that was reported for the 2014 neutrino flare candidate. Whether or not the cascade-like
 1429 events are removed from the sample prior to the analysis, or left in the data sample and
 1430 accounted for with the statistical method is simply a choice that can be made by the analysis
 1431 architects, and both options are entirely statistically valid.

1432 Though the cascade background is handled differently in the PointSourceTracks v002p03
 1433 analysis versus the PointSourceTracks v003p02 analysis, the two results are not inconsistent
 1434 with one another. Figure 6.14 shows the results of comparing the results of simulated
 1435 flares comparable to the 2014 TXS flare injected into both PointSourceTracks v002p03 and
 1436 PointsourceTracks v003p02. As the background test statistic distributions for both samples
 1437 are similar, comparing the test statistic values obtained using each sample is a good proxy for
 1438 comparing the flare local significance. For this test, trials of simulated signal at the location
 1439 of TXS 0506+056 were injected into background maps generated using PointSourceTracks
 1440 v002p03. The injected signal was chosen to replicate the best fit parameters in the original
 1441 PointSourceTracks v002p03 untriggered flare analysis [3]: 13 events with a spectral index
 1442 of $\gamma = 2.2$, injected over a time window of length $\Delta t = 158$ days. A test statistic for each
 1443 of these PointSourceTracks v002p03 signal trials was then calculated. The same simulated
 1444 signal events were then injected into background trials generated with PointsourceTracks
 1445 v003p02, but any events that do not pass the PointSourceTracks v003p02 event selection
 1446 were removed. A new PointSourceTracks v003p02 test statistic is then calculated for each
 1447 of these trials with injected signal.

1448 Figure 6.14 shows the results of this crosscheck, showing the distribution of test statistics
 1449 differences between the v2 and v3 test statistics. While on average the test statistic associ-
 1450 ated with a signal of this type is higher in PointSourceTracks v003p02, the distribution is
 1451 rather wide, and it is not uncommon for the PointSourceTracks v003p02 result to be lower
 1452 significance than the PointSourceTracks v002p03 result. A drop in significance comparable
 1453 or greater than what was seen in the observed v2 and v3 results ($TS_{v3} - TS_{v2} = 11.84$)

1454 occurs in 8% of the simulated trials.

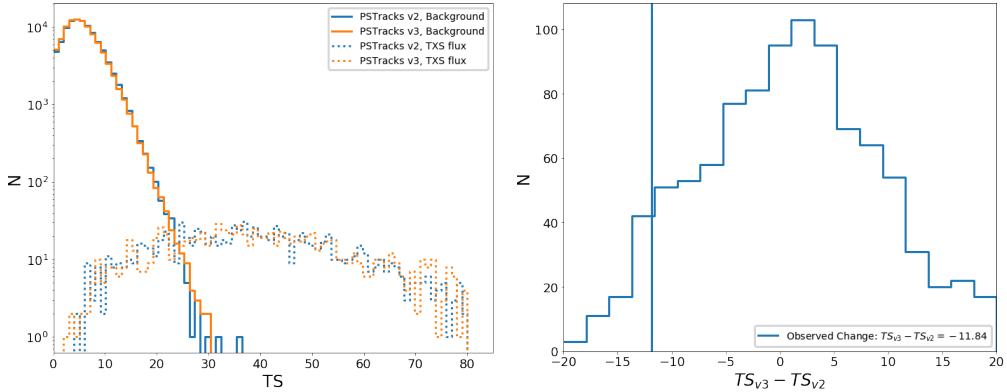


Figure 6.14: Simulated trials comparing the significance of a flare comparable to the 2014 TXS 0506+056 flare in both PointSourceTracks v002p03 and PointSourceTracks v003p02. Left: the test statistic distributions for both datasets in the background (solid) and injected signal (dotted) cases. The PointSourceTracks v003p02 signal is identical to the PointSourceTracks v002p03 signal, except with events that do not pass the v3 selection removed. Right: A comparison of the v2 and v3 test statistics for each simulated signal trial, with the observed test statistic difference plotted as a vertical line. A drop in significance at least as large as what was seen in observed data occurs in 8% of simulated trials.

1455 While there appears to be a drop in significance for the 2014 TXS 0506+056 untrig-
 1456 gered neutrino flare when using to the newer PointSourceTracks v003p02 data sample, it
 1457 is important to realize that the updated v3 result is not inconsistent with the previous v2
 1458 result. Additionally, the 2014 flare composes only part of the ensemble of results that make
 1459 TXS 0506+056 an interesting source candidate, as it is the combination of the 2014 untrig-
 1460 gered neutrino flare with the 2017 high energy alert event and multi-messenger observations
 1461 that suggest TXS 0506+056 as a source of astrophysical neutrinos. The significance of the
 1462 2014 TXS 0506+056 flare will likely continue to be monitored as the IceCube collaboration
 1463 improves its data samples and reconstruction techniques, hopefully converging on a more
 1464 precise measurement to the flare significance.

1465 Chapter 7

1466 Outlook

1467 In this work, we have introduced a novel method for fitting ensembles of neutrino flare
1468 candidates at a particular source location. This method was applied to two catalogs of
1469 source candidates motivated by TXS 0506+056: a catalog of northern-sky 3LAC blazars, and
1470 a “self-triggered” catalog of high energy IceCube events. Though neither catalog displayed
1471 a significant excess of neutrino flares, this allowed us to further constrain potential transient
1472 neutrino emission from blazars.

1473 The multi-flare algorithm introduced here was also applied on an all-sky scale. No signif-
1474 icant population of neutrino flares was observed, though flare curves were produced at every
1475 location in the sky, providing a potentially useful tool for future multi-messenger searches
1476 wishing to incorporate information on the historical neutrino emission from source candidate
1477 locations, similar to what was done in [3].

1478 The non-detection of a significant population of transient neutrino sources is somewhat
1479 interesting from the perspective of constraining astrophysical neutrino source populations.
1480 Whatever the sources of astrophysical neutrinos may be, they cannot produce neutrino flares
1481 that are so bright or numerous that the data becomes inconsistent with the background
1482 expectation on an all-sky scale. This places limits on the source density, flare rate, and
1483 neutrino burst energy that are not associated with any particular source class, serving as a
1484 “universal limit” of sorts on the behavior of potential astrophysical neutrino transients, as

1485 can be seen in figure 6.7.

1486 It should be noted, however, that a non-detection of neutrino sources on an all-sky scale
 1487 is not entirely unexpected. The all-sky trial factor is quite large, and the most significant
 1488 neutrino source candidates to date (TXS 0506+056 and NGC 1068) were both originally
 1489 identified in spatially triggered analyses, where the candidate location was already identified
 1490 as potentially interesting by other astrophysical messengers. Future, spatially triggered
 1491 searches may be sensitive to individual sources that have been obscured by the all-sky trial
 1492 factor. Ideally, the neutrino flare curves introduced in this work would aid with this, as the
 1493 historical neutrino information provides an additional piece to the multi-messenger puzzle.

1494 Though the first applications of the multi-flare algorithm did not yield any significant
 1495 discovery of astrophysical neutrino sources, the future of neutrino astronomy is still quite
 1496 bright. With two interesting source candidates already identified, the answer to the ques-
 1497 tion of the source of astrophysical neutrinos (and consequently, the source of high energy
 1498 cosmic rays) is potentially beginning to become more clear. The upcoming years bring im-
 1499 provements to the IceCube detector calibration and event reconstruction, providing a more
 1500 accurate description of existing data, as well as the construction of IceCube Gen2 which will
 1501 boast increased effective area at high energies, thereby reducing the atmospheric neutrino
 1502 background. Additionally, upcoming radio-based neutrino experiments such as RNO-G [?],
 1503 BEACON [?], IceCube Gen2-Radio [?], PUEO [?], and POEMMA [?] will provide a view
 1504 into the ultra-high energy neutrino regime, beyond what the current iteration of IceCube
 1505 is realistically capable of measuring. As the identification of candidate neutrino emission
 1506 from TXS 0506+056 was triggered by a single high energy neutrino event, the expansion
 1507 of neutrino detectors into the high energy regime could lead the way to identifying future
 1508 neutrino sources.

1509 **Chapter 8**

1510 **Appendix: Statistics Background**

1511 Much of the material presented in this thesis requires an understanding of a few key areas
1512 of statistics. This material is typically covered in almost any introductory level statistics
1513 course, but is generally not part of the standard undergraduate physics curriculum. For
1514 this reason, I've collected some of the key concepts in this section, to potentially serve as a
1515 starting point for people who may not already be familiar with the statistical underpinnings
1516 of recent source searches in neutrino astronomy. An interactive ipython notebook showing
1517 examples of these concepts can also be found as part of the materials for the 2019-2021
1518 IceCube bootcamps¹.

1519 **8.1 Estimators**

1520 An estimator is a procedure applied to the data sample which gives a numerical value for a
1521 property of the parent population, or, as appropriate, a property or parameter of the parent
1522 distribution function.

1523 This is a general definition: The sample of interest may have been drawn from a large
1524 parent population, for which some property is to be inferred. Alternatively, it may have
1525 been generated from a distribution function, arising from a basic law being investigated.

¹<https://events.icecube.wisc.edu/event/105/contributions/1054/>

1526 This distribution function also has parameters and properties, which one may also wish to
 1527 calculate (e.g. σ for a 1 dimensional gaussian distribution).

1528 Estimators are generally not classified as "right" or "wrong", rather we tend to classify
 1529 estimators as "good" or "bad" based on their properties. Some properties that are often
 1530 relevant when describing estimators:

- 1531 • An estimator is *consistent* if it tends to the true value as the number of data values
 1532 tends to infinity.
- 1533 • An estimator is *unbiased* if its expectation value is equal to the true value.
- 1534 • An estimator is *efficient* if its variance is small.

1535 Estimators can be any number of the above, but good estimators should fulfill all three
 1536 descriptions [?].

1537 8.2 Likelihoods

1538 One class of estimators that is commonly used in neutrino astronomy are *likelihood-based*
 1539 *estimators*. For a set of data, $x_1, x_2, x_3 \dots x_N$ produced from some underlying distribution
 1540 with parameter a , the probability of obtaining that particular data set is the product of
 1541 the individual probabilities of obtaining each of the x_i . This product is referred to as the
 1542 *likelihood* (eq. 8.1 and 8.2):

$$L(x_1, x_2, x_3 \dots x_N, a) = P(x_1; a)P(x_2; a) \dots P(x_N; a) \quad (8.1)$$

$$L(x_1, x_2, x_3 \dots x_N, a) = \prod_{i=1}^N P(x_i; a) \quad (8.2)$$

1543 The likelihood is typically used to fit the model parameter a , given some observed data
 1544 $x_1, x_2, x_3 \dots x_N$ by finding the value of a which maximizes the likelihood function. Note that
 1545 a can be a vector of values in the case that we have a model with multiple free parameters.

1546 For computational reasons, the process of maximizing the likelihood is oftentimes done
 1547 by minimizing the negative log-likelihood instead. Taking the logarithm of the likelihood
 1548 function turns the product into a sum, making the derivative more intuitive and easier to
 1549 work with numerically, and the switch from maximization of the likelihood to minimizing
 1550 the negative likelihood is purely convention.

1551 8.3 Confidence Intervals

1552 Suppose we want to know the value of a parameter X and have estimated it from the data,
 1553 giving result x . We know the resolution of our underlying distribution, and thus the variance,
 1554 $V(x)$ and the standard deviation σ . Our goal is then to create a "confidence interval": An
 1555 interval within which there is a C % chance that a single observation will lie within the
 1556 interval, where C is our "confidence level". Formally, the confidence interval (x_-, x_+) for a
 1557 given confidence level C obeys the requirement that (eq. 8.3):

$$Prob(x_- \leq x \leq x_+) = \int_{x_-}^{x_+} P(x)dx = C \quad (8.3)$$

1558 There are a few possible ways to construct this interval:

1559 1. The **symmetric interval**: x_- and x_+ are equidistant from the mean, μ , i.e $x_+ - \mu =$
 1560 $\mu - x_-$

1561 2. The **central interval**: The probability above and below the interval are equal: $\int_{-\infty}^{x_-} P(x)dx =$
 1562 $\int_{x_+}^{\infty} P(x)dx = (1 - C)/2$

1563 Common values for C are 68% (1σ), 90% (1.64σ), and 99% (2.58σ). There is a trade
 1564 off between a narrow interval and low confidence. You can say with great confidence that a
 1565 value will lie within a very wide interval, but if one wants to tie it down more precisely the
 1566 confidence lessens.

1567 8.4 Hypothesis Testing

1568 Many problems in science can be reduced to attempting to distinguish between 2 distinct
 1569 possibilities, where the observed data has different properties under each. In many cases,
 1570 we are attempting to distinguish between a "null hypothesis", which is used to refer to a
 1571 "default" model (e.g. the absence of neutrino point sources), and an "alternative hypothesis",
 1572 which represents the addition of some new physics, model parameter, or disagreement with
 1573 the "default" case (e.g the presence of neutrino point sources). Statistical hypothesis testing
 1574 is a framework for comparing these two hypotheses, given some set of observed data.

1575 We can roughly break down the process of hypothesis testing into the following steps:

- 1576 1. State relevant null and alternative hypotheses
- 1577 2. State the test statistic
- 1578 3. Derive the distribution of the test statistic under the null hypothesis
- 1579 4. Select significance level (α) at which the null hypothesis will be rejected
- 1580 5. Compute an observed test statistic from the data
- 1581 6. Calculate a p-value and decide whether to reject the appropriate hypothesis

1582 8.4.1 State relevant null and alternative hypotheses

1583 When constructing an analysis, we should be careful to state the null and alternative hy-
 1584 potheses. Typically, the null hypothesis (H_o) refers to a statement or default position that
 1585 there is no relationship between two phenomena, that there is no signal, or that our cur-
 1586 rent models describe the data well. The alternative (H_a) hypothesis usually describes the
 1587 opposite: that there is a relationship between two phenomena, that there is a signal, or that
 1588 our models to NOT describe the data well. Here are some example pairs of hypotheses one
 1589 might encounter when working with IceCube data:

1590 • H_o : Neutrino event arrival directions are not significantly correlated with the positions
 1591 of blazars identified in Fermi's 3FGL catalog

1592 • H_a : Neutrino event arrival directions are correlated with the positions of blazars iden-
 1593 tified in Fermi's 3FGL catalog

1594 • H_o : A 3-flavor oscillation model describes the IceCube data well

1595 • H_a : IceCube data is inconsistent with a 3-flavor model

1596 It is important to be careful when formulating null and alternative hypotheses so as to
 1597 not overreach with the claims being made should the alternative hypothesis be accepted.

1598 In general, it's best to keep in mind the specifics of how a particular analysis is being
 1599 constructed, and what the property of the data being measured actually is. For example, in
 1600 the first pair of hypotheses above, it would be improper for our alternative hypothesis to be
 1601 "blazars are a source of astrophysical neutrinos" if we were only examining the positions of
 1602 the 3FGL catalog, which covers only a subset of all observed blazars.

1603 8.4.2 State a test statistic

1604 A *test statistic* is a quantity derived from the sample, intended to be a numerical summary
 1605 of a dataset that reduces the data to one value that can be used for hypothesis testing. In
 1606 general, the test statistic is selected in such a way as to quantify, within observed data,
 1607 behaviors that would distinguish the null and alternative hypotheses. These are very similar
 1608 to estimators, and we can oftentimes use estimators as test statistics.

1609 An important property of the test statistic is that its sampling distribution under the
 1610 null hypothesis must be calculable either exactly or approximately. There are many types of
 1611 test statistics that you can use, and what the exact form of the test statistic is will usually be
 1612 determined by your analysis. One example of a test statistic is the chi-squared test statistic
 1613 intended to compare counts in an oscillation analysis (eq. 8.4):

$$\chi^2 = \sum_{i \in bins} \frac{(n_i^{\nu+\mu_{atm}} - n_i^{data})^2}{(\sigma_i^{data})^2 + (\sigma_{\nu+\mu_{atm},i})^2} \quad (8.4)$$

1614 Where χ^2 is the test statistic, i refers to bins in zenith and azimuth, $n_i^{\nu+\mu_{atm}}$ and n_i^{data} are
 1615 the number of events in a particular bin in both simulation and data, and $\sigma_{\nu+\mu_{atm},i}$ and σ_i^{data}
 1616 are similar the per-bin standard deviations in both simulation and data. This test statistic
 1617 is used to measure the agreement of the data with a "nominal" model that can be simulated
 1618 to obtain the values $n_i^{\nu+\mu_{atm}}$ and $\sigma_{\nu+\mu_{atm},i}$.

1619 Another example of a commonly used test statistic in neutrino astronomy is the point
 1620 source likelihood (eq. 8.5):

$$TS = -2 \log\left(\frac{\mathcal{L}(n_s = 0)}{\mathcal{L}(\hat{n}_s)}\right) \quad (8.5)$$

1621 This is a likelihood ratio test statistic, where \mathcal{L} is a likelihood function that describes
 1622 how clustered events are near a particular location. In its simplest form, this likelihood has
 1623 1 parameter, n_s , that describes the number of excess events seen near the location being
 1624 examined.

1625 The likelihood ratio is a very powerful test statistic. Given two hypotheses H_o and $H_a(a)$
 1626 where $H_o = H_a(\tilde{a})$ (they are *nested* models), then the Neyman-Pearson lemma states that
 1627 the likelihood ratio test has the strongest statistical power (i.e. correctly reject H_o when H_1
 1628 is true). This is the case for many point source searches, where the null hypothesis ("There
 1629 are zero signal events, $n_s = 0$) is nested in the alternative hypothesis ("There are a nonzero
 1630 number of signal events, $n_s > 0$ ").

1631 Note that test statistics are essentially estimators of the alternative hypothesis: a "more
 1632 extreme" test statistic should correspond to the data being better described by the alter-
 1633 native hypothesis. In fact, most test statistics are in fact based on estimators of some
 1634 statistical property of the data. The point source test statistic, for example, is based around
 1635 a likelihood estimator of the number of clustered neutrino events.

1636 **8.4.3 Select a significance level at which the null hypothesis will**
 1637 **be rejected**

1638 Since in testing our hypothesis, we have two options for our result (accept/reject the null
 1639 hypothesis), and there are two options for the "actual" state of our null hypothesis (either
 1640 it is true or it isn't), there are four possible outcomes describing whether we were correct or
 1641 not:

| | | | |
|------|----------------|--------------------------------|--------------------------------|
| | H_o rejected | Accept (Fail to reject) H_o | |
| 1642 | H_o False | Correct | Type II error (false negative) |
| | H_o True | Type II error (false positive) | Correct |

1643 If you reject a true null hypothesis, then this is a type II error. If you accept a false
 1644 null hypothesis, then this is a type I error. "Type I" and "type II" are needlessly confusing
 1645 names, so let's instead refer to these with the more intuitive names "false positive" and
 1646 "false negative".

1647 Both types of errors are bound to happen sometimes, but we're typically more concerned
 1648 with false positives: We don't want to make any claims of discovery when in fact it was
 1649 simply a background fluctuation. We can control the rate at which this happens with the
 1650 "significance" of the test (α). The *significance* refers to the probability of obtaining a false
 1651 positive.

1652 Given a hypothesis test with some test statistic (where we can calculate the distribution
 1653 of this test statistic under the null hypothesis, see above!), we can divide the range of our
 1654 test statistic into the acceptance region, containing test statistics less extreme than some
 1655 pre-defined significance threshold, and the rejection region, containing test statistics more
 1656 extreme than this threshold. If our observed test statistic falls in the acceptance region, we
 1657 will accept the null hypothesis to be true. If our observed test statistic falls into the rejection
 1658 region, we will reject the null hypothesis.

1659 The probability of a false positive is then simply the integral of our null hypothesis test
 1660 statistic distribution over the rejection region. This is the "significance" of the test. In
 1661 principle, we can set the significance of our test to be whatever we want, simply by changing
 1662 the acceptance and rejection regions. In practice, we typically want to set a high bar for
 1663 announcing a result (this corresponds to a low significance). In particle physics, the threshold
 1664 for rejecting the null hypothesis is typically set such that the significance is 2.87×10^{-7} (the
 1665 one-sided five sigma threshold). In other disciplines, the convention is different, with social
 1666 scientists and biologists typically rejecting the null hypothesis at the .01 or .05 significance
 1667 level.

1668 You might sometimes hear significance referred to in units of "sigma" (e.g. " 5σ " or " 3σ ").
 1669 This can be obtained by the process shown in figure 8.1, by mapping the significance to a
 1670 normal distribution. This simply provides a standardized way of describing how "extreme"
 1671 the observed significance is: more "sigmas" corresponds to a result that is less likely to be
 1672 seen under the null hypothesis.

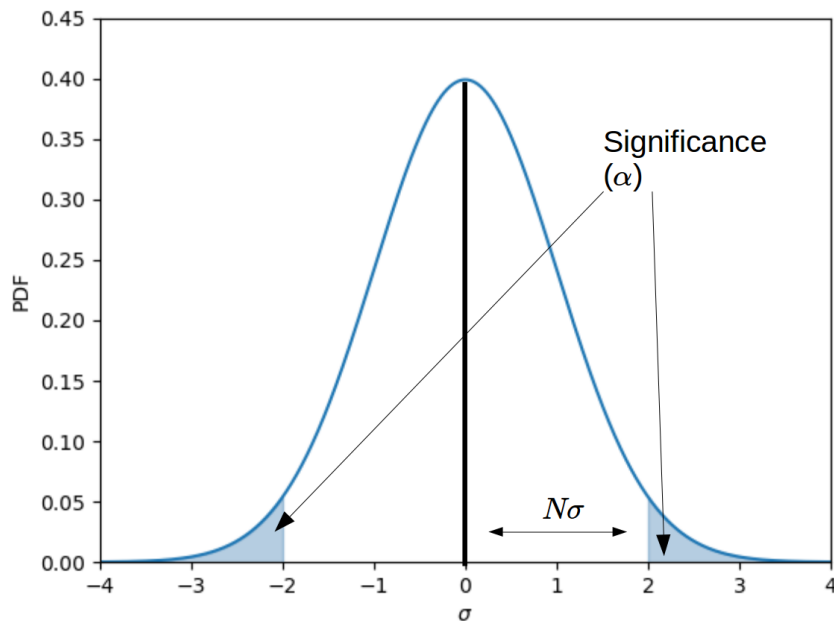


Figure 8.1: The mapping of significance into units of sigma using a normal distribution, for a two tailed test.

1673 **8.4.4 Compute the TS from observed data**

1674 This step is fairly straightforward, as the test statistic has already been defined. Simply
 1675 run your test statistic algorithm using the observed data generated from your experimental
 1676 apparatus.

1677 **8.4.5 Decide whether to accept or reject the null hypothesis**

1678 There are two different, but equivalent constructions for deciding whether to reject the null
 1679 hypothesis or not. The first construction involves pre-defining an *acceptance region* prior
 1680 to calculating the test statistic associated with the observed data. The acceptance region
 1681 corresponds to the range of test statistic values for which the null hypothesis cannot be
 1682 rejected. This is typically chosen to correspond to a particular significance (e.g. 5%, 1%,
 1683 0.01% etc.). If the observed test statistic lies outside of the acceptance region corresponding
 1684 to $X\%$ significance, then we can say that the null hypothesis is rejected at the $X\%$ signif-
 1685 icance level. Note that since we had to pick our significance threshold (and consequently
 1686 define an acceptance region) prior to computing an observed test statistic, we can make no
 1687 further claims on how extreme the result is: if our acceptance region is $TS > 12$, it does not
 1688 matter if we observe a $TS = 12.1$ or if we observe a $TS = 99.0$. In both instances we will
 1689 reject the null hypothesis as the significance level we initially chose.

1690 An alternative, but mathematically equivalent, construction involves the calculation of a
 1691 *p-value*. A p-value is the probability, under the null hypothesis, of obtaining a test statistic
 1692 at least as extreme as the one we have observed from data. If our p-value is smaller than a
 1693 pre-determined significance threshold, then we can reject the null hypothesis. The p-value
 1694 can be calculated by simply integrating our null hypothesis test statistic distribution over
 1695 the range of values more extreme than what was observed. For the one-tailed case where a
 1696 larger test statistic is correlated with stronger evidence of the alternative hypothesis, this is
 1697 (eq. 8.6):

$$p = \int_{TS_{obs}}^{\infty} PDF_{H_0} \quad (8.6)$$

1698 Where TS_{obs} is our observed test statistic and PDF_{H_0} is the distribution of test statistics
 1699 under the null hypothesis. It is important to note that the above equation is only valid for
 1700 the positive, one-tailed case (the alternative hypothesis is only associated with test statistic
 1701 values on one side of the distribution). A more general formula could be expressed as (eq.
 1702 8.7):

$$p = \int_{R|TS_{obs}} PDF_{H_0} \quad (8.7)$$

1703 Where here $R|TS_{obs}$ is the rejection region of the test statistic distribution associated
 1704 with a particular observed test statistic (i.e. it is the region of the background test statistic
 1705 distribution containing values more extreme than what was observed). This distinction is
 1706 particularly important when conducting two-tailed tests, where test statistics that are either
 1707 above an upper bound, or below a lower bound may be cause for rejecting the null hypothesis.

1708 8.5 Trial Factors

1709 Each time you obtain the answer of an analysis from real data, you have done one experi-
 1710 mental trial. It is common to perform multiple trials when working with a specific analysis
 1711 technique.

- 1712 • In the neutrino sources group, we might test the probability that one location is con-
 1713 sistent with background expectation. If we were to apply this framework to a list of
 1714 30 source candidate locations, then this would be 30 trials.
- 1715 • Repeating an analysis with new cuts. We might count the number of neutrinos with
 1716 $E > 1$ TeV in 1 year, then count the number of neutrinos with $E > 10$ TeV in 1 year.
 1717 This would be 2 trials.

- 1718 • Repeating with different signal hypotheses. You might look for emission from blazars
 1719 using both the hypothesis of steady emission and a flare hypothesis (2 trials)

1720 Trials can be both independent, or correlated:

- 1721 • **Independent:** Search for a new source/signal in 1 year of data, repeat the search in
 1722 the next year of data (separately). This would be 2 independent trials, as the results
 1723 of the first year will not affect the results of the second year
- 1724 • **Correlated:** Search for a new source/signal in 1 year of data, repeat the search with
 1725 2 years of data, including the first year. This would be 2 trials, but they would be
 1726 correlated, since the results of the first 2 years of data will be affected by the results
 1727 of the first year alone.

1728 Accounting for trials is important, as given enough trials even the null hypothesis can
 1729 produce a significant result. A simple and conservative way to account for trials is to assume
 1730 that trials are uncorrelated and apply the Sidak correction (eq. 8.8):

$$P_{post} = 1 - (1 - P_{pre})^N \quad (8.8)$$

1731 Where P_{post} is the trial-corrected p-value, P_{pre} is the smallest p-value observed across
 1732 all trials performed, and N is the number of trials. This formula is intended to describe
 1733 uncorrelated trials, however it can also be used to obtain a conservative trial correction
 1734 for correlated trials as well. More sophisticated methods of accounting for correlated trials
 1735 typically involve simulation of the null hypothesis, and are oftentimes specific to a particular
 1736 experiment.

1737 When reporting a trial corrected p-value, it is additionally important to specifically state
 1738 which trials are being accounted for. Accounting for trials across all sources in a catalog
 1739 will result in a different p-value than accounting for all analyses performed by the IceCube
 1740 collaboration, yet both are "post-trial" p-values.

1741 Bibliography

- 1742 [1] Evidence for high-energy extraterrestrial neutrinos at the icecube detector. *Science*,
 1743 342(6161):1242856–1242856, Nov 2013.
- 1744 [2] Mark Aartsen, Markus Ackermann, Jenni Adams, Juan Antonio Aguilar, Markus Ahlers, Maryon
 1745 Ahrens, Imen Al Samarai, David Altmann, Karen Andeen, and et al. Multimessenger observations of a
 1746 flaring blazar coincident with high-energy neutrino icecube-170922a. *Science*, 361(6398):eaat1378, Jul
 1747 2018.
- 1748 [3] Mark Aartsen, Markus Ackermann, Jenni Adams, Juan Antonio Aguilar, Markus Ahlers, Maryon
 1749 Ahrens, Imen Al Samarai, David Altmann, Karen Andeen, and et al. Neutrino emission from the
 1750 direction of the blazar tzs 0506+056 prior to the icecube-170922a alert. *Science*, 361(6398):147–151,
 1751 Jul 2018.
- 1752 [4] M.G. Aartsen, M. Ackermann, J. Adams, J.A. Aguilar, M. Ahlers, M. Ahrens, C. Alispach, K. Andeen,
 1753 T. Anderson, I. Ansseau, and et al. Time-integrated neutrino source searches with 10 years of icecube
 1754 data. *Physical Review Letters*, 124(5), Feb 2020.
- 1755 [5] M. G. Aartsen, M. Ackermann, J. Adams, J. A. Aguilar, M. Ahlers, M. Ahrens, I. Al Samarai, D. Alt-
 1756 mann, K. Andeen, T. Anderson, and et al. Constraints on galactic neutrino emission with seven years
 1757 of icecube data. *The Astrophysical Journal*, 849(1):67, Oct 2017.
- 1758 [6] Ke Fang, Arka Banerjee, Eric Charles, and Yuuki Omori. A cross-correlation study of high-energy
 1759 neutrinos and tracers of large-scale structure. *The Astrophysical Journal*, 894(2):112, May 2020.
- 1760 [7] Qinrui Liu and Ali Kheirandish. Searching for time-dependent high-energy neutrino emission from x-ray
 1761 binaries with icecube, 2021.
- 1762 [8] Austin William Schneider. *Precision measurements of the astrophysical neutrino flux*. PhD thesis.
- 1763 [9] Alessandro De Angelis and Mario Pimenta. *Acceleration of Charged Cosmic Rays: The Fermi Mecha-
 1764 nism*, page 582–586. Undergraduate Lecture Notes in Physics (ULNP). Springer, Cham, 2nd edition.
- 1765 [10] Graciela Gelmini. High energy cosmic rays. *Journal of Physics: Conference Series*, 171, 03 2009.
- 1766 [11] Alessandro De Angelis and Mario Pimenta. *Acceleration of Charged Cosmic Rays: The Fermi Mecha-
 1767 nism*, page 586–590. Undergraduate Lecture Notes in Physics (ULNP). Springer, Cham, 2nd edition.

- 1768 [12] Pisin Chen and K. D. Hoffman. Origin and evolution of cosmic accelerators - the unique discovery
 1769 potential of an uhe neutrino telescope: Astronomy decadal survey (2010-2020) science white paper,
 1770 2009.
- 1771 [13] Joeran Stettner. Measurement of the diffuse astrophysical muon-neutrino spectrum with ten years of
 1772 icecube data, 2019.
- 1773 [14] K P Singh. An x-ray view of quasars. *Bulletin of the Astronomical Society of India*, 41:137, 06 2013.
- 1774 [15] Abraham Loeb and Eli Waxman. The cumulative background of high energy neutrinos from starburst
 1775 galaxies. *Journal of Cosmology and Astroparticle Physics*, 2006(05):003–003, May 2006.
- 1776 [16] Tova M. Yoast-Hull, J. S. Gallagher III, Ellen G. Zweibel, and John E. Everett. Active galactic nuclei,
 1777 neutrinos, and interacting cosmic rays in ngc 253 and ngc 1068. *The Astrophysical Journal*, 780(2):137,
 1778 Dec 2013.
- 1779 [17] Brian C. Lacki, Todd A. Thompson, Eliot Quataert, Abraham Loeb, and Eli Waxman. On the gev and
 1780 tev detections of the starburst galaxies m82 and ngc 253. *The Astrophysical Journal*, 734(2):107, Jun
 1781 2011.
- 1782 [18] R. M. Bionta et al. Observation of a Neutrino Burst in Coincidence with Supernova SN 1987a in the
 1783 Large Magellanic Cloud. *Phys. Rev. Lett.*, 58:1494, 1987.
- 1784 [19] M.G. Aartsen, M. Ackermann, J. Adams, J. A. Aguilar, M. Ahlers, M. Ahrens, C. Alispach, D. Altmann,
 1785 K. Andeen, T. Anderson, and et al. Neutrinos below 100 tev from the southern sky employing refined
 1786 veto techniques to icecube data. *Astroparticle Physics*, 116:102392, Mar 2020.
- 1787 [20] M. G. Aartsen, M. Ackermann, J. Adams, J. A. Aguilar, M. Ahlers, M. Ahrens, C. Alispach, K. Andeen,
 1788 T. Anderson, I. Ansseau, and et al. Icecube search for high-energy neutrino emission from tev pulsar
 1789 wind nebulae. *The Astrophysical Journal*, 898(2):117, Jul 2020.
- 1790 [21] Matteo Agostini, Michael Böhmer, Jeff Bosma, Kenneth Clark, Matthias Danninger, Christian Fruck,
 1791 Roman Gernhäuser, Andreas Gärtner, Darren Grant, Felix Henningsen, and et al. The pacific ocean
 1792 neutrino experiment. *Nature Astronomy*, 4(10):913–915, Sep 2020.
- 1793 [22] A. Kappes. Km3net: A next generation neutrino telescope in the mediterranean sea, 2007.
- 1794 [23] Kohta Murase and Eli Waxman. Constraining high-energy cosmic neutrino sources: Implications and
 1795 prospects. *Physical Review D*, 94(10), Nov 2016.
- 1796 [24] J. A. Formaggio and G. P. Zeller. From ev to eev: Neutrino cross sections across energy scales. *Reviews
 1797 of Modern Physics*, 84(3):1307–1341, Sep 2012.
- 1798 [25] M. G. Aartsen et al. Detection of a particle shower at the Glashow resonance with IceCube. *Nature*,
 1799 591(7849):220–224, 2021. [Erratum: Nature 592, E11 (2021)].
- 1800 [26] I. M. Frank and I. E. Tamm. Coherent visible radiation of fast electrons passing through matter. *Compt.
 1801 Rend. Acad. Sci. URSS*, 14(3):109–114, 1937.

- 1802 [27] Stefaan Tavernier. *Experimental techniques in nuclear and particle physics*, page 177–181. Springer,
1803 2014.
- 1804 [28] M.G. Aartsen, M. Ackermann, J. Adams, J.A. Aguilar, M. Ahlers, M. Ahrens, D. Altmann, K. Andeen,
1805 T. Anderson, I. Ansseau, and et al. The icecube neutrino observatory: instrumentation and online
1806 systems. *Journal of Instrumentation*, 12(03):P03012–P03012, Mar 2017.
- 1807 [29] R. Abbasi, Y. Abdou, T. Abu-Zayyad, M. Ackermann, J. Adams, J.A. Aguilar, M. Ahlers, M.M. Allen,
1808 D. Altmann, K. Andeen, and et al. The design and performance of icecube deepcore. *Astroparticle
1809 Physics*, 35(10):615–624, May 2012.
- 1810 [30] Francis Halzen and Dan Hooper. High-energy neutrino astronomy: the cosmic ray connection. *Reports
1811 on Progress in Physics*, 65(7):1025–1078, Jun 2002.
- 1812 [31] Eli Waxman and John Bahcall. High energy neutrinos from astrophysical sources: An upper bound.
1813 *Physical Review D*, 59(2), Dec 1998.
- 1814 [32] IceCube Collaboration and M. G. Aartsen et. al. The icecube neutrino observatory part vi: Ice prop-
1815 erties, reconstruction and future developments, 2013.
- 1816 [33] Manuel Silva and Sarah Mancina. Measurement of the diffuse muon neutrino flux using starting track
1817 events in icecube, 2019.
- 1818 [34] IceCube Collaboration and R. Abbasi et. al. Icecube data for neutrino point-source searches years
1819 2008–2018. 2021.
- 1820 [35] M. G. Aartsen, M. Ackermann, J. Adams, J. A. Aguilar, M. Ahlers, M. Ahrens, D. Altmann, K. Andeen,
1821 T. Anderson, and et al. Search for steady point-like sources in the astrophysical muon neutrino flux
1822 with 8 years of icecube data. *The European Physical Journal C*, 79(3), Mar 2019.
- 1823 [36] M. G. Aartsen, K. Abraham, M. Ackermann, J. Adams, J. A. Aguilar, M. Ahlers, M. Ahrens, D. Altmann,
1824 K. Andeen, T. Anderson, and et al. All-sky search for time-integrated neutrino emission from
1825 astrophysical sources with 7 yr of icecube data. *The Astrophysical Journal*, 835(2):151, Jan 2017.
- 1826 [37] R. Abbasi, M. Ackermann, J. Adams, J. A. Aguilar, M. Ahlers, M. Ahrens, C. Alispach, A. A. Alves Jr.
1827 au2, N. M. Amin, R. An, K. Andeen, T. Anderson, I. Ansseau, G. Anton, C. Argüelles, S. Axani,
1828 X. Bai, A. Balagopal V., A. Barbano, S. W. Barwick, B. Bastian, V. Basu, V. Baum, S. Baur, R. Bay,
1829 J. J. Beatty, K. H. Becker, J. Becker Tjus, C. Bellenghi, S. BenZvi, D. Berley, E. Bernardini, D. Z.
1830 Besson, G. Binder, D. Bindig, E. Blaufuss, S. Blot, S. Böser, O. Botner, J. Böttcher, E. Bourbeau,
1831 J. Bourbeau, F. Bradascio, J. Braun, S. Bron, J. Brosteau-Kaiser, A. Burgman, R. S. Busse, M. A.
1832 Campana, C. Chen, D. Chirkin, S. Choi, B. A. Clark, K. Clark, L. Classen, A. Coleman, G. H. Collin,
1833 J. M. Conrad, P. Coppin, P. Correa, D. F. Cowen, R. Cross, P. Dave, C. De Clercq, J. J. DeLau-
1834 nay, H. Dembinski, K. Deoskar, S. De Ridder, A. Desai, P. Desiati, K. D. de Vries, G. de Wasseige,
1835 M. de With, T. DeYoung, S. Dharami, A. Diaz, J. C. Díaz-Vélez, H. Dujmovic, M. Dunkman, M. A.
1836 DuVernois, E. Dvorak, T. Ehrhardt, P. Eller, R. Engel, J. Evans, P. A. Evenson, S. Fahey, A. R.
1837 Fazely, S. Fiedlschuster, A. T. Fienberg, K. Filimonov, C. Finley, L. Fischer, D. Fox, A. Franckowiak,
1838 E. Friedman, A. Fritz, P. Fürst, T. K. Gaisser, J. Gallagher, E. Ganster, S. Garrappa, L. Gerhardt,
1839 A. Ghadimi, C. Glaser, T. Glauch, T. Glüsenkamp, A. Goldschmidt, J. G. Gonzalez, S. Goswami,
1840 D. Grant, T. Grégoire, Z. Griffith, S. Griswold, M. Gündüz, C. Haack, A. Hallgren, R. Halliday, L. Halve,
1841 F. Halzen, M. Ha Minh, K. Hanson, J. Hardin, A. A. Harnisch, A. Haungs, S. Hauser, D. Hebecker,

- 1842 K. Helbing, F. Henningsen, E. C. Hettinger, S. Hickford, J. Hignight, C. Hill, G. C. Hill, K. D. Hoffman,
 1843 R. Hoffmann, T. Hoinka, B. Hokanson-Fasig, K. Hoshina, F. Huang, M. Huber, T. Huber, K. Hultqvist,
 1844 M. Hünnefeld, R. Hussain, S. In, N. Iovine, A. Ishihara, M. Jansson, G. S. Japaridze, M. Jeong, B. J. P.
 1845 Jones, R. Joppe, D. Kang, W. Kang, X. Kang, A. Kappes, D. Kappesser, T. Karg, M. Karl, A. Karle,
 1846 U. Katz, M. Kauer, M. Kellermann, J. L. Kelley, A. Kheirandish, J. Kim, K. Kin, T. Kintscher, J. Kiryluk,
 1847 S. R. Klein, R. Koirala, H. Kolanoski, L. Köpke, C. Kopper, S. Kopper, D. J. Koskinen, P. Koundal,
 1848 M. Kovacevich, M. Kowalski, K. Krings, G. Krückl, N. Kurashiki, A. Kyriacou, C. Lagunas Gualda,
 1849 J. L. Lanfranchi, M. J. Larson, F. Lauber, J. P. Lazar, K. Leonard, A. Leszczyńska, Y. Li, Q. R. Liu,
 1850 E. Lohfink, C. J. Lozano Mariscal, L. Lu, F. Lucarelli, A. Ludwig, W. Luszczak, Y. Lyu, W. Y. Ma,
 1851 J. Madsen, K. B. M. Mahn, Y. Makino, P. Mallik, S. Mancina, I. C. Mariş, R. Maruyama, K. Mase,
 1852 F. McNally, K. Meagher, A. Medina, M. Meier, S. Meighen-Berger, J. Merz, J. Micallef, D. Mockler,
 1853 G. Momenté, T. Montaruli, R. W. Moore, K. Morik, R. Morse, M. Moulai, R. Naab, R. Nagai,
 1854 U. Naumann, J. Necker, L. V. Nguyêñ, H. Niederhausen, M. U. Nisa, S. C. Nowicki, D. R. Nygren,
 1855 A. Obertacke Pollmann, M. Oehler, A. Olivas, E. O'Sullivan, H. Pandya, D. V. Pankova, N. Park,
 1856 G. K. Parker, E. N. Paudel, P. Peiffer, C. Pérez de los Heros, S. Philippen, D. Pieloth, S. Pieper,
 1857 A. Pizzuto, M. Plum, Y. Popovych, A. Porcelli, M. Prado Rodriguez, P. B. Price, B. Pries, G. T. Przybylski,
 1858 C. Raab, A. Raissi, M. Rameez, K. Rawlins, I. C. Rea, A. Rehman, R. Reimann, M. Renschler,
 1859 G. Renzi, E. Resconi, S. Reusch, W. Rhode, M. Richman, B. Riedel, S. Robertson, G. Roellinghoff,
 1860 M. Rongen, C. Rott, T. Ruhe, D. Ryckbosch, D. Rysewyk Cantu, I. Safa, S. E. Sanchez Herrera,
 1861 A. Sandrock, J. Sandroos, M. Santander, S. Sarkar, S. Sarkar, K. Satalecka, M. Scharf, M. Schaufel,
 1862 H. Schieler, P. Schlunder, T. Schmidt, A. Schneider, J. Schneider, F. G. Schröder, L. Schumacher,
 1863 S. Sclafani, D. Seckel, S. Seunarine, A. Sharma, S. Shefali, M. Silva, B. Skrzypek, B. Smithers, R. Snihur,
 1864 J. Soedingrekso, D. Soldin, G. M. Spiczak, C. Spiering, J. Stachurska, M. Stamatikos, T. Stanev,
 1865 R. Stein, J. Stettner, A. Steuer, T. Stezelberger, R. G. Stokstad, T. Stürwald, T. Stuttard, G. W.
 1866 Sullivan, I. Taboada, F. Tenholt, S. Ter-Antonyan, S. Tilav, F. Tischbein, K. Tollefson, L. Tomankova,
 1867 C. Tönnis, S. Toscano, D. Tosi, A. Trettin, M. Tselengidou, C. F. Tung, A. Turcati, R. Turcotte, C. F.
 1868 Turley, J. P. Twagirayezu, B. Ty, M. A. Unland Elorrieta, N. Valtonen-Mattila, J. Vandebroucke,
 1869 D. van Eijk, N. van Eijndhoven, D. Vannerom, J. van Santen, S. Verpoest, M. Vraeghe, C. Walck,
 1870 A. Wallace, T. B. Watson, C. Weaver, A. Weindl, M. J. Weiss, J. Weldert, C. Wendt, J. Werthebach,
 1871 M. Weyrauch, B. J. Whelan, N. Whitehorn, K. Wiebe, C. H. Wiebusch, D. R. Williams, M. Wolf,
 1872 K. Woschnagg, G. Wrede, J. Wulff, X. W. Xu, Y. Xu, J. P. Yanez, S. Yoshida, T. Yuan, and Z. Zhang.
 1873 A convolutional neural network based cascade reconstruction for the icecube neutrino observatory, 2021.
- 1874 [38] R. Abbasi et.al. Measurement of astrophysical tau neutrinos in icecube's high-energy starting events,
 1875 2020.
- 1876 [39] IceCube Collaboration. Icecube muon filter for 2010 pole season, 2010.
- 1877 [40] J. Ahrens, X. Bai, R. Bay, S.W. Barwick, T. Becka, J.K. Becker, K.-H. Becker, E. Bernardini,
 1878 D. Bertrand, A. Biron, and et al. Muon track reconstruction and data selection techniques in amanda.
 1879 *Nuclear Instruments and Methods in Physics Research Section A: Accelerators, Spectrometers, Detectors
 1880 and Associated Equipment*, 524(1-3):169–194, May 2004.
- 1881 [41] M.G. Aartsen, R. Abbasi, Y. Abdou, M. Ackermann, J. Adams, J.A. Aguilar, M. Ahlers, D. Altmann,
 1882 J. Auffenberg, X. Bai, and et al. Measurement of south pole ice transparency with the icecube led
 1883 calibration system. *Nuclear Instruments and Methods in Physics Research Section A: Accelerators,
 1884 Spectrometers, Detectors and Associated Equipment*, 711:73–89, May 2013.
- 1885 [42] Till Neunhöffer. Estimating the angular resolution of tracks in neutrino telescopes based on a likelihood
 1886 analysis. *Astroparticle Physics*, 25(3):220–225, Apr 2006.

- 1887 [43] M G Aartsen, R Abbasi, M Ackermann, J Adams, J A Aguilar, M Ahlers, D Altmann, C Arguelles,
 1888 J Auffenberg, X Bai, and et al. Energy reconstruction methods in the icecube neutrino telescope.
 1889 *Journal of Instrumentation*, 9(03):P03009–P03009, Mar 2014.
- 1890 [44] R. Abbasi and M. Ackermann et. al. The icecube high-energy starting event sample: Description and
 1891 flux characterization with 7.5 years of data. 2020.
- 1892 [45] Tessa Carver. *Time integrated searches for astrophysical neutrino sources using the icecube detector and
 1893 gender in physics studies for the genera project*. PhD thesis.
- 1894 [46] René Reimann. *Search for the sources of the astrophysical high-energy muon-neutrino flux with the
 1895 IceCube neutrino observatory*. PhD thesis, RWTH Aachen U., 2019.
- 1896 [47] Jim Braun, Mike Baker, Jon Dumm, Chad Finley, Albrecht Karle, and Teresa Montaruli. Time-
 1897 dependent point source search methods in high energy neutrino astronomy. *Astroparticle Physics*,
 1898 33(3):175–181, Apr 2010.
- 1899 [48] M. Ackermann, M. Ajello, W. B. Atwood, L. Baldini, J. Ballet, G. Barbiellini, D. Bastieri, J. Becerra
 1900 Gonzalez, R. Bellazzini, E. Bissaldi, and et al. The third catalog of active galactic nuclei detected by
 1901 thefermilarge area telescope. *The Astrophysical Journal*, 810(1):14, Aug 2015.
- 1902 [49] M. G. Aartsen, K. Abraham, M. Ackermann, J. Adams, J. A. Aguilar, M. Ahlers, M. Ahrens, D. Alt-
 1903 mann, K. Andeen, T. Anderson, and et al. The contribution offermi-2lac blazars to diffuse tev-pev
 1904 neutrino flux. *The Astrophysical Journal*, 835(1):45, Jan 2017.
- 1905 [50] LAT Collaboration. Fermi large area telescope third source catalog, 2015.
- 1906 [51] S. Abdollahi, M. Ackermann, M. Ajello, A. Albert, L. Baldini, J. Ballet, G. Barbiellini, D. Bastieri,
 1907 J. Becerra Gonzalez, R. Bellazzini, and et al. The second catalog of flaring gamma-ray sources from
 1908 thefermi all-sky variability analysis. *The Astrophysical Journal*, 846(1):34, Aug 2017.
- 1909 [52] Andrea Zonca, Leo P. Singer, Daniel Lenz, Martin Reinecke, Cyrille Rosset, Eric Hivon, and
 1910 Krzysztof M. Gorski. healpy: equal area pixelization and spherical harmonics transforms for data
 1911 on the sphere in python. *Journal of Open Source Software*, 4(35):1298, 2019.
- 1912 [53] <https://github.com/ChrisCFTung/FIRESONG>. Icecube muon filter for 2010 pole season, 2021.
- 1913 [54] Andrew M. Hopkins and John F. Beacom. On the normalization of the cosmic star formation history.
 1914 *The Astrophysical Journal*, 651(1):142–154, Nov 2006.
- 1915 [55] ANTARES Collaboration. Antares: the first undersea neutrino telescope, 2011.
- 1916 [56] A. Albert, M. André, M. Anghinolfi, G. Anton, M. Ardid, J.-J. Aubert, J. Aublin, T. Avgitas, B. Baret,
 1917 J. Barrios-Martí, and et al. All-flavor search for a diffuse flux of cosmic neutrinos with nine years of
 1918 antares data. *The Astrophysical Journal*, 853(1):L7, Jan 2018.
- 1919 [57] Giulia Illuminati and Alexander Plavin. ANTARES search for neutrino flares from the direction of
 1920 radio-bright blazars. *PoS*, ICRC2021:972, 2021.

- 1921 [58] J.A. Aguilar, P. Allison, J.J. Beatty, H. Bernhoff, D. Besson, N. Bingefors, O. Botner, S. Buitink,
 1922 K. Carter, B.A. Clark, and et al. Design and sensitivity of the radio neutrino observatory in greenland
 1923 (rno-g). *Journal of Instrumentation*, 16(03):P03025, Mar 2021.
- 1924 [59] Stephanie Wissel, Andrés Romero-Wolf, Harm Schoorlemmer, Washington R. Carvalho Jr., Jaime
 1925 Alvarez-Muñiz, Enrique Zas, Austin Cummings, Cosmin Deaconu, Kaeli Hughes, Andrew Ludwig,
 1926 and et al. Prospects for high-elevation radio detection of 0.10 pev tau neutrinos. *Journal of Cosmology*
 1927 and *Astroparticle Physics*, 2020(11):065–065, Nov 2020.
- 1928 [60] M. G. Aartsen, M. Ackermann, J. Adams, J. A. Aguilar, M. Ahlers, M. Ahrens, C. Alispach, K. Andeen,
 1929 T. Anderson, I. Ansseau, G. Anton, C. Argüelles, T. C. Arlen, J. Auffenberg, S. Axani, P. Backes,
 1930 H. Bagherpour, X. Bai, A. Balagopal V., A. Barbano, I. Bartos, B. Bastian, V. Baum, S. Baur,
 1931 R. Bay, J. J. Beatty, K. H. Becker, J. Becker Tjus, S. BenZvi, D. Berley, E. Bernardini, D. Z. Besson,
 1932 G. Binder, D. Bindig, E. Blaufuss, S. Blot, C. Bohm, M. Bohmer, M. Börner, S. Böser, O. Botner,
 1933 J. Böttcher, E. Bourbeau, J. Bourbeau, F. Bradascio, J. Braun, S. Bron, J. Brosteau-Kaiser,
 1934 A. Burgman, J. Buscher, R. S. Busse, M. Bustamante, T. Carver, C. Chen, P. Chen, E. Cheung,
 1935 D. Chirkin, B. Clark, K. Clark, L. Classen, A. Coleman, G. H. Collin, A. Connolly, J. M. Conrad,
 1936 P. Coppin, P. Correa, D. F. Cowen, R. Cross, P. Dave, C. Deaconu, J. P. A. M. de André, C. De Clercq,
 1937 S. DeKockere, J. J. DeLaunay, H. Dembinski, K. Deoskar, S. De Ridder, P. Desiati, K. D. de Vries,
 1938 G. de Wasseige, M. de With, T. DeYoung, A. Diaz, J. C. Díaz-Vélez, H. Dujmovic, M. Dunkman, M. A.
 1939 DuVernois, E. Dvorak, B. Eberhardt, T. Ehrhardt, P. Eller, R. Engel, J. J. Evans, P. A. Evenson, S. Fahey,
 1940 K. Farrag, A. R. Fazely, J. Felde, K. Filimonov, C. Finley, A. Franckowiak, E. Friedman, A. Fritz,
 1941 T. K. Gaisser, J. Gallagher, E. Ganster, D. Garcia-Fernandez, S. Garrappa, A. Gartner, L. Gerhardt,
 1942 R. Gernhaeuser, K. Ghorbani, T. Glauch, T. Glüsenkamp, A. Goldschmidt, J. G. Gonzalez, D. Grant,
 1943 Z. Griffith, M. Günder, M. Gündüz, C. Haack, A. Hallgren, L. Halve, F. Halzen, K. Hanson, J. Haugen,
 1944 A. Haungs, D. Hebecker, D. Heereman, P. Heix, K. Helbing, R. Hellauer, F. Henningsen, S. Hickford,
 1945 J. Hignight, G. C. Hill, K. D. Hoffman, B. Hoffmann, R. Hoffmann, T. Hoinka, B. Hokanson-Fasig,
 1946 K. Holzapfel, K. Hoshina, F. Huang, M. Huber, T. Huber, T. Huege, K. Hughes, K. Hultqvist,
 1947 M. Hünenfeld, R. Hussain, S. In, N. Iovine, A. Ishihara, G. S. Japaridze, M. Jeong, K. Jero, B. J. P.
 1948 Jones, F. Jonske, R. Joppe, O. Kalekin, D. Kang, W. Kang, A. Kappes, D. Kappesser, T. Karg, M. Karl,
 1949 A. Karle, T. Katori, U. Katz, M. Kauer, A. Keivani, J. L. Kelley, A. Kheirandish, J. Kim, T. Kintscher,
 1950 J. Kiryluk, T. Kittler, S. R. Klein, R. Koirala, H. Kolanoski, L. Köpke, C. Kopper, S. Kopper, D. J.
 1951 Koskinen, M. Kowalski, C. B. Krauss, K. Krings, G. Krückl, N. Kulacz, N. Kurahashi, A. Kyriacou,
 1952 M. Labare, J. L. Lanfranchi, M. J. Larson, U. Latif, F. Lauber, J. P. Lazar, K. Leonard, A. Leszczynska,
 1953 M. Leuermann, Q. R. Liu, E. Lohfink, J. LoSecco, C. J. Lozano Mariscal, L. Lu, F. Lucarelli,
 1954 J. Lünemann, W. Luszczak, Y. Lyu, W. Y. Ma, J. Madsen, G. Maggi, K. B. M. Mahn, Y. Makino,
 1955 P. Mallik, K. Mallot, S. Mancina, S. Mandalia, I. C. Maris, S. Marka, Z. Marka, R. Maruyama, K. Mase,
 1956 R. Maunu, F. McNally, K. Meagher, M. Medici, A. Medina, M. Meier, S. Meighen-Berger, T. Menne,
 1957 G. Merino, T. Meures, J. Micallef, G. Momenté, T. Montaruli, R. W. Moore, R. Morse, M. Moulai,
 1958 P. Muth, R. Nagai, J. Nam, U. Naumann, G. Neer, A. Nelles, H. Niederhausen, S. C. Nowicki, D. R.
 1959 Nygren, A. Obertacke Pollmann, M. Oehler, A. Olivas, A. O'Murchadha, E. O'Sullivan, T. Palczewski,
 1960 H. Pandya, D. V. Pankova, L. Papp, N. Park, P. Peiffer, C. Pérez de los Heros, T. C. Petersen, S. Philippen,
 1961 D. Pieloth, E. Pinat, J. L. Pinfold, A. Pizzuto, I. Plaisier, M. Plum, A. Porcelli, P. B. Price, G. T.
 1962 Przybylski, C. Raab, A. Raissi, M. Rameez, L. Rauch, K. Rawlins, I. C. Rea, R. Reimann, B. Relethford,
 1963 M. Renschler, G. Renzi, E. Resconi, W. Rhode, M. Richman, M. Riegel, S. Robertson, M. Rongen,
 1964 C. Rott, T. Ruhe, D. Ryckbosch, D. Rysewyk, I. Safa, S. E. Sanchez Herrera, A. Sandrock, J. Sandroos,
 1965 P. Sandstrom, M. Santander, S. Sarkar, S. Sarkar, K. Satalecka, M. Schaufel, H. Schieler, P. Schlundt,
 1966 T. Schmidt, A. Schneider, J. Schneider, F. G. Schröder, L. Schumacher, S. Sclafani, D. Seckel,
 1967 S. Seunarine, M. H. Shaevitz, S. Shefali, M. Silva, D. Smith, R. Snihur, J. Soedingrekso, D. Soldin,
 1968 S. Söldner-Rembold, M. Song, D. Southall, G. M. Spiczak, C. Spiering, J. Stachurska, M. Stamatikos,
 1969 T. Stanov, R. Stein, P. Steinmüller, J. Stettner, A. Steuer, T. Stezelberger, R. G. Stokstad, A. Stößl,
 1970 N. L. Strotjohann, T. Stürwald, T. Stuttard, G. W. Sullivan, I. Taboada, A. Taketa, H. K. M. Tanaka,
 1971 F. Tenholt, S. Ter-Antonyan, A. Terliuk, S. Tilav, L. Tomankova, C. Tönnis, J. Torres, S. Toscano,
 1972 D. Tosi, A. Trettin, M. Tselengidou, C. F. Tung, A. Turcati, R. Turcotte, C. F. Turley, B. Ty, E. Unger,

- 1973 M. A. Unland Elorrieta, M. Usner, J. Vandebroucke, W. Van Driessche, D. van Eijk, N. van Eijndhoven,
 1974 S. Vanheule, A. Vieregg, J. van Santen, D. Veberic, M. Vraeghe, C. Walck, A. Wallace, M. Wallraff,
 1975 N. Wandkowsky, T. B. Watson, C. Weaver, A. Weindl, M. J. Weiss, J. Weldert, C. Welling, C. Wendt,
 1976 J. Werthebach, B. J. Whelan, N. Whitehorn, K. Wiebe, C. H. Wiebusch, L. Wille, D. R. Williams,
 1977 L. Wills, S. Wissel, M. Wolf, J. Wood, T. R. Wood, K. Woschnagg, G. Wrede, S. Wren, D. L. Xu,
 1978 X. W. Xu, Y. Xu, J. P. Yanez, G. Yodh, S. Yoshida, T. Yuan, and M. Zöcklein. Neutrino astronomy
 1979 with the next generation icecube neutrino observatory, 2019.
- 1980 [61] Q. Abarr, P. Allison, J. Ammerman Yebra, J. Alvarez-Muñiz, J. J. Beatty, D. Z. Besson, P. Chen,
 1981 Y. Chen, X. Cheng, J. M. Clem, A. Connolly, L. Cremonesi, C. Deaconu, J. Flaherty, D. Friksen, P. W.
 1982 Gorham, C. Hast, C. Hornhuber, J. J. Huang, K. Hughes, A. Hynous, Y. Ku, C. Y. Kuo, T. C. Liu,
 1983 Z. Martin, C. Miki, J. Nam, R. J. Nichol, K. Nishimura, A. Novikov, A. Nozdrina, E. Oberla, S. Prohira,
 1984 R. Prechelt, B. F. Rauch, J. M. Roberts, A. Romero-Wolf, J. W. Russell, D. Seckel, J. Shiao, D. Smith,
 1985 D. Southall, G. S. Varner, A. G. Vieregg, S. H. Wang, Y. H. Wang, S. A. Wissel, R. Young, E. Zas,
 1986 and A. Zeolla. The payload for ultrahigh energy observations (pueo): A white paper, 2021.
- 1987 [62] A. V. Olinto, J. Krizmanic, J. H. Adams, R. Aloisio, L. A. Anchordoqui, A. Anzalone, M. Bagheri,
 1988 D. Barghini, M. Battisti, D. R. Bergman, M. E. Bertaina, P. F. Bertone, F. Bisconti, M. Bustamante,
 1989 F. Cafagna, R. Caruso, M. Casolino, K. Černý, M. J. Christl, A. L. Cummings, I. De Mitri,
 1990 R. Diesing, R. Engel, J. Eser, K. Fang, F. Fenu, G. Filippatos, E. Gazda, C. Guepin, A. Haungs,
 1991 E. A. Hays, E. G. Judd, P. Klimov, V. Kungel, E. Kuznetsov, Š. Mackovjak, D. Mandát, L. Marcelli,
 1992 J. McEnergy, G. Medina-Tanco, K. D. Merenda, S. S. Meyer, J. W. Mitchell, H. Miyamoto, J. M. Nacht-
 1993 man, A. Neronov, F. Oikonomou, Y. Onel, G. Osteria, A. N. Otte, E. Parizot, T. Paul, M. Pech, J. S.
 1994 Perkins, P. Picozza, L. W. Piotrowski, Z. Plebaniak, G. Prévôt, P. Reardon, M. H. Reno, M. Ricci,
 1995 O. Romero Matamala, F. Sarazin, P. Schovánek, V. Scotti, K. Shinozaki, J. F. Soriano, F. Stecker,
 1996 Y. Takizawa, R. Ulrich, M. Unger, T. M. Venters, L. Wiencke, D. Winn, R. M. Young, and M. Zotov.
 1997 The poemma (probe of extreme multi-messenger astrophysics) observatory, 2021.
- 1998 [63] R J Barlow. *Statistics: A Guide to the Use of Statistical Methods in the Physical Sciences*. Wiley and
 1999 Sons, 1989.